International Science and Technology (ISAT) Linkages Fund

The Chemistry and Physics of Heavy and Superheavy Elements

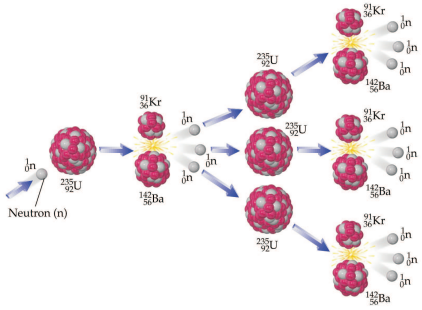

Proceedings of the First German / New Zealand Workshop on Heavy and Superheavy Elements

Financed by

THE NEW ZEALAND MINISTRY OF RESEARCH, SCIENCE AND TECHNOLOGY/DEUTSCHE FORSCHUNGSGEMEINSCHAFT (DFG) PROGRAMME

and

MASSEY UNIVERSITY

Edited by

Matthias Lein and Peter Schwerdtfeger

Theoretical and Computational Chemistry Research Centre, Institute of Fundamental Sciences, Massey University (Albany) Auckland, New Zealand

Support of Science and Technology Cooperation with Germany

I am pleased to announce the support of this workshop through New Zealand funds established through a Memorandum of Understanding (MoU) between the Ministry of Research, Science and Technology (MoRST) and the German Research Foundation (Deutsche Forschungsgemeinschaft (DFG) signed in 1997. These DFG funds are competitive and administrated by the Royal Society in New Zealand.

The MoU essentially says that MoRST and DFG recognise the mutual benefit of scientific interchange between New Zealand and Germany and that both parties facilitate cooperation between specialists in scientific disciplines within their mutual competence through research visits, exploratory missions, joint seminars and workshops subject to the laws and regulations in force in the two countries and subject to the financial limitations of each side.

Both New Zealand and Germany have a number of mechanisms to support the Science and Technology Cooperation (STC) Agreement which was signed and established in 1977. The International Science and Technology (ISAT) Linkage fund in New Zealand supports travel overseas for

- research collaborations and international conferences/meetings,
- conference and workshop sponsorship and
- international fellowships

The schemes that are funded through ISAT include:

- The STC funds which are also part of ISAT are reciprocated by the Ministerium für Bildung und Forschung in Germany, BMBF (Ministry of Education and Research) through its International Bureau.
- The DFG funds sponsoring visits and workshops such as this workshop The Julius von Haast Fellowship (JvH), a prestigious reciprocal scheme to the
- Alexander von Humboldt Foundation (AvH) award programme inviting a top German researcher to work in NZ for 4 weeks per year over a 3 year period. The JvH fellowship award is supported by a MoU with the AvH.

Additional funding for international collaboration include the International Investment Opportunity Fund (IIOF) and the technical participation Programme (TPP). Other opportunities are within our mainstream funding from the Health Research Council (HRC) and the Foundation for Research Science and Technology (FRST).

Further information on funding opportunities on the web-sites of MoRST www.morst.govt.nz, the Foundation www.frst.govt.nz, the Health Research Council www.hrc.govt.nz and the Royal Society New Zealand www.rsnz.org and its Collaboration web-site: http://colab.rsnz.org/germany/ .

Congratulation to the workshop organisers, Prof Peter Schwerdtfeger and Prof Burkhard Fricke for their successful application and best wishes for a productive workshop which I could imagine being the start of a series maybe continued in Germany.

Dr Werner Friedrich
Ministry for Research Science and Technology
May 2005

Preface

In September 1997 a Memorandum of Understanding was signed between the New Zealand Ministry of Research, Science and Technology and the Deutsche Forschungsgemeinschaft (DFG) of Germany. The broad purpose of the MOU is to foster exchange of researchers between New Zealand and Germany. To support the MOU, the Minister of Research, Science and Technology, through the International Science and Technology (ISAT) Linkages Fund has allocated funding to the "NZ/DFG Programme" for 2004-05. Funding is provided for joint seminars and workshops in areas where the exchange of information promises to improve the level of co-operation between scientists of the two countries. The joint seminars and workshops can be held in either country. Joint applications are encouraged with New Zealand applications to the Royal Society of NZ and German applications to the German Research Foundation (DFG Deutsche Forschungsgemeinschaft).

On a rather short notice for the first funding round we decided to organize a workshop on heavy and superheavy element chemistry and physics to be held at Massey University (in Auckland) bringing together renowned scientists in this field from both physics and chemistry, theoreticians and experimentalists, from both Germany and New Zealand. This area has gone through a scientific renaissance both on the computational and experimental side in the last two decades underlining the importance of fundamental research for the advancement of knowledge. We hope that the workshop will be a success and can be repeated in not too distant future in Germany.

It is our hope that this workshop will help to strengthen the already existing national and international collaborations and may encourage the formation of new co-operations among the attending scientists.

We are grateful to the Ministry of Research, Science and Technology (New Zealand) and the Deutsche Forschungsgemeinschaft (Germany) through the ISAT Linkage Fund, and to Massey University for financial support. We thank Vesna Davidovic-Alexander for her help and assistance in organising this meeting.

The Organisers:
Prof. Peter Schwerdtfeger (Auckland)
Prof. Burkhard Fricke (Kassel)
Dr. Matthias Lein (Auckland)
May 2005

28 May 2005

Time	**Speaker**	**Title**
8.45 – 9.00	Dr. Werner Friedrich	Welcome
	Chair: Peter Schwerdtfeger	
9.00 – 9.40	Burkhard Fricke (Kassel)	Early History of Superheavy Elements and their Chemical Predictions
9.40 – 10.20	Valeria Pershina (Darmstadt)	The Chemistry of Superheavy Elements and Relativistic Effects
10.20 – 10.50	Coffee	
	Chair: Hermann Stoll	
10.50 – 11.15	Robert Krawczyk (Massey, Auckland)	Coinage Metal Halide Oligomers
11.15 – 11.40	Matthias Lein (Massey, Auckland)	Catalytic Activity of Au(III)
11.40 – 12.05	Behnam Assadollahzadeh (Massey, Auckland)	DFT Study of Structural and Physical Properties of Gold and Cesium Clusters
12.05 – 14.00	Lunch	
	Chair: Burkhard Fricke	
14.00 – 14.40	Christoph van Wüllen (Berlin)	Relativistic quantum chemistry with two-component spinors
14.40 – 15.20	Hermann Stoll (Stuttgart)	Relativistic Pseudopotentials
15.20 – 16.00	Josef Anton (Kassel)	Non-collinear and collinear relativistic density functional theory
16.00 – 16.30	Coffee	
	Chair: Christoph Van Wüllen	
16.30 – 17.10	Cristina Sarpe-Tudoran (Kassel)	Adsorption of super-heavy elements on metal surface
17.10 – 17.50	Timo Jacob (Berlin)	Reactions on Pt and Pt-based surfaces
17.50 – 18.15	Nicola Gaston (Massey, Auckland)	The frequency-dependent dipole polarisability of the mercury dimer

29 May 2005

Time	**Speaker**	**Title**
	Chair: Valeria Pershina	
9.00 – 9.40	Matthias Schädel (GSI Darmstadt)	Chemical separation and characterization of superheavy elements.
9.40 – 10.20	Heinz Gäggeler (PSI Bern)	From few atoms/min (Rf) to few atoms/week(Z=112).
10.20 – 10.40	Coffee	
	Chair: James Wright	
10.40 – 11.20	Warren Roper (Auckland)	Compounds of Ru or Os with bonds to B, Si and Sn.
11.20 – 11.45	Pennelope Brothers (Auckland)	Theoretical investigations into transition meta-Group 13 element bonding
11.45 – 12.10	Tilo Söhnel (Auckland)	Fe, Ru and Ir containing Tin Cluster Compounds.
12.10 – 14.00	Lunch	
	Chair: Heinz Gäggeler	
14.00 – 14.40	Robert Eichler (Bern)	Thermodynamic data evaluation for gas phase chemical experiments with transactinides.
14.40 – 15.05	Hicham Idriss (Auckland)	Carbon monoxide reaction with UO_2 (111) single crystal and thin film surfaces.
15.05 – 15.30	Graham A. Bowmaker (Auckland)	Solid-state NMR of silver and mercury compounds.
15.30 – 16.00	Coffee	
	Chair: G. Bowmaker	
16.00 – 16.25	James Wright (Auckland)	Tethered Osmabenzenes Derived from an Osmabenzofuran
16.25 – 16.50	Alistair Nielson (Massey, Auckland)	A case for linear agostic interaction in tantalum chemistry
16.50 – 17.15	Peter Schwerdtfeger (Massey, Auckland)	How good is density functional theory for field gradients?
17.15 – 18.00	Final Discussions and Reflections	

Contents

First day: 25 June 2005

Time	Speaker	Title
8.45 – 9.00	Dr. Werner Friedrich	Welcome
	Chair: Peter Schwerdtfeger	
9.00 – 9.40	Burkhard Fricke	Early History of Superheavy Elements and their Chemical Predictions
9.40 – 10.20	Valeria Pershina	The Chemistry of Superheavy Elements and Relativistic Effects
10.20 – 10.50	Coffee	
	Chair: Hermann Stoll	
10.50 – 11.15	Robert Krawczyk	Coinage Metal Halide Oligomers
11.15 – 11.40	Matthias Lein	Catalytic Activity of Au(III)
11.40 – 12.05	Behnam Assadollahzadeh	DFT Study of Structural and Physical Properties of Gold and Cesium Clusters
12.05 – 14.00	Lunch	
	Chair: Burkhard Fricke	
14.00 – 14.40	Christoph van Wüllen	Relativistic quantum chemistry with two-component spinors
14.40 – 15.20	Hermann Stoll	Relativistic Pseudopotentials
15.20 – 16.00	Josef Anton	Non-collinear and collinear relativistic density functional theory
16.00 – 16.30	Coffee	
	Chair: Christoph Van Wüllen	
16.30 – 17.10	Cristina Sarpe-Tudoran	Adsorption of super-heavy elements on metal surface
17.10 – 17.50	Timo Jacob	Reactions on Pt and Pt-based surfaces
17.50 – 18.15	Nicola Gaston	The frequency-dependent dipole polarisability of the mercury dimer

Early History of Superheavy Elements and their Chemical Predictions

Burkhard Fricke

Universität Kassel, Fachbereich Naturwissenschaften, Institut für Physik,
D-34109 Kassel, Germany

1 Introduction

After the actinides hypothesis of Seaborg of the late 30s it became clear that the elements beyond Actinium had a similar behavior as the lantinides although there are significant differences. These actinide elements were successively generated in the 40s and 50s and indeed showed up as 5f elements. The half-life of the most stable isotopes decreased such that it became more and more difficult to generate them or even to generate sufficiently large quantities in order to perform chemical experiments. The details of the production and chemical behavior of these superheavy elements from the experimental side will be given in the talks by Matthias Schädel and Heinz Gäggeler.

The subject of superheavy elements more and more became a matter of nuclear physicists who tried to generate as heavy elements as possible. The most successful group for the generation of transactinides was the GSI group of Armbruster, Hofmann and others, who generated the elements 107 up to 112 between 1984 and 1996. During the last ten years one was able to

produce nuclei with charge numbers up to 118 which dominantly was done by the Dubna group [1].

From the theoretical side nuclear theory predicted a stabilization in the vicinity of magic and double-magic numbers. There were and still are numerous predictions for the stability of these elements and the so-called islands of stability which are connected with these predictions [1]. In Figure 1 we present a general idea of the islands of stability which was used in the late 70s [2].

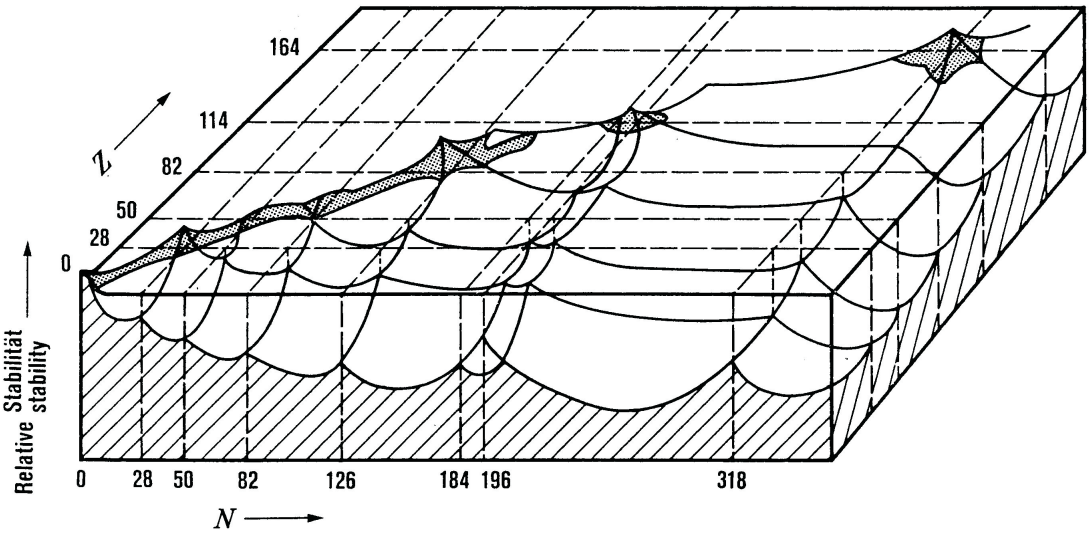

Fig. 1: Schematic diagram of the stability of the elements. This graph which shows two islands of stability near 114 and 164 was used in the 70s. This graph also shows an island of stability near element 164 which of course nowadays is out of any discussion. This prediction stirred up a number of activities in order to generate these nuclei and, as far as possible, to identify the chemical behavior.

In the early 70s first predictions of the electronic structure of these elements showed up because calculations on the level of full-relativistic calculations became available. These calculations resulted in predictions of the gross structure of the chemical behavior of these elements. Figure 2 presents

the new extended form of the periodic system of elements until element 172. Two reviews [3, 4] appeared 1971 and 1975 where this was summarized.

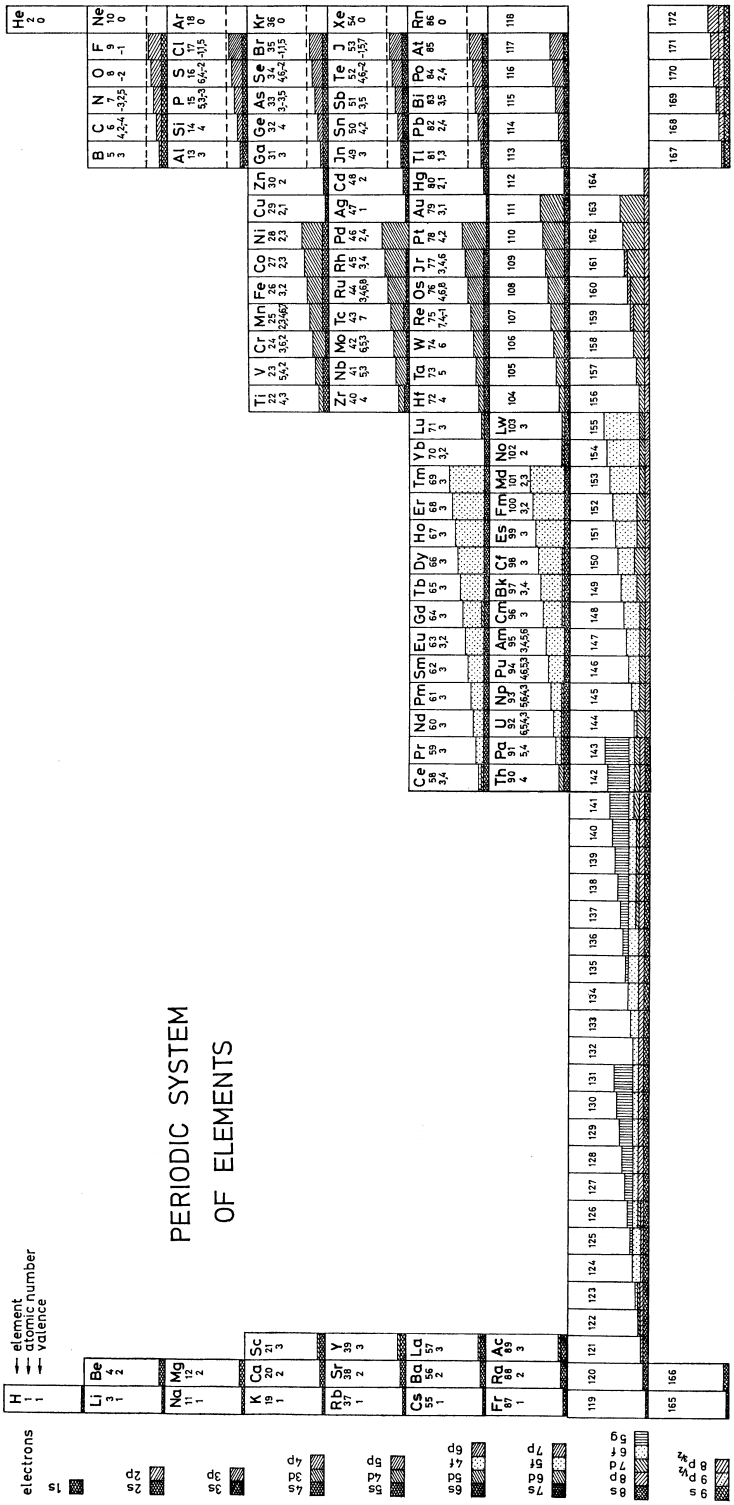

Fig. 2: Periodic system of the elements with the extension up to element 172 (taken from Ref. [3] from 1971

2 Calculation of the atomic structure of superheavy atoms

It is obvious that a calculation of the atomic structure of very heavy elements should be done by full four-component relativistic calculations which solve the Dirac equation for the many-particle systems. The talks by Christoph van Wuellen, Hermann Stoll and Josef Anton in this workshop discuss various alternatives and approximation.

The most interesting question in this connection is the difference between a non-relativistic and a relativistic approximation. Dominant is the direct relativistic effect which mainly results from the fact that a moving electron changes its effective mass due to special relativity. This increase of effective mass results in a stronger binding of all the levels which have dominant contributions in the vicinity of the nucleus where its kinetic energy sees a deep potential.

Due to the fact that these inner s and p electrons have a smaller average distance to the nucleus they shield those wave functions which have a large angular momentum. This results in the indirect relativistic effect which can be seen on the d- and especially the f-wave functions (This, by the way, is the main reason for the different behavior of the 5f elements compared to the 4f elements).

The third relativistic effect is the spin-orbit splitting which increases dramatically with the nuclear charge number. This results in wave functions which are quite different for the two components with an angular momentum plus the spin and minus the spin. Most dramatic is this spin-orbit-splitting for the p1/2 and p3/2 functions.

In the early 70s first numerical calculations became available where all

electrons in such a system were taken into account and were brought to self-consistency. The Hamiltonian which was used in these calculations was just the kinetic energy of the electrons, the elecron-nucleus interaction and the electron-electron interaction in the Slater approximation. A full Dirac-Fock calculation was not possible at that time, but the results which came out were reasonably good in order to get a first prediction on the ground states and the first excited states of the superheavy elements. The elements 104 to 120 are the ones which are of special interest nowadays and where an improvement of our knowledge in terms of nuclear stability and chemical behavior still is a point of scientific interest. From the Dirac-Fock-Slater calculations one already got an impression on the valence electron structure, the most frequent oxidation states and the ionization potentials which also served as a starting point for the interpretation. Table 1 lists the results from 1971 in the Dirac-Fock-Slater approximation. Because at that time one had hope that quantitative amounts of these elements might be available also metallic radii and densities were predicted. The gross structure of the interpretation of the chemical behavior was possible because these calculations were also performed in the homologues of the superheavy elements which of course are chemically known. This then resulted in the interpretation of the chemistry.

To summarize the development in the accuracy of atomic calculations of superheavy elements one can say that there were four stages: From 1967 to 1972 atomic relativistic many-particle calculations with the Dirac-Fock-Slater Method were performed for all elements up to 172. Since 1970 atomic Dirac-Fock calculations became available which were used for elements 103 to 108 and element 111. From 1972 on atomic Multiconfiguration Dirac-Fock calculations became available. Since 1990 large scale Multiconfiguration Dirac-Fock calculations became possible, where hundreds and thousands

Element	104	105	106	107	108	109	110	111	112
Atomic weight	278	281	283	286	289	292	295	298	301
Chemical groups	IV B	V B	VI B	VII B	VIII	VIII	VIII	I B	II B
Valence electron structure	$7s^26d^2$	$7s^26d^3$	$7s^26d^4$	$7s^26d^5$	$7s^26d^6$	$7s^26d^7$	$7s^26d^8$	$7s^26d^9$	$7s^26d^{10}$
Most frequent oxidation states	+4	+5	+6,4	+7,6,5	+8,6,4	+6,4	+4,6	+3,5	+2,4
Ionization potential (eV)	5.1	6.2	7.1	6.5	7.4	8.2	9.4	10.3	11.1

Element	113	114	115	116	117	118	119	120
Atomic weight	304	307	310	313	316	319	322	325
Chemical groups	III A	IV A	V A	VI A	VII A	0	I A	II A
Valence electron structure	$7s^27p^1$	$7s^27p^2$	$7s^27p^3$	$7s^27p^4$	$7s^27p^5$	$7s^27p^6$	$8s^1$	$8s^2$
Most frequent oxidation states	+1	+2	+3,1	+2,4	+1,3,-1	0,4	+1	+2
Ionization potential (eV)	7.5	8.5	5.9	6.8	8.2	9.0	4.1	5.3

Tab. 1: Part of the predictions for the elements 104 to 120, taken from Ref. [3]

of configurations were used in order to get better and better results. The best atomic calculations are nowadays possible with the so-called Many-Pody Pertur?bation Theory (Coupled Cluster Approach).

But already with the simple Dirac-Fock-Slater calculations one was able to get the structure of the inner shells including the wave functions [5], the influence of the extended nucleus including the number of electrons inside the nucleus, additional contributions to the inner shell binding energies and the outer shell structure in terms of wave functions and radial distributions.

3 Relativistic molecular calculations

Because the prediction of the chemistry in detail is connected to molecules one is able to perform full relativistic molecular calculations nowadays in order to find out the binding structure of those molecules who are involved in the chemistry.

This lead to more accurate predictions of ionization potentials and struc-

ture of the ions which are necessary because chemistry usually is connected not to the ground state of the neutral atoms, but to the ionized systems. With these calculations also overlap populations and Mulliken population numbers became possible. In the following talk by Valeria Pershina the details of the chemical interpretation and relativistic effects will be presented. Two reviews for the prediction of the chemistry of superheavy elements from a most modern point of view can be found in Ref. [6] and [7].

Applications of such molecular calculations in order to get predictions of the adsorption of superheavy elements on metal surfaces are presented by Cristina Sarpe-Tudoran.

References

[1] S. Hofmann; Physik-Journal **4**, No. 5, p 37 (2005)

[2] G. T. Seaborg; Welch Foundation Conference XIII The Transuranium Elements, Ed. W. O. Milligan, p. 5 (1969)

[3] B. Fricke, W. Greiner, J. T. Waber; Theoret. Cim. Acta (Berlin) **21**, 235 (1971)

[4] B. Fricke; Structure and Bonding **21**, 89 (1975)

[5] B. Fricke, G. Soff; Atom. Data Nucl. Data Tab. **19**, 83 (1977)

[6] V. Pershina; Chem. Rev. **96**, 1977 (1996)

[7] V. Pershina, B. Fricke; in: Heavy Elements and Related New Phenomena, Ed. W. Greiner, R. K. Gupta, World Scientific, Singapore, p. 194 (1999)

The Chemistry of the Superheavy Elements and Relativistic Effects

Valeria Pershina

Gesellschaft für Schwerionenforschung (GSI), Planckstr. 1, D-64291, Darmstadt

Investigations of chemical properties of the heaviest elements belong to the most fundamental and important areas of chemical science. They seek to probe the uppermost reaches of the Periodic Table of the elements where the nuclei become extremely unstable and relativistic effects on electronic shells are very strong. This makes both theoretical and experimental research in this area extremely exciting and challenging. The aim of the chemical research is to identify superheavy elements chemically in order to confirm their placement in the Periodic Table [1]. Another important goal is to establish whether the periodicities in properties observed within the groups or the rows of the Periodic Table are continued with the heaviest elements, or whether deviations can be observed due to strong relativistic effects. Especially in this part of the Periodic Table the theory is extremely important, since most of properties of the heaviest elements cannot be directly measured due to their short half-lives.

It is now well established that the use of the relativistic quantum theory and based on it relativistic atomic and molecular programs is mandatory in order to reliably predict properties and trends of the heaviest elements.

Some simple extrapolations based on periodic trends, often used in the past, should be made very cautiously.

Accurate predictions of properties of the relativistic systems became nowadays possible due to the spectacular developments in the relativistic quantum theory, computer codes and the hardware [2, 3]. Most advanced fully relativistic methods, like ab initio Dirac-Fock, or relativistic effective core potentials at the CCSD(T) level of correlation, or the relativistic gradient corrected DFT theory are needed to accurately describe bonding and spectroscopic properties of the heaviest elements.

One can distinguish between two main streams in the theoretical research on the superheavies. One is the performance of very accurate relativistic calculations for atoms [4] and small molecules with the use of the most accurate ab initio DF methods with electron correlation. To this group the calculations for small molecules using the relativistic DFT [5] and RECP CCSD(T) methods [6] could also be referred. The other part of the theoretical research [7, 8, 9] serves experimental needs. It comprises predictions of the stability of the synthesized heavy-element compounds, their adsorption behaviour in gas-phase chromatography studies, the complex formation in aqueous solutions and their extraction behaviour in liquid chromatography. This second direction is where our main efforts are concentrated. Carried out in a close link with the experiment, these theoretical works have essentially contributed to understanding the nature of bonding of the heaviest elements and the role of relativistic effects, which are of a paramount importance for these elements [7, 8, 9].

Most of our relativistic calculations [7, 8, 9] were performed with the use of the fully relativistic, 4-component, RGGA DFT method [10]. In its various approximations, it allows for treating large complex molecules in liquid phase,

or adsorption processes on various types of surfaces [11].

1 Relativistic effects

The influence of relativistic effects on valence orbital shells of relatively heavy elements, like Au or Hg, was shown in the pioneer works of Pitzer [12] and Pyykkö [13]. Later, the influence of these effects on atomic orbital shells and related properties was shown by many atomic DF and DS calculations, which are summarized in the review of Fricke [14]. The basic architecture of the Periodic Table up to Z=176 was drawn up using those results. Later, advanced atomic DF CCSD(T) calculations [4] have given a more accurate values of the energy levels of the heaviest elements up to Z=122, but did not essentially alter the basic predictions [14]. Importance of the relativistic effects for heavy-element atoms, like 112, can be seen from Fig. 1, where a large stabilization of the 7s orbital and a spin-orbit splitting of the 6d orbitals are observed.

The effect of the ns orbital contraction and stabilization reaches its maximum in the 6^{th} row on Au (17.3%) and in the 7^{th} row on element 112 (31%), the phenomenon being called the gold [13] and group-12 [15] maximum of relativistic effects, respectively. The shift of the maximum to element 112 in the 7^{th} row in contrast to gold in the 6^{th} row is due to the fact that in both the 111 and 112 elements the ground state electronic configuration is d^9s^2, while the electronic configuration changes from Au (d^9s^1) to Hg ($d^{10}s^2$).

2 Molecular properties

A real wave based on molecular relativistic calculations started at around 1990 [7]. By that time, the experimental research have accumulated a lot of

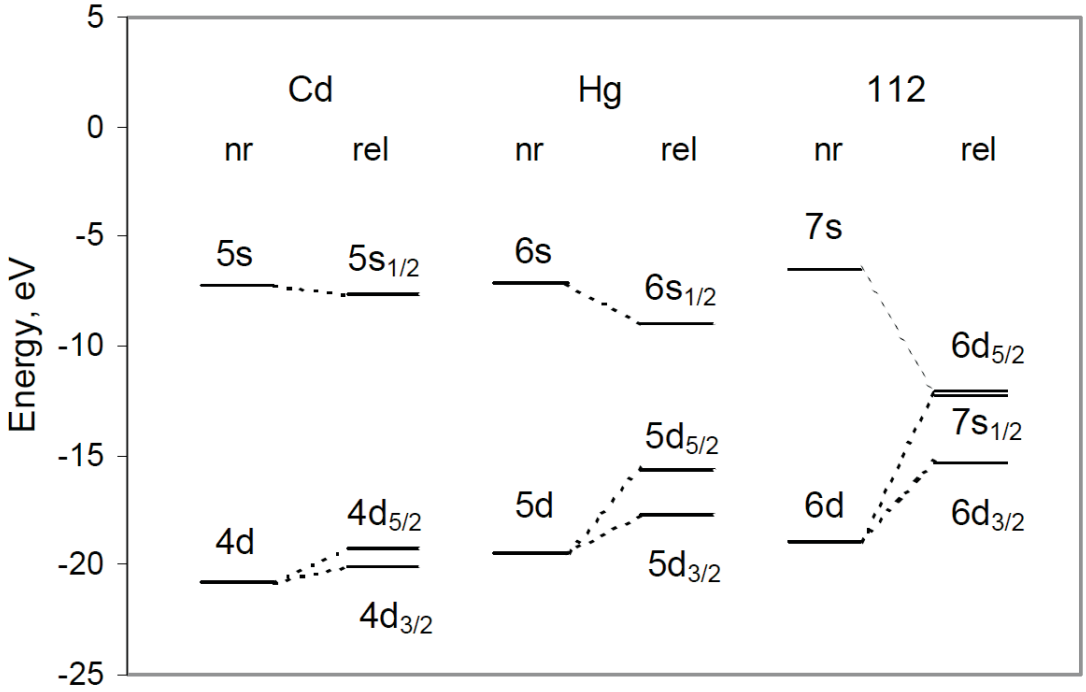

Fig. 1: Relativistic (DF) and nonrelativistic (HF) energy levels of the valence ns and (n-1)d electrons for group-12 elements.

information waiting for a theoretical support. Thus, a larger series of the 4c-DFT calculations was started by us for various heavy-elements compounds and their homologs studied experimentally: gaseous molecules MCl_4 (M = Zr, Hf, and Rf), MCl_5 and MBr_5, $MOCl_3$ and $MOBr_3$ (M = V, Nb, Ta and Db), MF_6, MCl_6, $MOCl_4$, MO_2Cl_2, (M = Mo, W and Sg), MO_3Cl (M = Tc, Re and Bh), and MO_4 (M = Ru, Os and Hs), and complexes in solutions of the type $MO_x(OH)_y(H_2O)_wL_n{}^{z-2x-y-n}$, where M=Zr, Hf and Rf; Nb, Ta and Db; Mo, W and Sg; L = F, Cl, Br. Various electronic structure properties (ionization potentials, electron affinities, electron transition energies, charge density distribution and bonding, geometries) and their trends have been predicted for the transactinide compounds and their lighter homologs.

The influence of relativistic effects on the electronic structures and prop-

erties of the heaviest elements has been studied by comparing results of the relativistic and nonrelativistic calculations. Relativistic effects were shown to increase ionization potentials, theormochemical stability and the stability of the highest oxidation state. They are responsible for a decrease in the bond lengths and increase in covalency. A reason for that is the increasing contribution of the relativistically stabilized and contracted 7s AO, as well as of the expanded 6d AO in bonding. Relativistic effects also define trends in those properties in the transition element groups in going over to the superheavies: e.g., an increase in covalency and in the stability of the maximum oxidation state.

3 Predictions for gas-phase experiments

Predictions of volatility as adsorption on a surface of chromatography column were made using a combination of the relativistic calculations and physicochemical models. Thus, enthalpies of adsorption of MO_3Cl (M = Tc, Re and Bh) [16] and MO_4 (M = Ru, Os and Hs) [17] were predicted with the use of the molecule-slab interaction model based on the theory of physisorption. Excellent agreement with experiment [18] was achieved for group-7 compounds showing that volatility changes as $TcO_3Cl > ReO_3Cl > BhO_3Cl$. The reason for that was shown to be increasing dipole moments in the row of the homologs [16]. For group-8 compounds, the predicted trend is $RuO_4 < OsO_4 < HsO_4$. However, a different trend, $OsO_4 > HsO_4$, was observed experimentally [19], the fact that still needs an explanation.

The study of volatility of element 112 is the most fascinating, since element 112 is expected to be very volatile, almost like an inert gas, due to the closed shell, $6d^{10}7s^2$, and the inaccessibility of the relativistically stabilized 7s electrons for chemical bonding. Experimentally, it is planned to be ad-

sorbed together with its homolog Hg on surfaces of noble metals, e.g., Au. As a first step in the extensive study, bonding in the dimers HgM and 112M (M = Pd, Cu, Ag, Pt and Au) was calculated using the 4c-RGGA DFT method [20]. The difference in the bond strength between HgX and 112X was found to be of about 20 kJ/mol, and the increase in the bond length of about 0.06 Å. Thus, element 112 is expected to be weaker bound with gold than Hg, but not as weak as was assumed earlier. A Mulliken population analysis shows that the decrease in the bond strength form HgX to 112X is a result of the decreasing involvement of the 7s electrons in bonding leading to a diminished 7s(112)-6s(Au) overlap compared to the 6s(Hg)-6s(Au) one. Calculations are now being carried out for Hg and element 112 interacting with large gold clusters using the embedded DFT method [21].

The study of relativistic effects on volatility of element 112 as adsorption of the gold (100) surface [22] has shown that bonding can be decreased or increased depending on the adsorption position. Thus, in the on-top position, relativistic effects decrease the bonding due to the predominant involvement of the relativistically stabilized 7s(112) orbital. On the contrary, upon adsorption in the hollow position, relativistic effects increase bonding due to the involvement of the relativistically destabilized 6d orbitas. As a trend in the group, volatility should change, however, in the same way independently of the adsorption position, i.e., Hg $<$ 112.

Further on, the adsorption temperature, T_{ads}, of element 112, the property that is measured in the gas-phase experiments, was predicted on the basis of the calculated adsorption energy, the vibrational frequency of the adsorption bond with the use of the statistical thermodynamic functions for the adsorption-desorption equilibrium [23]. T_{ads}(112) was found to be about 100 degrees below that of Hg, which means that element 112 should behave

somehow between Hg and Rn. This prediction is valid only for the ideal Au(100) surface for which the calculations were performed. Any deviation from ideal conditions would lead to the formation of the van der Waals bond by element 112 and a shift of T_{ads} to the area of T_{ads} of Rn.

4 Predictions for liquid chromatography experiments

Complex formation is another important property of the heaviest elements. It is known to increase in the transition element groups with increasing Z. In experiments, trends in the complex formation of homologs are studied by observing sequences in their extraction from aqueous solutions by organic solvents, or their sorption by resins [24].

Theoretically, trends in the complex formation were predicted by defining trends in the free energies of the complex formation reactions in rows of homologs. Since in aqueous solutions the complex formation is competing with hydrolysis, reactions of the following type were considered

$$x\mathrm{M(H_2O)}^{\mathrm{z+}}_{\mathrm{W0}} + y\mathrm{OH}^- + i\mathrm{L}^- \Longleftrightarrow \mathrm{M}_x\mathrm{O}_u(\mathrm{OH}_{z-2u}(\mathrm{H_2O})_w\mathrm{L}_a^{(\mathrm{xz-y-i})+}$$

Using a model [25] which defines the free energy change of a reaction via changes in the covalent and ionic contributions of the reactants and products, as well as in the entropy term, a large number of complex formation reactions were considered for group-4 through 6 elements. The calculations of the electronic structures of the complexes were performed with the use of the 4c-DFT method. The complex formation and also trends in the groups in going over to the transactinides were shown to be influenced by various factors such as acid concentration and pH of the solution. Thus, especially in the presence of hydrolysis, the increasing trend to the complex formation from the 4d to the 5d elements can be reversed in going over to the 6d elements.

For example, the calculations show that the complex formation of the group-5 elements in HF, HCl and HBr solutions at intermediate concentrations has the following trend: Nb > Db > Ta [25]. A reversal of the trends was also shown for group-6 elements in HF solutions at some acid concentrations [26]. Thus, for example, in very dilute HF solutions, the trend in the complex formation is W > Sg > Mo, while for concentrated HF solutions the trend is Mo < W $\ll$ Sg. The theoretically predicted trends were confirmed by experiments on the extraction of group-4 elements from HF and HCl solutions and of group-5 elements from HF, HCl and HBr solutions [24]. Experiments for the group-6 elements (Sg) are still to be conducted in the near future. Presently, adsorption of elements 112 and 114 on various metal surfaces are in the focus of our interests. Aqueous chemistry of elements heavier than Sg is also to be considered in future.

References

[1] M. Schädel, ed. The Chemistry of Superheavy Elements, Kluwer, 2003.

[2] P. Schwerdtfeger, ed. Relativistic Electronic Structure Theory, Part. 1. Fundamentals, Elsevier, 2002.

[3] P. Schwerdtfeger, ed. Relativistic Electronic Structure Theory, Part. 2. Applications, Elsevier, 2004.

[4] U. Kaldor, E. Eliav, A. Landau, Ref. 2, p. 81.

[5] Ch. van Wüllen, Ref. 2, p. 598.

[6] Y. S. Lee, Ref. 2, p. 352.

[7] V. Pershina, Chem. Rev. 96, 1977 (1996).

[8] V. Pershina, Ref. 2, p. 1.

[9] V. Pershina, Ref. 1, p. 31.

[10] S. Varga, et al., Phys. Rev. A 59, 4288 (1999).

[11] T. Jacob, et al., Eur. Phys. J. D 16, 257 (2001).

[12] K. S. Pitzer, J. Chem. Phys. 63, 1032 (1975).

[13] P. Pyykkö, Chem. Rev. 88, 563 (1988).

[14] B. Fricke, Struct. Bond. 21, 89 (1975).

[15] S. Schwerdtfeger and M. Seth, In: Encyclopedia on Calculational Chemistry, Wiley, N. Y. (1998) Vol. 4, 2480.

[16] V. Pershina and T. Bastug, J. Chem. Phys. 113, 1441 (2000).

[17] V. Pershina, et al., J. Chem. Phys. 115, 1 (2001).

[18] R. Eichler, et al., Nature, 407, 63 (2000).

[19] Ch. Düllman, et al., Nature, 418, 859 (2002).

[20] V. Pershina, et al., Chem. Phys. Lett. 365, 176 (2002).

[21] C. Sarpe-Tudoran, et. al., Eur. Phys. J. D 24, 65 (2003).

[22] V. Pershina and T. Bastug, Chem. Phys. 311, 139 (2005).

[23] V. Pershina, et al., Nucl. Phys. A 734, 200 (2004).

[24] J. V. Kratz, Ref. 1, p. 159.

[25] V. Pershina, Radiochim. Acta 80, 75 (1998).

[26] V. Pershina. Radiochim. Acta 92, 455 (2004).

Coinage Metal Halide Oligomers

Robert P. Krawczyk, Tilo Söhnel, Holger Hermann, and Peter Schwerdtfeger

Institute of Fundamental Sciences, Massey University (Albany Campus), Private Bag 102904, North Shore MSC, Auckland, New Zealand

Group 11 metal halides exhibit interesting solid-state and gas-phase oligomer structures. Further on, the coinage metal halides have solid-state structures which differe dignificantly from the structures of small MX oligomers. In order to understand the nucleation process, the question arises at which number of MX units the structure of the clusters changes. In this study, we will give a brief introduction in the structures of solid group 11 metal halides and the structures of group 11 metal halides clusters. The structure and stability of $(MX)_n$ moieties (with $n \geq 4$) and the influence of phosphine coordination to the tetrameric group 11 chlorides and bromides will be investigated.

In the solid state a variety of different modifications can be found. The copper(I) halides CuCl, CuBr, and CuI crystallise in a 4-fold coordinated zinc blende structure, see Fig. 1(a). Solid CuF is unknown, because it easily disproportionates into CuF_2 and solid copper, while CuF is stable in the gas phase[1]. There is also a high pressure modification of CuCl and CuBr which has a rock salt structure, see Fig. 1(b).

In contrast to Cu, silver fluoride, chloride, and bromide crystallise at

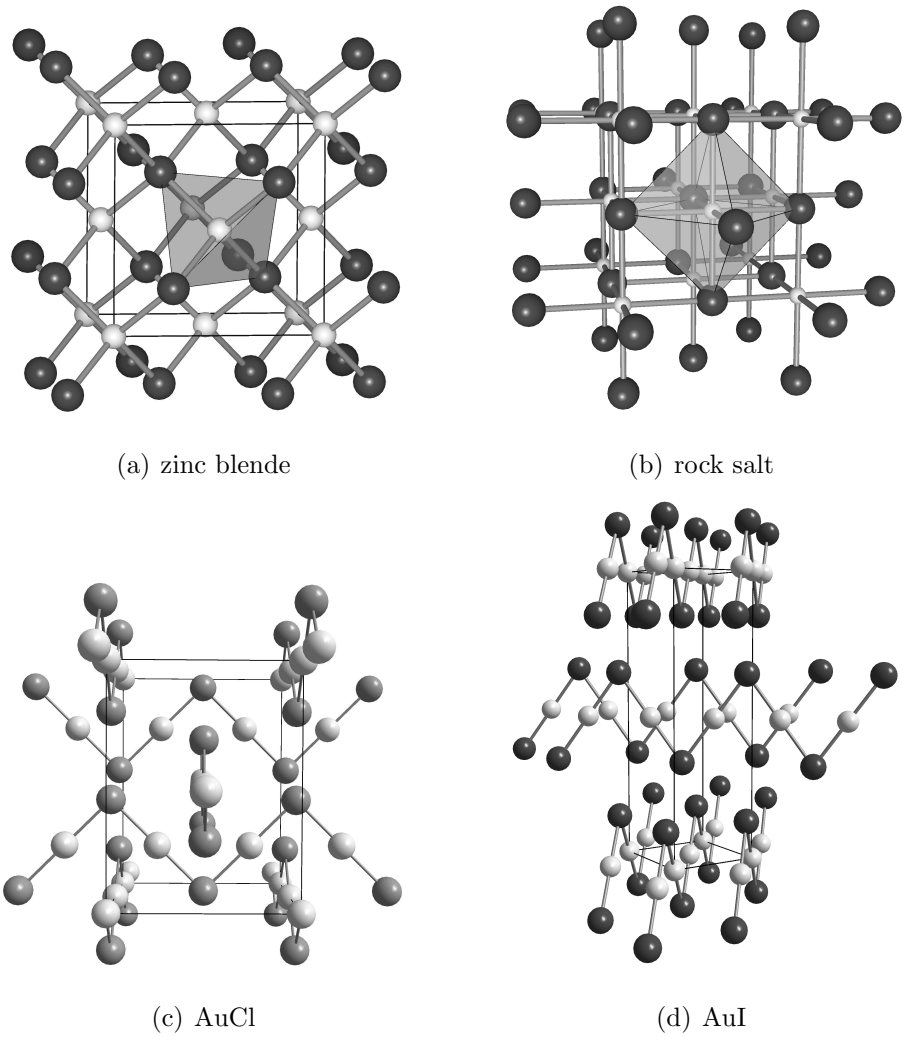

(a) zinc blende (b) rock salt

(c) AuCl (d) AuI

Fig. 1: Solid state structures in which coinage metal halides can crystallise.

room temperature and low pressure in the simple cubic rock salt structure (Fig.1(b)). For AgI several different low pressure modifications are known: a cubic zinc blende modification, a hexagonal wurzite modification, and a high-temperature cubic modification.

The most interesting situation can be found in the gold halides and their extraordinary structures. Gold halides crystallise in unexpected chainlike tetragonal structures, as shown in Figs. 1(c) and 1(d), which cannot be so easily understood[2, 1]. These halides show linear AuX_2 units with short Au–Au distances that have been ascribed to aurophilic interactions.

The coinage metal halides show a tendency to form clusters. These clusters have short metal–metal bonds. In silver and copper the metal–metal interactions are about 4 kcal/mol, whereas in the gold compounds the metal–metal interaction can be as larger as 7 to 12 kcal/mol[3, 4]. Correlation and relativistic effects play an important role in these metallophilic interactions[3, 5, 6]. The maximum of the influence of relativistic effects on the radii of the orbitals for gold[7, 8] is responsible for changing the coordination chemistry of gold compared to the other coinage metals. Gold has different structures in comparison to Cu(I) and Ag(I) halides. The former preferring shorter gold–gold contacts, the structures of the latter are governed by electrostatic contributions.

The existence of group 11 halides oligomers has been known for over 100 years[9]. In the vapour of CuCl conclusive evidence for oligomeric molecules has been found using a variety of spectroscopic techniques[10, 11, 12, 13, 14]. Up to pentameric units can be found in the vapour. Under most conditions the most dominant species is the tetramer[15]. This kind of metal–halide clusters can be useful in low-pressure CVD processes[16].

Electron-donating ligands change the structural M_4X_4 units of the group

11 metal halides completely. In the solid state the Cu(I) and AG(I) halide phosphanes tend to oligomerise in dimeric and tetrameric structures[17]. From the two tetrameric structures found, one is cubic and the other one has a ladder or step like structure. In contrast, Cl–Au–PR_3 oligomerises in the solid state by keeping the linear P–Au–Cl structure intact and forming Au–Au bonds[18]. The phosphane ligands tend to stabilise the aurophilic interactions, often inducing the formation of larger clusters.

The calculations were performed with Gaussian98 and Gaussian03. For a survey of different cluster structures and energies the density functional method has been used. The B3LYP functional in combination with Los Alamos pseudopotentials and double-ζ valence basis sets[19] has been used. In order to reduce computational costs PH_3 has been used as a model ligand for the phosphanes. Some very closely lying structures have been optimised further using a larger basis set (for the specification of the basis set see [6, 20]) in connection with a small-core Stuttgart pseudo-potential[21]. For these calculations the BPW91 functional has been used, because it gave more accurate results for the MX diatomics.

The interaction in the cluster consist largely of dipole–dipole interactions as the MX units have large dipole moments[22]. For the calculation of the influence of dipole interactions on the stability of the $(MX)_4$ clusters, a simple electrostatic model was adopted. For calculating the total energy, the dipole–dipole potential has to be augmented with a repulsive term, in order to avoid the collapse of the cluster from the purely attractive dipole–dipole interactions. We assumed the repulsion to be of Lennard-Jones type. Thus,

the energy between two dipoles is given by

$$V(\vec{\mu}_1, \vec{\mu}_2) = \frac{\vec{\mu}_1\vec{\mu}_2}{r^3} - \frac{(\vec{\mu}_1\vec{r})(\vec{\mu}_2\vec{r})}{r^5} + \sum_{i<j} \frac{A_{ij}}{r_{ij}^{12}}. \quad (1)$$

$\vec{\mu}_i$ is the dipole moment and r is the distance between the midpoints of the dipoles. The r_{ij} are the distances between the atoms. The parameter A is chosen such ($A = 0.12403101$) that the equilibrium distance between two parallel dipoles is at the unit length of $r_e = 1$ au. The cluster geometry was optimised by numerical gradient techniques[23].

All of the structures found in the optimisation process are shown in Fig. 2. The energies of the structures are given in Tab. 1. It can be seen that the structures **1** and **2** have the lowest energy in agreement with a number of theoretical studies[24]. In both structures the halide atoms sit at the corners of a square and the metal atoms are in the middle of the edges. The D_{2d} arrangement as shown by **2** is derived from the D_{4h} structure by folding the ring along a diagonal. The energy difference between **1** and **2** is very small in all cases (≤ 0.4 kcal/mol at B3LYP level of theory). Therefore, the system will behave dynamically at room temperature. In gas-phase electron diffraction experiments at room temperature there may be no evidence for this symmetry breaking. Using the larger basis set and the BPW91 functional it was found that **2** is the energetically favoured structures with the sole exception CuI. For the CuI tetramer the D_{2d} structure represents a first-order transition state to a weakly distorted D_2 geometry. In the D_2 structure the four copper atoms form a planar rhombic Cu_4 core.

The tetrahedral T_d structure (structure **3** in Fig. 2) consists of MX units forming a cube. It more closely resembles the solid-state structure of copper and silver halides. The T_d structure lies between 10 and 25 kcal/mol higher

	1	**2**	**3**	**4**	**5**	**6**
CuF	0.0	0.2	41.7	37.1		36.2
CuCl	0.3a	0.0	23.0	18.6		24.0
CuBr	0.2	0.0	16.7	13.3		18.7
CuI	1.2a	0.0	10.6	8.7		12.5
AgF	0.6b	0.0	12.9	24.5		28.9
AgCl	0.0	0.4	11.5	15.9		23.2
AgBr	0.0	0.0	11.1	13.0		d
AgI	0.1a	0.0	10.8	10.4		d
AuF	0.6a	0.0	82.7	47.8	39.7	37.5
AuCl	0.0	0.4	63.0c	28.0	25.1	23.7
AuBr	0.1a	0.0	57.9c	24.4	21.5	24.4
AuI	0.0	0.0	55.9c	21.2	18.6	47.8

Tab. 1: Energies of the Coinage Metal(I) Halide Tetramers relative to the global Minimum Structure at the B3LYP/LANL2DZ level of Theory (kcal/mol). a marks a transition state (TS) to structure **2**, b is a TS to the D_{2h} structure, c is a TS to structure **5**, and d is a TS to structure **4**.

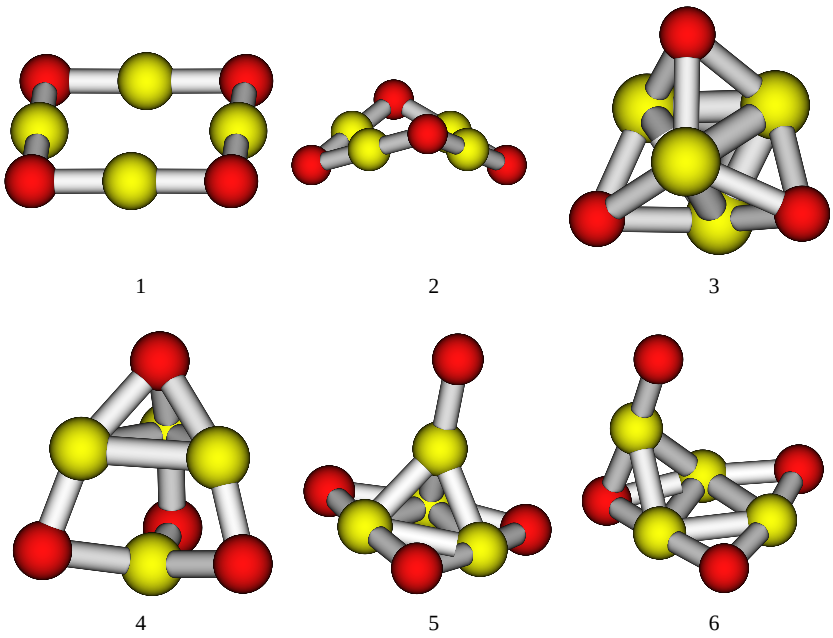

Fig. 2: Minimum structures of group 11 metal(I) halide tetramers, M_4X_4, at the B3LYP level of theory.

in energy than the ring structures. For the gold halide tetramers and copper fluoride tetramer this tetrahedral arrangement is particularly unfavoured. Structure **4** which is of C_{3v} symmetry, can be seen as a tetrahedron of metal atoms with three halide atoms attached to the edges and one halide atom is face-centered. Both structures **3** and **4** are in the same energy range.

Structures **5** and **6** both have a $(MX)_3$ ring structure as an important building block. The $(MX)_3$ ring is the global minimum structure for all of the group 11 halide trimers[25]. In structure **5**, the gold end of the fourth MX unit is above the ring, thus forming a gold tetrahedron. In this case, an atom-in-molecule analysis, according to Bader, clearly reveals Au–Au interactions. However, **5** is only a local minimum structure for the gold halide tetramers and does not represent a minimum for copper and silver. This clearly shows the preference of gold to form metallophilic interactions. As can be seen from

gold iodide, which is 18.6 kcal/mol higher in energy than **1**, and becomes even less favoured in the smaller halides, softer ligands lead to stronger aurophilic interactions. In structure **6** a fourth MX molecule is connected to a halide in the corner of the $(MX)_3$ ring structure. This structure is not very stable and often represents only a transition state leading to structure **5**.

In contrast to these findings the dipole interaction potential (1) clearly prefers, as expected, the cubic arrangement **3** over the ring structure. A plot of (1) is shown in Fig. 3. The ring structure is therefore strongly stabilised by additional covalent interactions. The energy of the ring-like structures remains fairly independent of the magnitude of the dipole moment. The cubic structures show a strong dependence on the dipole moment as can be seen from Fig. 3. It can also be seen that for very weak dipole moments there is only a small energy difference and it may be possible that ring-like structures are favoured for weak dipole moments. Silver chloride crystallises in a rock-salt structure, showing that with the addition of more MX units, the dipole interactions become more dominant. A change from the ring to the cubic structure is observed but the exact cluster size has yet to be determined. First preliminary calculations on higher coinage metal halides have shown that Ag_6F_6, see Fig. 4, has no imaginary frequencies and is in the same energy range as the ring-like structures. From this preliminary results it can be concluded that the transition to the solid-state structures may occur at six MX moieties.

The coordination of phosphane completely changes the structure of the these tetramers, see Fig. 5. The ring structures found for the halides do not represent a minimum on the potential energy surface. The copper and silver chloride and bromide phosphane tetramers have minima for a heterocuban structure of T_d symmetry (top/left structure in Fig. 5. The step-

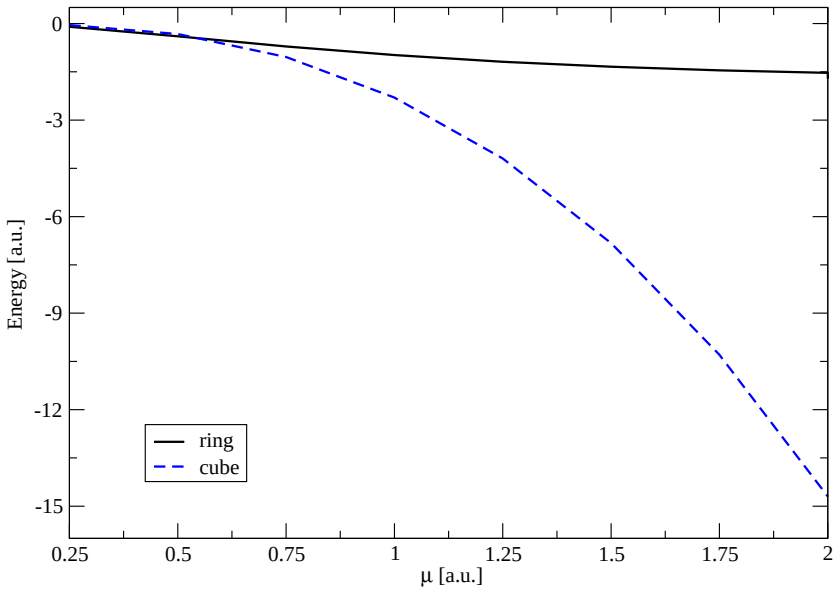

Fig. 3: Dependence of the dipole cluster energy on the dipole moment. Energy and dipole moment is given in arbitrary units. The solid line shows the energy of a ring-like structure, the dahed line shows the energy of a cube-like structure. At each point the energy of the cluster has been optimised.

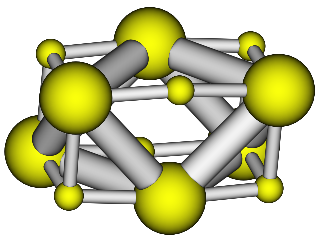

Fig. 4: Optimised structure of Ag_6F_6 at the B3LYP level of theory.

cluster structure of C_i symmetry (bottom/left structure in Fig. 5) is about 9 to 12 kcal/mol higher in energy than the T_d structure. The gold chloride and bromide phosphane tetramers have different structures compared to the copper and silver homologous. The above mentioned structures do not represent minima for gold. In gold the X–Au–P unit remains linear in all cases, therefore having the most possible metal–metal interaction. In the top/right structure in Fig. 5, the four gold atoms are in a square planar arrangement with the halide and phosphane ligands alternating above and below the plane. The linear structure (bottom/right in Fig. 5) is about 5 to 10 kcal/mol higher in energy.

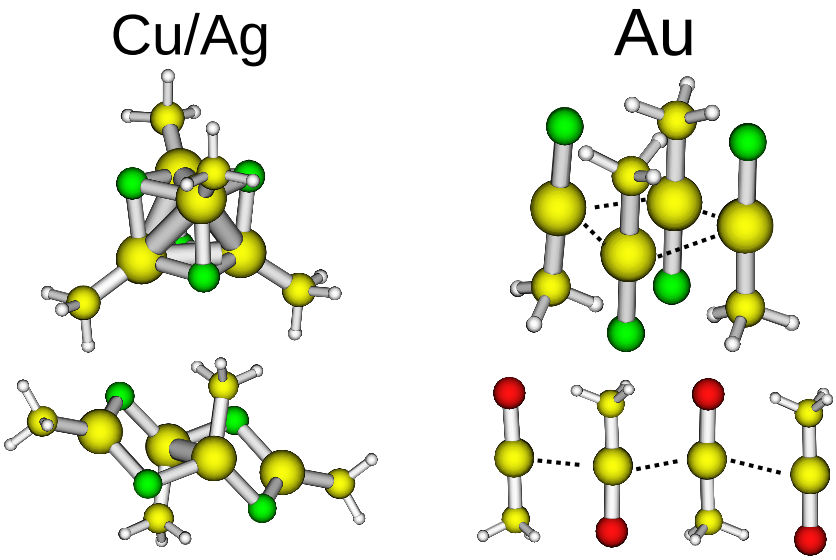

Fig. 5: Selected minimum structures of group 11 metal(I) phosphane halide tetramers.

In conclusion the coinage metal halide tetramers adopt ring-like structures. From the hexamers onward a change in structure is anticipated. At the DFT level of theory and using the atoms-in-molecules method no clear bond path between the metals of the ring-like structures could be found.

However, at the perturbation theory level of theory, aurophilic interactions were found for Au_4I_4. The very similar structures obtained for all group 11 halide tetramer clusters suggest that the well known differences for the solid-state structures between Cu and Ag on one hand and the Au halides on the other hand are not evident. Preliminary calculations show that they may appear for the hexamers.

While all coinage metal halide tetramers have ring-like structures, the phosphane complexes of group 11 chlorides and bromides are not stable in this configuration. Additionally the gold tetramers have a totally different structure. The gold phosphane halide tetramers retain the linearity of the X–Au–P units.

Acknowledgement

This work was supported by the Alexander von Humboldt Foundation and the Marsden Fund administered by the Royal Society of New Zealand. We are grateful to the Allan Wilson Centre for large amount of computer time on their high-performance parallel computer HELIX.

References

[1] T. Söhnel, H. Hermann, and P. Schwerdtfeger. *J. Phys. Chem. B*, **2004**. *109*, 526.

[2] T. Söhnel, H. Hermann, and P. Schwerdtfeger. *Angew. Chem. Int. Ed.*, **2001**. *40*, 4381.

[3] H. Schmidbaur. *Gold Bull.*, **2000**. *33*, 3.

[4] P. Pyykkö. *Angew. Chem. Int. Ed.*, **2002**. *41*, 3573.

[5] N. Runeberg, M. Schütz, and H.-J. Werner. *J. Chem. Phys.*, **1999**. *110*, 7210.

[6] P. Schwerdtfeger, R. P. Krawczyk, A. Hammerl, and R. Brown. *Inorg. Chem.*, **2004**. *43*, 6707.

[7] P. Pyykkö. *Chem. Rev.*, **1988**. *88*, 563.

[8] P. Pyyköö. *Angew. Chem.*, **2004**. *116*, 4512.

[9] V. Meyer and C. Meyer. *Cehm. Ber.*, **1879**. *12*, 1112.

[10] L. Brewer and N. Lofgren. *J. Am. Chem. Soc.*, **1950**. *72*, 3038.

[11] M. Vanliere and T. C. DeVore. *High Temp. Sci.*, **1984**. *18*, 185.

[12] M. Guido, G. Balducci, G. Gigli, and M. Spoliti. *J. Chem. Phys.*, **1971**. *55*, 4566.

[13] A. Potts and M. L. Lyus. *J. Elxtr. Spectr. Relat. Phen.*, **1978**. *13*, 305.

[14] P. R. Koren, F. Chen, and E. R. Davidson. *Mol. Phys.*, **2001**. *99*, 1329.

[15] S. Locmelis and M. Binneweis. *Z. Anorg. Allg. Chem.*, **1999**. *625*, 1578.

[16] N. Bourhila, J. Torres, J. Palleau, C. Bernard, and R. Madar. *Microelectron. Eng.*, **1997**. *33*, 25.

[17] G. Wilkinson, R. G. Gillard, and J. A. McCleverly (editors). *Comprehensive Coordination Chemistry*, volume 5. Wiley, **1987**.

[18] M. Melnik and R. V. Parish. *Coord. Chem. Rev.*, **1986**. *70*.

[19] P. J. Hay and W. R. Wadt. *J. Chem. Phys.*, **1985**. *82*, 299.

[20] P. Schwerdtfeger, R. Brown, J. K. LAerdahl, and H. Stoll. *J. Chem. Phys.*, **2000**. *113*, 7110.

[21] A. Bergner, M. Dolg, W. Kuechle, H. Stoll, and H. Preuss. *Mol. Phys.*, **1993**. *80*, 1431.

[22] M. Guichemerre, G. Chambaud, and H. Stoll. *Chem. Phys.*, **2002**. *280*, 71.

[23] *http://www.gnu.org/software/gsl/*.

[24] J. M. L'Hermite, F. Rabilloud, P. Labastie, and F. Spiegelman. *Eur. Phys. J. D: At., Mol. Opt. Phys.*, **2001**. *16*, 77.

[25] M. Hargatti, P. Schwerdtfeger, R. Balazs, and R. Brown. *Chem. – Eur. J.*, **2003**. *9*, 327.

Catalytic Activity of Au(III)

Matthias Lein and Peter Schwerdtfeger

Institute of Fundamental Sciences, Massey University (Albany Campus), Private Bag 102904, North Shore MSC, Auckland, New Zealand

1 Introduction

Although traditionally considered to be of only moderate catalytic activity, gold compounds have found various applications in the realm of modern catalytic chemistry. Still, the vast majority of known catalysed reactions involving gold are heterogeneous reactions on gold surfaces and only a small fraction of attention is given to the growing field of homogeneously gold-catalysed organic chemistry. The special position gold, as a precious metal and as a non-toxic compound, makes it particularly interesting for the use as a catalyst. In addition, the unique physical properties of gold, which stem mostly from the large relativistic effects in this element, are of methodological interest. Gold often reacts very differently in comparison to the lighter homologues, copper and silver. The differences within those group-11 metals may hold the key to the understanding of the catalytic activity of gold. Compared to other metals commonly used in catalysis, notably ruthenium or rhodium, gold is moderately priced. It may be worthwhile to explore the possibility to replace those metals with equally catalytically active gold

complexes in order produce more efficiently and in a more ecologically sustainable way. Lastly, the possibility that gold may open the way to new, previously unknown or inefficient, synthetic routes, must be considered. A recent review on homogeneous catalysis by gold can be found in [1].

2 Methods

The geometries of all molecules have been optimized at the gradient-corrected DFT level using the exchange functional of Becke[2] in conjunction with the correlation functional of Perdew[3] (BP86) with the Los Alamos basis-set/pseudo-potentials LANL2DZ to determine the shape of locate local minima. The obtained structures are then confirmed by re-optimisation at the Møller Plesset[4] (MP2) level of theory with a Stuttgart type pseudo-potential [5] and corresponding valence basis set for gold and Dunning type triple-ζ basis set[6] for the light elements. CCSD(T) single point calculations at the geometries obtained at the MP2 level are performed to ensure correct energetic. All calculations are performed using Gaussian03[7]

3 Calculations

Because if the structural simplicity and the relatively "well-behaved" electronic structure Gold(III)-compounds are particularly appealing for theoretical investigations. Although Gold(III)-catalysts with large organic ligands are used throughout the whole range of applications, most reactions can be done by using Gold-trihalides AuX_3. Particularly $AuCl_3$ catalyses a wide variety of organic reactions, ranging from oxidation reaction [8] to complex ring re-arangements [9] and nucleophilic additions [10].

One possible reaction is the addition of oxygen-nucleophiles like water or

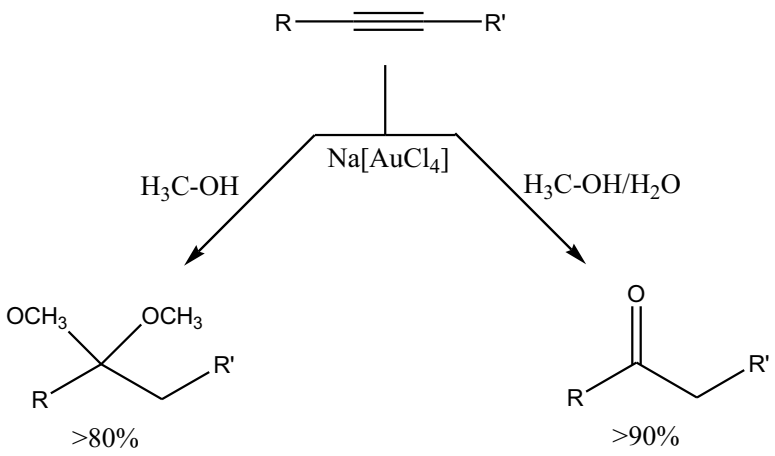

Fig. 1: Addition of oxygen-nucleophiles to alkynes under various conditions

alcohols to form ketones and ketals respectively as shown in Figure 1. In order to model the energetic profile of this reaction the structures of both the un-coordinated as well as the $AuCl_3$ coordinated educt were obtained and compared with the strucures of the product-complex.

The obtained data will be discussed and compared to the experimental observations. The possible influence of the solvent, both as a polarising medium and as reactant will be discussed.

4 Acknowledgement

This work was supported by a Marsden Fund administered by the Royal Society of New Zealand. We are grateful to the Allan Wilson Centre for large amount of computer time on their high-performance parallel computer HELIX and to the Institute of Information and Mathematical Sciences for providing excellent service maintaining the high-performance parallel computer DOUBLEHELIX.

References

[1] A. S. K. Hasmi. *Gold Bull.* **2004**, *37/1-2*, 51

[2] A. D. Becke. *Phys. Rev. A.* **1988**, *38*, 3098.

[3] J. P. Perdew. *Phys. Rev. B.* **1986**, *33*, 8822.

[4] C. Møller, M. S. Plesset *Phys. Rev.* **1934**, *46*, 618.

[5] a) W. Kuechle, M. Dolg, H. Stoll, H. Preuss *Mol. Phys.* **1991**, *74*, 1245. b) A. Bergner, M. Dolg, W. Kuechle, H. Stoll, H. Preuss *Mol. Phys.* **1993**, *80*, 1431. c) M. Dolg, U. Wedig, H. Stoll, H. Preuss *J. Chem. Phys* **1987**, *86*, 866.

[6] a) T. H. Dunning, Jr. *J. Chem. Phys* **1989**, *90*, 1007. b) D. E. Woon, T. H. Dunning, Jr. *J. Chem. Phys* **1993**, *98*, 1358.

[7] M. J. Frisch et al. *Gaussian 03 Rev. C2.;* Gaussian, Inc.: Pittsburgh PA, United States of America, 1998.

[8] a) F. Gasparrini, M. Giovanolli, D. Misiti, G. Natile, G. Palmieri. *Tetrahedron* **1983**, *39*, 3181 b) F. Gasparrini, M. Giovanolli, D. Misiti, G. Natile, G. Palmieri. *Tetrahedron* **1984**, *40*, 165

[9] a) A. S. K. Hashmi, T. M. Trost, J. W. Bats. *J. Am. Chem. Soc.* **2000**, *122*, 11555 b) A. S. K. Hashmi, T. M. Trost, J. W. Bats. *Catal. Today* **2001**, *72*, 19 c) A. S. K. Hashmi, L. Ding, J. W. Bats, P. Fischer, W. Frey. *Chem. Eur. J.* **2003**, *9*, 4339

[10] a) Y. Fukuda, K. Uchimoto. *J. Org. Chem.* **1991**, *56*, 3729 b) Y. Fukuda, K. Uchimoto. *Bull. Chem. Soc. Jpn.* **1991**, *64*, 2013 c) Y. Fukuda, K. Uchimoto. *Chem. Abstr.* **1992**, *117*, 150554

Density Functional Study of Structural and Physical Properties of Gold and Cesium Clusters

Behnam Assadollahzadeh

Institute of Fundamental Sciences, Massey University (Albany Campus), Private Bag 102904, North Shore MSC, Auckland, New Zealand

1 Abstract Au-Cluster

Atomic clusters bridge the gap between small molecules and bulk materials, in fact it can be said that they constitute a new type of material, since they have chemical and physical properties which are fundamentally different from those of the relevant bulk solid. Gold clusters make no exception. Whereas gold in its bulk form is one of the most inactive metals, it exhibits fascinating and unconventional chemical and physical properties as its dimensions are reduced to the nanoscale. This leads to a wide range of applications.

Due to applications of gold clusters and nanoparticles in nanostructured materials, electronic devices and catalysts[1], there is a wide and great interest in investigating the chemical and physical properties of such clusters[2][3]. This interest is reflected by a considerable amount of experimental and theoretical work on gold clusters. However, very important fundamental ques-

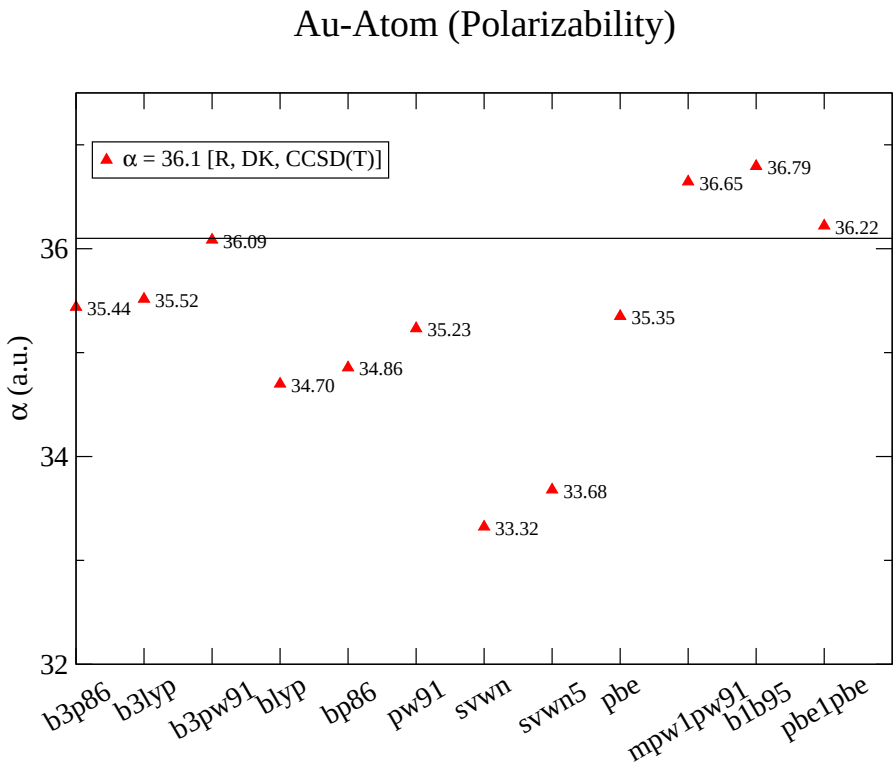

Fig. 1:

tions still remain unanswered.

For instance: When does the transition from 2D to 3D structures occur? Is there any growth pattern for the minima structures as a function of cluster size? How can one obtain the global minima structures?

In order to obtain and to predict the clusters' properties, their geometrical structures must be characterized. Investigating these properties as a function of size will lead to a better understanding of how they evolve towards bulk properties.

The GAUSSIAN 03 package of quantum chemical programs was used throughout[4]. All computations of gold clusters reported were carried out using the LANL2DZ or LANL2MB basis sets, respectively, as a preliminary optimization. The local density approximation (LDA) to the exchange-

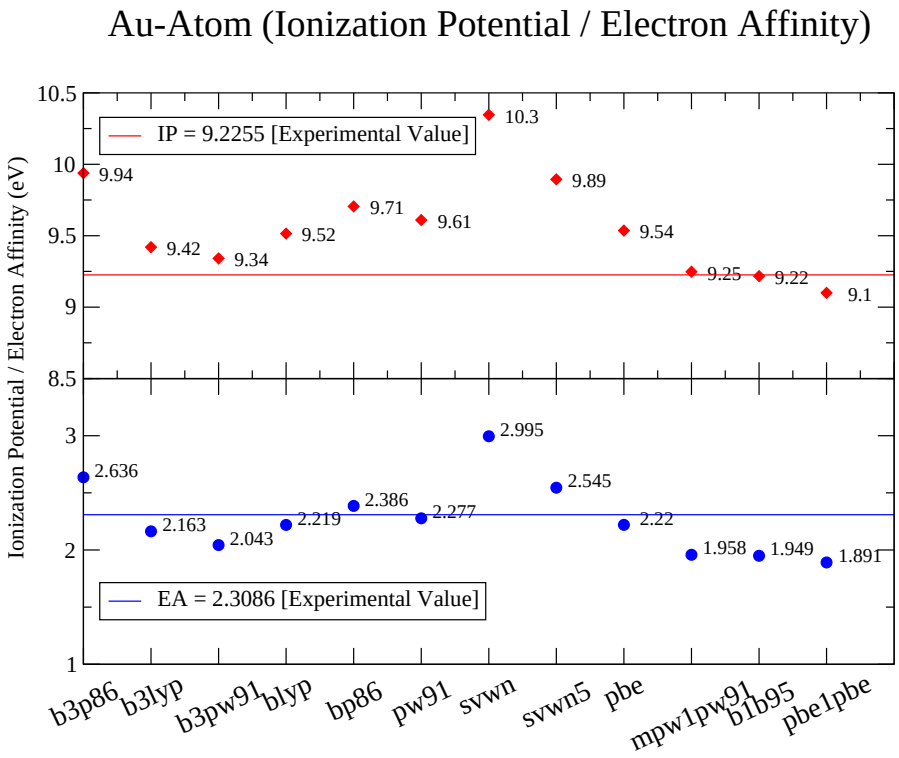

Fig. 2:

correlation functional utilized in the parametrization suggested by Vosko *et al.* was used for calculating the gold structures. Frequency calculations were carried out for each optimized structure to confirm it is a minimum. The atomic and dimer properties of gold were computed using the latest Stuttgart relativistic effective core potential (RECP) and corresponding basis set, which was modified[5], as well as a much smaller basis set optimized in our group combined with another Stuttgart RECP.

In this work a series of new and fascinating minima structures of gold clusters ranging from Au_5 to Au_{20} were found Most of these structures were obtained by random starting geometries. The planar to three-dimensional structural transition is expected to be at a cluster size of 9 or 10 atoms, respectively. Furthermore, the static dipole polarizability, electron affinity and

ionization potential of the gold atom and dimer were accurately calculated depending on a variety of DFT-functionals. Further work will involve the employment of our modified basis sets into the optimization of the lowest lying minima-energy gold clusters and the calculation of their properties.

1.1 Properties of Atomic Gold

A wide range of DFT-functionals was employed to compute the static dipole polarizability, vertical electron affinity and vertical ionization potential of the gold atom.

The values obtained with the hybrid functionals b3pw91 and pbe1pbe deviate only insignificantly from the much more computer-time demanding relativistic all-electron calculation at the coupled cluster level[6], which can be regarded as a reference value.

Comparison of the calculated ionization potential and electron affinity with experimental outcomes[6] shows that the b3pw91 functional also yields satisfactory results for these properties.

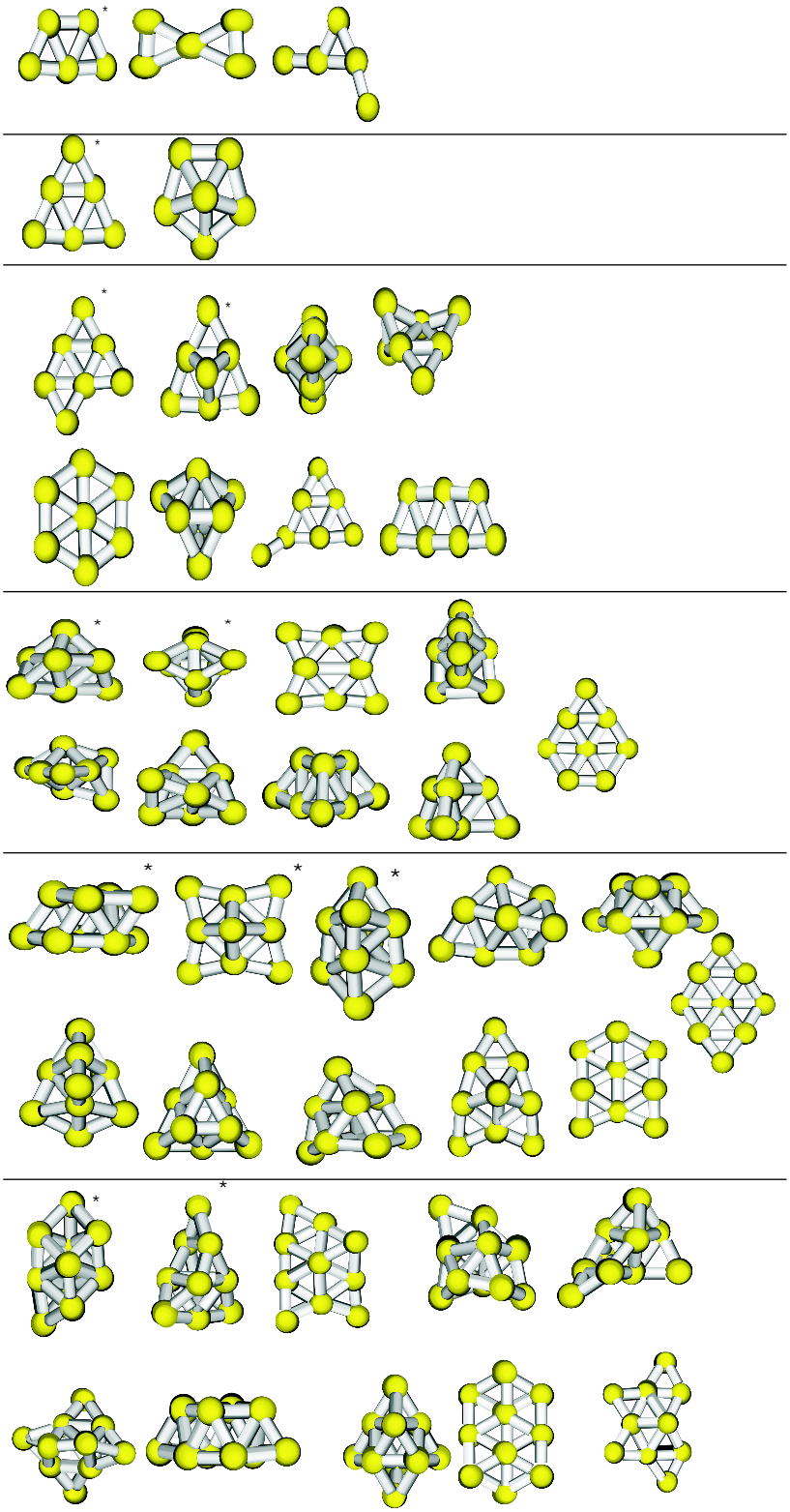

Fig. 3: Selected Isomers of Au_5, Au_6, Au_7, Au_8, Au_9, Au_{10}.

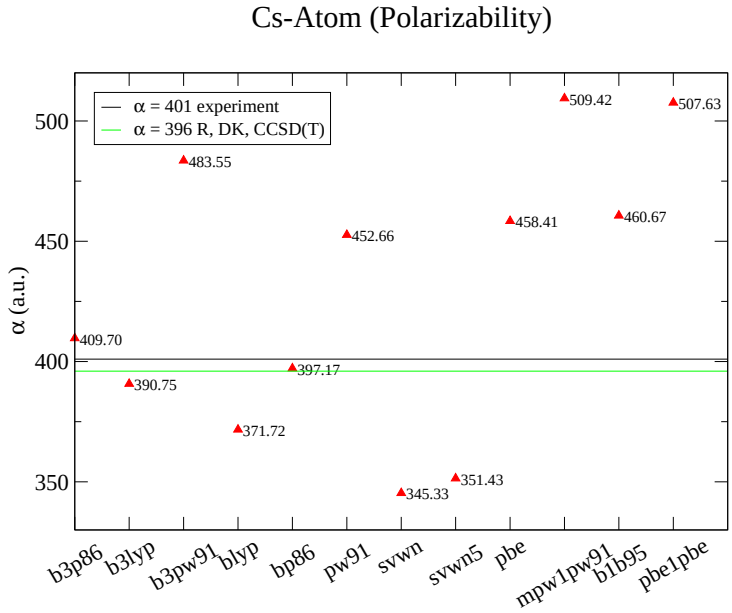

Fig. 4:

2 Abstract Cs-Cluster

Cesium clusters have by far not reached as much interest as gold clusters have. Up to date there is no chronological theoretical investigation of the properties and minima geometries of cesium clusters. All computations of cesium clusters reported were carried out using a basis set optimized in our group combined with an 9 valence electron RECP and the generalized gradient approximation (GGA) with the exchange-correlation functional parametrized by Becke and Perdew (BP86).

The following figure compares the calculated static dipole polarizability of atomic cesium, as a function of the DFT-functional, with the experimental and the relativistic all-electron value at the couple-cluster level (CCSD(T))[7]. The very satisfying value obtained with BP86 deviates less than 1 per cent from the experimental value.

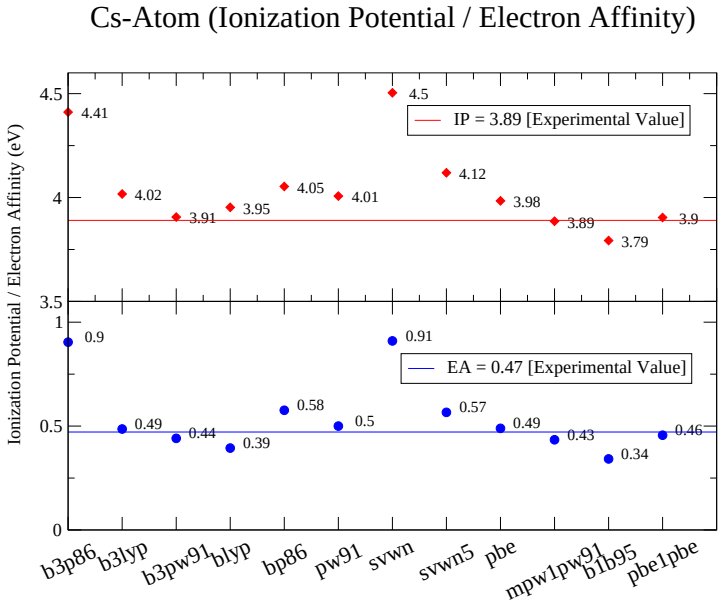

Fig. 5:

2.1 Properties of Atomic Cesium

Comparison of the vertical ionization potential and vertical electron affinity with experimental values[8], [9], shows that BP86 yields only reasonable results. The agreement with experimental values is very satisfactory with the functionals pbe1pbe and p3pw91, respectively.

The following cesium minimum structures were obtained from Lennard-Jones starting geometries.

References

[1] A. V. Walker, J. Chem. Phys. **122**, 094310 (2005)
and references therein

[2] E. M. Fernández, J. M. Soler, I. L. Garzón, L. C. Balbás,
Phys. Rev. B **70**, 165403 (2004)

[3] V. Bonačić-Koutecký, J. Burda, R. Mitrić, M. Ge,
J. Chem. Phys. **117**, 3120 (2002)

[4] M. J. Frisch, G. W. Trucks, H. B. Schlegel et al., GAUSSIAN 03 (Gaussian, Inc., Pittsburgh, PA, 2003)

[5] http://www.theochem.uni-stuttgart.de/pseudopotentials/clickpse.en.html

[6] Pekka Pyykkö, Angew. Chem. Int. Ed. **43**, 4412 (2004)

[7] I. Lim, P. Schwerdtfeger, B. Metz, H. Stoll, J. Chem. Phys. (*in press*)
J. M. Amini, H. Gould, Phys. Rev. Lett. **91**, 153001 (2003)

[8] E. Eliav, M. J. Vilkas, Y. Ishikawa, U. Kaldor, Chemical Physics **311**, 163 (2005)

[9] http://www.webelements.com/webelements/elements/text/Cs/ionz.html

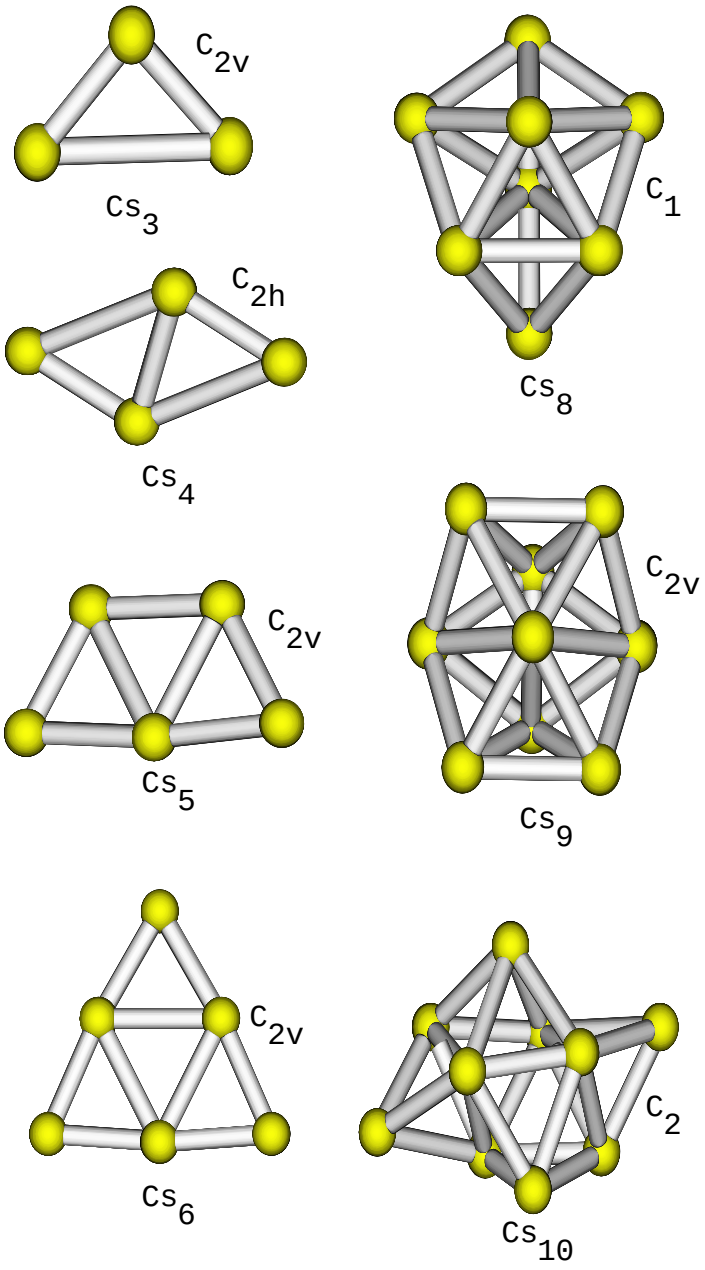

Fig. 6: Selected Structures of Cs-Cluster

Relativistic quantum chemistry with two-component spinors

Christoph van Wüllen

Institut für Chemie Sekr. C3; Technische Universität Berlin, Straße des 17. Juni 135; 10623 Berlin; Germany

Traditional quantum chemistry is a quest for accurate approximations to the exact solution of the Schrödinger equation. However, the classical limit of the Schrödinger equation is Newtons mechanics which is not Lorentz covariant. As in the case of non-relativistic classical physics, this is not particular disturbing as long as the speed of light is very much larger than any motion in the system. In the strong potential of heavy nuclei however, electrons "move" so fast that the non-relativistic Schrödinger equation does not correctly describe the electronic structure. This not only applies to the core electrons, but likewise holds for valence electrons and chemical phenomena. Conventionally, one assumes that nonrelativistic calculations can accurately describe reality if there are no atoms beyond krypton (Z=36) in the molecule. Although it is somewhat arbitrary where to draw the border, it is utterly clear that for compounds containing superheavy elements with Z>100, calculations based on nonrelativistic wave equations are essentially meaningless.

The relativistic treatment of an electron leads to the four-component

Dirac equation. Compared to the nonrelativistic Schrödinger equations, two additional degrees of freedom appear here, namely the electron spin and charge conjugation. While the electron spin can be incorporated in an ad hoc manner in a nonrelativistic theory, charge conjugation is inherently relativistic. As a consequence, the spectrum of the Dirac equation contains a positive-energy and a negative-energy branch. In a quantum field theoretical picture, the existence of negative-energy eigenstates is connected with the existence of antiparticles (the positron in this case). From this it follows that a truly relativistic theory cannot be confined to a fixed number of particles (electron-positron pair creation and annihilation has also to be taken into account). In applications relevant to chemistry on the other hand, the energy scale does not allow for such processes . In this case, one deals with a fixed number of electrons, and then the negative-energy part of the Dirac spectrum is quite uninteresting and a nuisance for mathematical reasons. What one looks for is therefore an equivalent theory "for electrons only", usually called a "quasirelativistic" theory. One should point out that Quasirelativistic two-component methods can in principle exactly reproduce the positiveenergy branch of the spectrum from calculations using Dirac (four-component) spinors. As an aside, we mention that one can even go one step further and arrive at a one-component (or scalar-relativistic) computational scheme. In this step however, one neglects spin-orbit coupling which is of utmost importance for example for the chemistry of superheavy p-block elements (element 113 through 118). Such scalar-relativistic methods are therefore not discussed in our contribution.

Historically, two-component Hamiltonians have initially been sought since the absence of negative-energy eigenstates eliminates some problems associated with a four-component treatment, such as variational collapse (the Dirac

spectrum is unbound and thus this operator is not amenable to a variational treatment) and the Brown-Ravenhall disease (a naive way of performing configuration interaction calculations with the full set of Dirac orbitals will induce heavy mixinig-in of continuum functions). Today however, these problems are essentially solved by the kinetic balance prescription to construct four-component basis sets and by the no-pair approach to correlated Dirac-Coulomb calculations. Quasirelativistic two-component Hamiltonians still arise interest as long as their lower complexity can be exploited to yield computational procedures which involve considerably less compuational effeort than four-component calculations based on the Dirac equation. Our analysis shows that such computational savings are to be expected for methods like Hartree-Fock, DFT and MP2, while high-level correlation calculations will behave very similar in a two-component and four-component framework because of the no-pair approximation that is necessary in the latter. It should be pointed out that a very interesting perspective for two-component quasirelativistic methods is the use of spin-dependent ("two-component") effective core potentials. Such calculations are very economic and can be applied to a large body of chemical problems.

Bearing in mind these considerations, we have programmed a two-component Hartree-Fock and density functional program including energy gradients. In a two-component program, each "conventional" basis function occurs explicitly twice (for both spin orientations), and therefore, if taken literally, the matrix represenation of e. g. the one-particle Hamiltonian would be a 2N*2N complex matrix (N is the number of basis functions used in the calculation). A better interface to existing nonrelativistic computer code, and reduced storage and CPU requirements can be achieved if a quaternion-like algebraic structure is used throughout the program, such that one always

deals with spin-free operators that can be represented by a hermitian N·N matrix that furthermore in many cases is either real or imaginary. Test calculations on heavy and superheavy element compounds involving the elelemts Tl, Pb, Bi and their superheavy homologues element 113, 114, and 115 show that results from four-component calculations can be duplicated with our quasirelativistic code for properties like bond lengths, ionization potentials, binding energies and vibrational frequencies. The basis sets have to be chosen properly, however. It is very important to have steep p-functions, and use a "j-adapted" contraction scheme.

The ZORA Hamiltonian has been used in these calculations, but recently we also have implemented Douglas-Kroll up to sixth order and molecular integrals over two-component effective core potentials, and all results agree pretty well. In this talk, we shall not discuss details of higher-order Douglas-Kroll theory, but it is important to note that quasirelativistic two-component Hamiltonians for one-electron systems can be constructed to any desired accuracy. Up to now we only have implemented geometry gradients for ZORA, so this quasirelativistic method is currently the only one we can use to determine molecular structures of polyatomic compounds involving superheavy elements.

The problem of finding accurate two-component Hamiltonians has essentially been solved for one-electron systems, where the so-called "infinite order" or "higher order" Douglas-Kroll methods are capable of reproducing the Dirac eigenvalues to any desired accuracy. The corresponding two-component orbitals on the other hand have no direct physical meaning, a phenomenon usually referred to as "picture change". For one-electron properties (expectation values etc.) one knows how to treat picture change. If one does the algebra properly, no problems arise. As an example, we discuss

the calculation of parity-violating potentials. Because this involves the expectation value of an "odd" operator which is furthermore strongly peaked at the nuclei, there is no possibility to calculate such an expectation value in a two-component framework in the "naive" way. Instead, one expresses the expectation value in the four-component framework! as an energy derivative, performs the reduction to a two-component method, and re-expresses the resulting energy derivative again as an expectation value of some operator which is then identified as the transformed two-component parity violation operator to be used. Results from ZORA calculations agree well with those from four-component methods.

For the electron interaction, the correct treatment of the picture change quickly increases the computational effort such that the advantage over four-component calculations may be lost. We present an approximate "model potential" method for treating twoelectron picture change effects which has the correct balance between one- and two-electron terms in the long range and also is able to reproduce atomic spin-orbit splittings. The first requirement is important because otherwise, interaction energies between relativistic subsystems cannot be calculated. However, this requirement is violated by nearly all existing approximations such as the mean-field Hamiltonian. The second requirement arises quite naturally since spin-orbit splittings are quite "atom-like" in nature. We will discuss the derivation of the model potential approximation in some detail, and will demonstrate that it is able to reproduce orbital energies from four-component calculations for atomic, ionic, and molecular systems.

Conclusions:

Although they have been declared dead at several occasions, quasirelativistic two-component methods do well and are able to make four-component treat-

ments obsolete for a growing number of applications, including the calculation of chemical properties of compounds containing transactinide atoms.

Relativistic Pseudopotentials

Hermann Stoll

Institut für Theoretische Chemie, Universität Stuttgart, D-70550 Stuttgart, Germany

An accurate description of relativistic effects is of the utmost importance for a reliable theoretical treatment of compounds of the heavy and superheavy elements. A four-component approach based on the Dirac-Coulomb or Dirac-Coulomb-Breit Hamiltonian certainly meets this purpose, but the computational effort is very high. Two-component (or one-component scalar-relativistic) schemes of the Douglas-Kroll-Hess or regular-Hamiltonian type lead to substantial computational savings, but still face the necessity to explicitly treat a very large number of electrons in inner shells. This is avoided in pseudopotential theory where inner-shell electrons, which are largely unchanged when molecules are formed from atoms, are replaced by atomically parametrized model potentials (MP) or effective-core potentials (ECP). Since relativistic effects mainly arise in the core region, they can implicitly be incorporated into the same potentials, so that a formally non-relativistic treatment (with a Schrödinger-type Hamiltonian) becomes possible for heavy-element compounds.

Originally, pseudopotentials (PP) were defined as one-center/one-electron operators which simulate the above effects (i.e., frozen-corevalence interaction and relativistic effects) by means of local potentials. It soon turned out,

however, that a much better performance can be achieved with a semi-local (i.e., l- or lj-dependent) or non-local form (including, e.g., projection operators onto core orbitals). Especially the non-local form is gaining increasing popularity nowadays due to the computational ease with which quantities like, e.g., PP gradients can be evaluated.

By several groups pseudopotentials have been adjusted which retain the original nodal structure of valence orbitals from all-electron calculations (these are then also called MPs), but very often a transformation to radially nodeless pseudo-valence orbitals is implied when using PPs (also termed ECPs in this case); since the valence interaction energy changes with the pseudo-valence transformation, the pseudopotentials then also have to include correction terms which compensate for this change.

Originally, PPs were adjusted in a Hartree-Fock framework, to orbital properties of a single atomic state, but with the upcoming importance of DFT methods also density-functional-based PPs are widely used, and also information about several low-lying states is sometimes taken into account for generating the PPs.

When working with plane-wave basis sets (in solid-state calculations, e.g.), it is essential that the potentials be as smooth as possible; hence, specially designed pseudo-orbital transformations have been developed leading to (ultra-)soft PPs satisfying these requirements.

While early pseudopotentials were generated for (and used in) one-component (i.e., non-relativistic or scalar-relativistic) calculations, modern PPs incorporate spin-orbit (SO) terms as well, thus simulating relativistic effects in full.

Finally, it is increasingly recognized nowadays that, for heavy atoms, cores may become thus polarizable that they cannot be longer treated as strictly frozen; core-valence correlation effects, in particular, can be of the same order

of magnitude as relativistic effects. Adding core-polarization terms to the PPs efficiently remedies these shortcomings of the original pseudopotential theory however, the pseudopotentials are no longer one-electron operators then, and also the one-center approximation no longer strictly applies.

The present talk gives a short overview of the most important available variants of pseudopotentials, describes their merits and shortcomings, and indicates future lines of development.

Special emphasis is given to the energy-consistent pseudopotentials of the Auckland, Cologne, and Stuttgart groups. These pseudopotentials are generated using the valence-energy spectrum of a multitude of atomic states (rather than orbital properties of a single state) and can be adjusted, in principle, at every useful theoretical level. (Currently, multi-configuration Dirac-Hartree-Fock (MCDHF) is used for setting up the atomic all-electron reference spectrum.) Thus, these potentials should be particularly useful in cases, when there are low-lying excited atomic states (as in open-shell d and f elements), or when the atomic coupling is intermediate between the LS coupling of the light elements and the jj coupling of the very heavy ones. (Both limits can be covered with a state-averaged MCDHF containing all relativistic states of a non-relativistic orbital configuration.)

We discuss recent progress for improving the accuracy and transferability of the energy-consistent PPs [1, 2], on the development of correlation-consistent series of valence basis sets for these potentials (in co-operation with K.A. Peterson (WSU and PNNL) [3, 4], and on on-going benchmark calculations [5, 6, 7].

References

[1] H. Stoll, B. Metz, M. Dolg, J. Comput. Chem. 23 (2002) 767.

[2] M. Dolg, D. Figgen, H. Stoll, in preparation

[3] K.A. Peterson, D. Figgen, E. Goll, H. Stoll, M. Dolg, J. Chem. Phys. 119 (2003) 11113

[4] K.A. Peterson, M. Dolg, H. Stoll, in preparation

[5] I.S. Lim, P. Schwerdtfeger, B. Metz, H. Stoll, J. Chem. Phys. 122 (2005) 104103.

[6] D. Figgen, G. Rauhut, M. Dolg, H. Stoll, Chem. Phys. 311 (2005) 227.

[7] I.S. Lim, P. Schwerdtfeger, T. Söhnel, H. Stoll, J. Chem. Phys. 122 (2005) 134307.

Non-collinear and collinear four-component relativistic density functional theory

J. Anton and B. Fricke

Institut für Physik, Universität Kassel, D-34109 Kassel, Germany

An attractive way to describe electronic matter is through density functional theory (DFT). This method is as old as wave-function based approximations for solving the electronic Schrödinger- or Dirac-equation, and originally comes from the simple Thomas-Fermi model [1, 2], which in early times was the only practical method to describe total electronic energies and densities within atoms. However, with the ever increasing computer power and the development of more sophisticated algorithms, the many-particle Dirac equation can now be treated with relatively high accuracy for small electronic systems.

For atoms the Dirac-Fock-Slater [3], Dirac-Fock and Multiconfiguration Dirac-Fock [4, 5] approximations are in use for more than two decades now, and very precise ab-initio calculations are now possible for many-electron systems in heavy atoms [6]. Somewhat later the same development began for the solution of molecular systems, but at that time most quantum chemical methods were restricted to the non-relativistic framework, and initially relativistic effects were included through the Pauli-Hamiltonian via perturbation

theory (if at all). Because of the importance of spin-orbit coupling for heavy element containing molecules, a lot of effort was invested in approximate 2-component methods which often lead to excellent results even for states with very large spin-orbit splittings (some reviews are given in [7, 8, 9, 10]). Nevertheless, such methods have to be considered as approximations to the full four-component Dirac description.

The density functional method has a sound basis in form of the Hohenberg-Kohn Theorem in 1964 [11] which proved that all electronic matter can be described exactly by a 3-dimensional density only.

In 1973 this theorem was extended by Rajagopal and Callaway to the relativistic domain [12]. In this case the total energy is a functional of the four-current J_μ. The problem to find the exact four-current in the relativistic framework analogous to the density in the non-relativistic case is not yet solved. Nevertheless, a number of density functionals have already been proposed [13, 14, 15, 16] and a lot of effort still goes into finding the "exact" density functional (see for example Ref. [17, 18]). Four-component density functional theory for molecules within the non-collinear approach have already been reported.

We briefly discuss Gordon's decomposition [19] to approximate the four-current of the exact relativistic formulation in the form of a charge and magnetization density in order to perform actual calculations within the non-collinear formalism for molecules. A general derivation of this method can be found in Ref. [17] and [20]. Within this approximation the total energy of a molecular system is given by the following expression

$$E = \sum_{i=1}^{M} n_i \left\langle \psi_i \,\middle|\, \hat{t} \,\middle|\, \psi_i \right\rangle + \int V^N \rho \; d^3\,\vec{r} + \frac{1}{2} \int V^H \rho \; d^3\,\vec{r} + E^{xc}[\rho, \vec{m}] + \sum_{p>q} \frac{Z_p \, Z_q}{|\vec{R}_p - \vec{R}_q|} \quad (2)$$

with the density ρ and magnetization density $\vec{m}$ which are defined by

$$\rho(\vec{r}) = \sum_{i=1}^{M} n_i \, \psi_i^+(\vec{r})\psi_i(\vec{r}) \tag{3}$$

$$\vec{m}(\vec{r}) = -\mu_B \sum_{i=1}^{M} n_i \psi_i^+(\vec{r})\beta\vec{\Sigma}\psi_i(\vec{r}) \, . \tag{4}$$

Here n_i are the occupation numbers, $\vec{r}$, $\vec{R}_q$ are the electronic and nuclear coordinates respectively and μ_B is the Bohr-magneton. The index i runs over all occupied molecular orbitals M, which in our case are four-component Dirac-spinors. The four-component spin-operator $\vec{\Sigma} = (\Sigma_x, \Sigma_y, \Sigma_z)$ is built from the two component Pauli matrices $\vec{\sigma}$. The Dirac kinetic energy operator has the form (we use atomic units throughout)

$$\hat{t} = c \, \vec{\alpha} \cdot \hat{\vec{p}} + c^2(\beta - I) \, , \tag{5}$$

where $\vec{\alpha} = (\alpha_x, \alpha_y, \alpha_z)$ and β are the four-component Dirac matrices in the standard representation [21], and I is the four-component unit matrix. V^N is the nuclear potential

$$V^N = \sum_p -\frac{Z_p}{|\vec{r} - \vec{R}_p|} \, , \tag{6}$$

where the index p runs over all nuclei in the molecular system.

E^{xc} is the exchange-correlation energy functional.

V^H is the electronic Hartree potential

$$V^H(\vec{r}) = \int \frac{\rho(\vec{r}\,')}{|\vec{r} - \vec{r}\,'|} \, d^3\,\vec{r}\,' \, . \tag{7}$$

Since the calculation of the Hartree potential from the SCF-density (3) is very time-consuming, we approximate ρ in (3) by a model-density $\tilde{\rho}$. We expand our model-density into series of 'atomic' multipole-densities centered on the nuclei.

The variation of the energy functional (2) leads to the relativistic Kohn-Sham (KS) equations in their general form for the molecular Kohn-Sham orbitals ψ_i

$$\left\{\hat{t} + V^N + \tilde{V}^H + \frac{\delta E^{xc}[\rho,\vec{m}]}{\delta\rho} - \mu_B\beta\vec{\Sigma}\cdot\frac{\delta E^{xc}[\rho,\vec{m}]}{\delta\vec{m}}\right\}\psi_i = \epsilon_i\psi_i \qquad i = 1,...,M' \quad (8)$$

Here $\tilde{V}^H$ is the Hartree potential from the model-density and $M' \geq M$ is the number of molecular orbitals.

This general formulation is called a non-collinear description which allows the magnetization density to point in any direction at any point of the system under consideration. Because often the z-component of the magnetization density is physically important, an approximation of this expression is used which is called the collinear description. For details we refer here to Ref. [22].

The Kohn-Sham equations in the collinear form read

$$\left\{\hat{t} + V^N(\vec{r}) + \tilde{V}^H(\vec{r}) + \frac{1+\beta\Sigma_z}{2}V_+^{xc}(\vec{r}) + \frac{1-\beta\Sigma_z}{2}V_-^{xc}(\vec{r})\right\}\psi_i(\vec{r}) = \epsilon_i\psi_i(\vec{r}) \quad (9)$$

with

$$V_\pm^{xc}(\vec{r}) = \frac{\delta E^{xc}[\rho_+,\rho_-]}{\delta\rho_\pm} = \frac{\delta E^{xc}[\rho,m_z]}{\delta\rho} \mp \mu_B\frac{\delta E^{xc}[\rho,m_z]}{\delta m_z}\,.$$

At this point we would like to make a few general but important comments: Although physically incorrect people often speak of 'spin up' and 'spin down' components in this collinear description. Of course the 'spin' has a strong contribution to the magnetization density. But one has to have to remember two important facts. First, orbital angular momenta also contribute to the magnetization density and second, spin as well as orbital angular momenta have no good quantum numbers anymore in relativistic theory and therefore, one should speak of magnetization densities only. The total angular momentum J and the angular momenta j of each electron are the only good quantum numbers in atoms.

In addition we would like to comment on the Kohn-Sham orbitals. They contribute to the charge- resp. the magnetization-density according to formulae (3) and (4). Because these densities are in principle exact, the Kohn-Sham orbitals can not be compared to Hartree-Fock wavefunctions which usually are written in Slater-Determinants. Rather the density built from Kohn-Sham orbitals must be compared with a density built from an infinite sum of Slater determinants in the Hartree-Fock sense.

Due to the fact that the practical solution of the Kohn-Sham equations in form of eq.(8) is hard to achieve (independent of the special functional used), only very few results have been reported so far [23]. We recently have developed a method to perform this kind of calculations [24, 22] which allows the magnetic moment to point in any direction at any point in space. A similar implementation of non-collinear DFT can be found in [25]. In this non-collinear approximation nearly each electron is treated by its own wavefunction with a quantum number j and magnetic quantum number m_j in the atomic decomposition of the molecular wave function.

Due to the fact that not only the electric but also the magnetic density is included in the self-consistent interaction, each electron often converges to a non-degenerate energy eigenvalue and thus depends on the occupation of the Kohn-Sham orbitals with different total energies. We should mention here that all results which we present in the following are performed within the Becke 88 [15] for the exchange and Perdew 86 [14] for the correlation functionals. In addition, we compare all these results with the Perdew Wang 91 [16] functionals, which often lead to very similar values compared to the other functionals.

Molecular dissociation energies depend on the total energy of the molecule as well as the total energy of the separated fragments or atoms. To be phys-

ically correct, all values of the potential energy curve, including the infinite distance values, have to be calculated with the same density functional method. In the non-relativistic description one gets the average of the multiplet, and in the relativistic description the average of the sub-multiplet. Thus up to now the atomic values had often to be corrected afterwards. In most cases the non-collinear description reaches the atomic ground state automatically, which means that one does not need to correct the potential energy curve at larger distances.

An example for first excited atomic levels of platinum is presented in [26]. As is it showed there the non-collinear DFT values can reasonably good reproduce those levels and compare even better with experiment than the Dirac-Fock values. Of course, deviations are due to the approximations made in the density functional.

The ground state of an atom is usually described by the angular momentum L as well as by the total spin S as the projection of the total angular momentum M_j and will be usually written in the form ${}^{2S+1}L_{M_j}$. This notation is widely used in the spectroscopy [27] and is correct within the non relativistic quantum mechanics where all these observable are 'good' quantum numbers when the spin-orbit coupling is neglected. For heavy elements however relativistic effects become more and more important and lead to a break down of the non-relativistic picture. One of famous examples for this is bismuth. According to the semiempirical Hund's rule the total spin of all homologues of bismuth should be 3/2. As it was shown in the early 70's [28] there is a strong deviation from this value for Bi-atom. In the table 1 we present the total magnetic moments of all known homologues of bismuth in the ground state which are proportional within the non-collinear density functional theory to the total spin of the atoms.

Element	Z	Fine splitting (eV)	Magnetic moment
N	7	0.019	2.99987
P	15	0.054	2.99951
As	33	0.277	2.99169
Sb	51	0.613	2.93940
Bi	83	1.857	1.71797
E115	115	4.755	1.23677

Tab. 1: Fine splittings of the outermost p-shell and the total magnetic moments of homologue of bismuth.

One can see from this table a dramatic change of the magnetic moment for bismuth and E115. On the other hand within the relativistic description bismuth is an effective one electron system and one would expect a magnetic moment equal to one. From this point of view one could say that 6p-shell bismuth behaves neither full relativistically nor non-relativistically. In contrast to this the 7p-shell of the element E115 has a very pronounced relativistic character.

For applications of the presented method to small molecules and clusters we refer to our recent publications [24, 29, 22, 30, 26]. There we presented the 'standard' molecular properties such as bond energies and bond length as well as magnetic properties of molecules. In all considered case we achieved a good agreement with experimental data if such data were available.

J. A. gratefully acknowledges the financial support from the Deutsche Forschungsgemeinschaft (DFG).

References

[1] R. H. Thomas, Proc. Camb. Phil. Soc. **23**, 542 (1927)

[2] E. Fermi, Z. Phys. **48**, 73 (1928)

[3] D. A. Lieberman, D. T. Cromer, and J. T. Waber, Comp. Phys. Com. **2**, 107 (1970)

[4] J. P. Desclaux, Comp. Phys. Com. **9**, 31 (1975)

[5] I. P. Grant, B. J. Mc Kensie, P. H. Normington, D. F. Myers, and N. C. Paper, Comp. Phys. Comm. **21**, 2007 (1980) K. G. Dyall, I. P. Grant, C. T. Johnson, F. A. Parpia, and E. P. Plummer, Comp. Phys. Comm. **55**, 425 (1989)

[6] U. Kaldor, E. Eliav, and A. Landau, *Theoretical Chemistry and Physics of Heavy and Superheavy Elements.*, edited by U. Kaldor and S. Wilson, Kluwer Academic, Dordrecht, 2003; pg.171 John Wiley & Sons, 2001

[7] R. L. Matcha, J. Am. Chem. Soc. **95**, 7506 (1973)

[8] Y. S. Lee, W. C. Ermler, and K. S. Pitzer, J. Chem. Phys. **67**, 6851 (1977)

[9] B. A. Hess, C. M. Marian, and S. D. Peyerimhoff, *Modern Electronic Structure Theory*, edited by D. R. Yarkony, World Scientific, 1995; pg. 152.

[10] P. Pyykkö, Lecture Notes in Chemistry, Vol. 41, Springer, Berlin, 1986.

[11] P. Hohenberg and W. Kohn, Phys. Rev. **136**, 864 (1964)

[12] A. K. Rajagopal, J. Callaway, Phys. Rev. B**7**, 1912 (1973)

[13] S. H. Vosko, L. Wilk, M. Nusair, Can. J. Phys. **58**, 1200 (1980)

[14] J. P. Perdew, Phys. Rev. B**33**, 8822 (1986)

[15] A. D. Becke, Phys. Rev. A**38**, 3098 (1988)

[16] J. P. Perdew, in *Electronic Structure of Solids*, ed. by P. Ziesche and H. Eschrig, p.11, Akademie Verlag, Berlin 1991

[17] E. Engel, R. M. Dreizler, S. Varga, and B. Fricke, *Relativistic Effects in Heavy-Element Chemistry and Physics.*, edited by B. A. Hess, John Wiley & Sons, 2001

[18] E. Engel, and R. M. Dreizler, Top. Curr. Chem. **181**, 1 (1996)

[19] H. Eschrig and V. D. P. Servedio, J. Comput. Chem. **20**, 23 (1999)

[20] E. Engel, *Relativistic Electronic Structure Theory, Part 1: Fundamentals*, edited by P. Schwerdtfeger, Elsevier, Amsterdam, 2002

[21] L. D. Landau, E. M. Lifschitz, *Quantenelektrodynamik*, Akademie-Verlag, Berlin 1986

[22] J. Anton, B. Fricke, E. Engel, Phys. Rev. **A 69**, 012505 (2004)

[23] M. Mayer, S. Krüger, and N. Rösch, J. Chem. Phys. **115** 4411 (2001)

[24] J. Anton, T. Jacob, B. Fricke and E. Engel, Phys. Rev. Lett. **89**, 213001 (2002)

[25] F. Wang and W. J. Liu, J. Chin. Chem. Soc. **50** (3B), 597 (2003)

[26] J. Anton, B. Fricke, and P. Schwerdtfeger, Chem. Phys. **311**, 97 (2005)

[27] C. E. Moore, *Ionization Potentials and Ionization Limits derived from the Analyses of Optical Spectra*; NSRDS-NBS24, NBS, Washington DC 1970

[28] I. Lindgren and A. Rosĕn, *Case Studies in Atomic Physics*, Vol. 4, North-Holland 1974

[29] J. Anton, M. Hirata, B. Fricke, and V. Pershina, Chem. Phys. Lett. **380**, 95–98 (2003)

[30] J. Anton, T. Ishii, and B. Fricke, Chem. Phys. Lett. **388**, 248–252 (2004)

Adsorption of super-heavy elements on metal surfaces

C. Sarpe-Tudoran[1], *V. Pershina*[2], *B. Fricke*[1],*J. Anton*[1]

[1]Universität Kassel, D-34109 Kassel,

[2]Gesellschaft für Schwerionenforschung, D-64291 Darmstadt

1 Introduction

The fully relativistic, 4-component Density Functional Theory (DFT) method with the General Gradient Approximation (GGA) for the exchange-correlation potential has been successfully applied to molecules and clusters of different sizes in recent years. In this work the theoretical study of the adsorption of element 112 and its homologue, Hg, was done using the embedded-cluster method which will be described below. This method is based on the fact that chemisorption is both a geometrically and energetically local phenomenon. It means that for a certain adsorption site, the adsorbate mainly interacts with the metal-surface atoms lying close to the adsorption place, and the character of the binding depends on the geometry of the system (more precise, on the position of the ad-atom relative to the crystal lattice points: top-, bridge- or hollow-position). The cluster which models the surface is then embedded in a much bigger environmental cluster. This procedure allows to achieve results which converge with the size of the cluster.

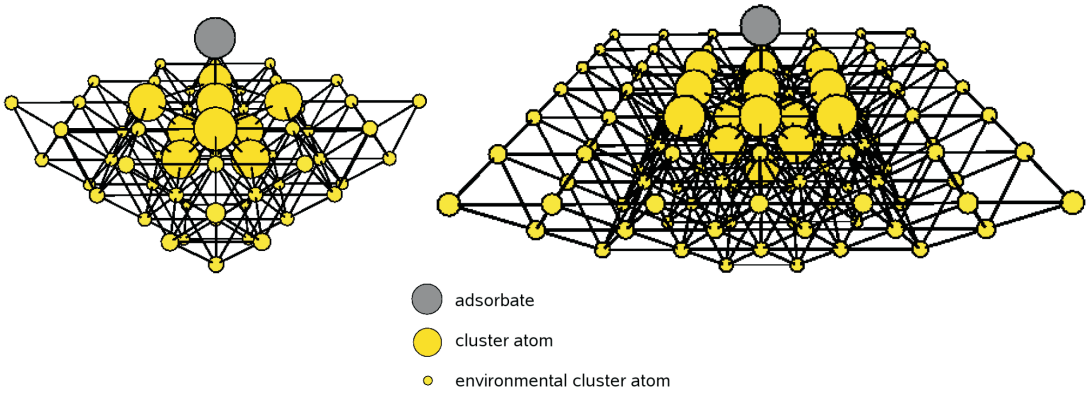

Fig. 1: Embedded cluster models for the case in which only the first coordination shell (left hand side) and respectively up to second coordination shell (right hand side) are considered.

2 Method

2.1 General considerations

For properly describing the chemisorption, the cluster has to fulfil several conditions.

Firstly, if one wishes to model a particular surface, the geometry of the surface atoms interacting with the adsorbate and that of the cluster have to be the same to at least the first coordination shell. For instance, at a (100) surface of a faced centred cubic metal, surface atoms have eight metal-atom neighbours. Four of them are in the plane and the other four are located in the second layer. Clusters which model chemisorption atop such a surface atom in a (100)fcc metal should include at least these eight metal-atom neighbours (see Fig. 1).

The next coordination shell contains 4 atoms in the first layer and one atom in the third plane, resulting in a cluster with 14 atoms: $Au_{14}(9, 4, 1)$ which also is shown in Fig. 1 Due to the requirement of conserving the sym-

metry of the metal surface, the size of the cluster cannot be varied monotonically. For instance, for the atop adsorption mentioned above the first few model clusters should have 9, 14, 26, 34, 40, ... atoms.

Secondly, even when the first coordination shell of the metal-surface atom is fully included in the inner cluster, another difficulty arises. In the embedded cluster technique it is assumed that the perturbation of the environment due to the presence of the ad-atom is small and therefore is neglected. However, if the cluster contains too few atoms, this assumption may not be true anymore. This reversal from the real surface situation leads to electron-distribution differences significantly deviating from that of a true surface atom.

Thirdly, the number of atoms in the cluster should be enough that a continuous valence band is formed.

2.2 Equations

In the RDFT the total energy of a system with N nuclei and M electrons is given by (10):

$$E = \sum_{i=1}^{M} n_i \left\langle \psi_i \mid \hat{t} \mid \psi_i \right\rangle + \int V^N \rho \, d^3\,\vec{r} + \frac{1}{2} \int V^H \rho \, d^3\,\vec{r} + E^{xc}[\rho] + \frac{1}{2} \sum_{K=1}^{N} \sum_{K' \neq K}^{N} \frac{Z_{K'}\, Z_K}{|\vec{R}_{K'} - \vec{R}_K|} \,. \tag{10}$$

In the non-pair approximation the electronic density is constructed as follows:

$$\rho(\vec{r}) = \sum_{i=1}^{M} n_i \, \psi_i^+(\vec{r}) \psi_i(\vec{r}), \tag{11}$$

where n_i is the occupation of the molecular orbital ψ_i.

The variation of the total energy leads to the Kohn-Sham equation:

$$\left(\hat{t} + \hat{V}^N + \hat{V}^H + \hat{V}^{xc} \right) \psi_i(\vec{r}) = \epsilon_i \psi_i(\vec{r}) \tag{12}$$

which has to be solved self-consistently.

To solve the Kohn-Sham equations (12) we use the MO-LCAO (Molecular Orbital – Linear Combination of Atomic Orbitals) method. Within this method we expand the molecular orbitals $\psi_i(\vec{r})$ in a series of symmetry-adapted orbitals (SO) $\chi_j(\vec{r})$

$$\psi_i(\vec{r}) = \sum_j c_{ji}\chi_j(\vec{r})\,. \tag{13}$$

The SO's themselves are expanded in a series of atomic orbitals φ_ν

$$\chi_j(\vec{r}) = \sum_\nu d_{\nu j}\varphi_\nu(\vec{r}) \tag{14}$$

where the expansion coefficients $d_{\nu j}$ can be determined from Group theory [1]. Atomic orbitals are solutions of the atomic Kohn-Sham equation.

Inserting 13 in the equation 12 gives the matrix equation in the symmetry orbital representation

$$\underline{\underline{H}}\,\underline{\underline{c}} \;=\; \underline{\underline{S}}\,\underline{\underline{c}}\,\underline{\underline{\varepsilon}} \tag{15}$$

where $\underline{\underline{H}}$ and $\underline{\underline{S}}$ are the Fock and overlap matrices respectively, $\underline{\underline{c}}$ is the coefficient-matrix, and $\underline{\underline{\varepsilon}}$ is the eigenvalue diagonal matrix.

In the embedded cluster method the system is divided in two parts, an inner cluster an an environmental cluster. The inner cluster contains N^{Cl} nuclei and M^{Cl} electrons the rest of the nuclei $N^{Env} = N - N^{Cl}$ and $M^{Env} = M - M^{Cl}$ electrons belong to the environment. In our calculation we use an auxiliary density, $\tilde{\rho}(\vec{r})$ which fits the "true" density $\rho(\vec{r})$. Thus

$$\rho(\vec{r}) \;=\; \tilde{\rho}(\vec{r}) + \Delta\rho(\vec{r}), \tag{16}$$

where the modelled density $\tilde{\rho}(\vec{r})$ is obtained by a multipolar expansion [2] over spherical harmonics $Y_l^m(\theta_k, \phi_k)$ and radial functions $F_k^j(r_k)$ centred on the atoms of the system.

This procedure leads to a considerable simplification in calculating the Hartree potential and allow us to divide the total density in two parts:

$$\rho \equiv \sum_{i=1}^{M} n_i \, \tilde{\psi}_i^{+}(\vec{r})\tilde{\psi}_i(\vec{r}) = \sum_{i=1}^{M^{Cl}} n_i^{Cl} \, \psi_i^{Cl^{+}}(\vec{r})\psi_i^{Cl}(\vec{r}) + \sum_{i=M^{Cl}+1}^{M} n_i \, \psi_i^{Cl^{+}}(\vec{r})\psi_i^{Cl}(\vec{r}) \equiv$$
$$\equiv \rho^{Cl} + \rho^{Env} \tag{17}$$

The Hartree energy is linear in the density and can be divided in two parts:

$$V^C \equiv V^C(\rho) = V^C(\rho^{Cl}) + V^C(\rho^{Env}) \equiv V_{Cl}^C + V_{Env}^C \, . \tag{18}$$

This procedure leads to the Kohn-Sham equation in the cluster embedding method

$$\left(\hat{t} + \hat{V}_{Cl}^N + \hat{V}_{Cl}^C + \hat{V}^{xc}(\rho) + \hat{V}^{Ext}\right) \psi_i^{Cl}(\vec{r}) = \epsilon_i^{Cl}\psi_i^{Cl}(\vec{r}). \tag{19}$$

where $\hat{V}^{Ext} = \hat{V}_{Env}^N + \hat{V}_{Env}^C$ is the external potential. This equation contains one additional term V^{Ext} in comparison to a similar equation in the cluster method (12). A further difference is the exchange-correlation potential which depends not only on the density in the cluster but from the total density. These two terms contain the whole information about the environment.

The occupation of the environmental cluster atoms AO's is kept fixed during the self-consistent calculations.

3 Results

In the present calculations, inner gold clusters of 14, 16, 22 and 29 atoms were used which were embedded in the outer environment of 112, 110, 92 and 156 atoms to simulate the Au(100) surface. Hg and element 112 were considered in the on-top, bridge and hollow adsorption positions with respect to the surface cluster atoms.

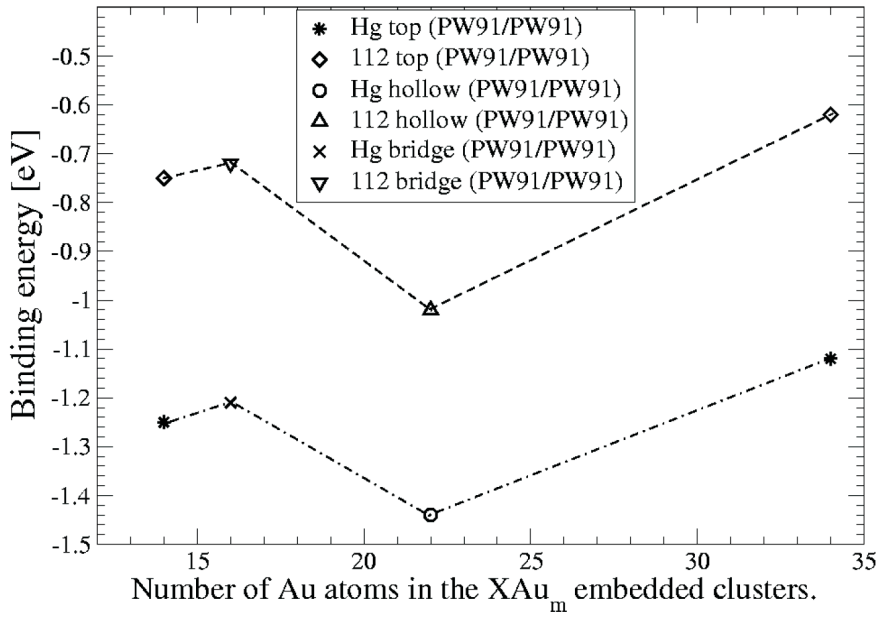

Fig. 2: The GGA (PW91/PW91) binding energies as a function of the number of atoms used to model the surface(embedding method).

The calculations were performed with two types of basis sets: the basis set of type B includes the filled neutral 1s through ns orbitals and slightly charged virtual np and $(n-1)$f orbitals, while a more extended basis set of type B' includes the charged virtual nd, $(n-2)$g and nf orbitals in addition to those of the basis set B. The calculated binding (adsorption) energies E_b for the basis set B as a function of the number of atoms in the inner gold cluster and the adsorption position are shown in Fig. 2.

The behaviour of the binding energies for Hg and element 112 as function of the number of atoms in the cluster are very similar. However, the differences in the binding energy were (≈ 0.4 eV) much larger than one expects from the diatomic calculations [5] of HgAu and E112Au molecules, where HgAu was more strongly bound by about 0.1 eV. This result suggested that the AO's basis which we used in the MO-LCAO expansion was too poor.

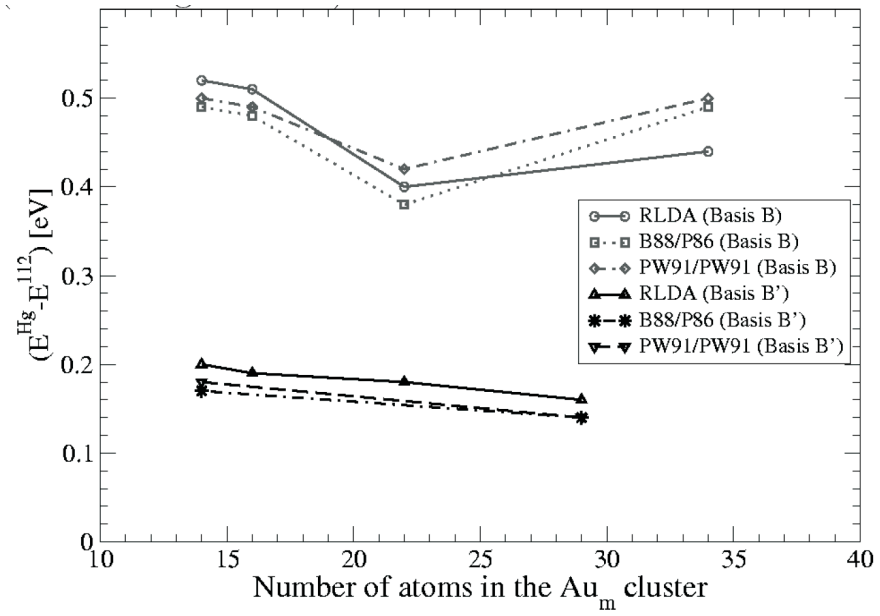

Fig. 3: The differences ($\Delta E_b = E_b^{Hg} - E_b^{112}$) in the binding energies for the top, bridge and hollow positions, embedding method.

Therefore we decided to increase the number of AO's in the basis for adsorbates; the more extended basis we have denoted B'.

Results of the calculations with the basis set B' are given in Table 1. The obtained data show that absolute values of E_b are dependent on the adsorption position, with the hollow one being preferential both for Hg and element 112. The E_b for the basis set B' are more negative. The differences $\Delta E_b = E_b^{Hg} - E_b^{112}$ in the binding energies as function of the number of Au cluster atoms is plotted in Fig. 3, for both basis B and B'. Two main features result from it. Firstly, for the basis B' there is a systematic behaviour of ΔE_b for both RLDA and GGA values in contrast to the corresponding values for basis B. Secondly, the difference in the binding energy slowly decreases with increasing number of Au atoms, being practically independent of the adsorption site. Niklaus et al.[7] found a value of 1.05 eV for the adsorption enthalpy of Hg on Au surface. On the basis of the data in Table 3 we predict

m	method	$HgAu_m$		$E112Au_m$	
		D_e [eV]	r [a.u.]	D_e [eV]	r [a.u.]
14 (top)	RLDA	2.16	4.82	1.96	5.10
	B88/P86	1.64	4.97	1.47	5.32
	PW91	1.75	4.94	1.57	5.31
16 (bridge)	RLDA	2.14	4.30	1.95	4.50
22 (hollow)	RLDA	2.45	3.50	2.27	3.80
29 (hollow)	RLDA	1.91	3.51	1.75	3.80
	B88/P86	0.86	4.11	0.72	4.37
	PW91	0.98	4.05	0.84	4.32

Tab. 1: Dissociation energies D_e and bond lengths r for $HgAu_m$ and $^{112}Au_m$, with m = 14, 16, 22 and 29, when the enlarged basis sets (B') are used.

for the corresponding quantity for element 112 a value of 0.9 eV.

References

[1] W. Ludwig, C. Falter, Symmetries in Physics, Springer-Verlag, Berlin, Heidelberg, New York, London, Paris, Tokyo 1988

[2] B. I. Dunlap, J. W. D. Connolly, J. R. Sabin, *J. Chem. Phys.*, **71**(8), 3396– 3402 (1979)

[3] V. Pershina et al. Chem. Phys. Lett., 365, 176 (2002).

[4] T. Jacob, J. Anton, C. Sarpe–Tudoran, W.-D. Sepp, *Surf. Sci.*, **536**, 45–54 (2003)

[5] C. Sarpe–Tudoran, V. Pershina, B. Fricke, J. Anton, W.D. Sepp, T. Jacob, *Eur. Phys. J. D*, **24**, 65–67 (2003)

[6] C. Sarpe-Tudoran, *Adsorption of element 112 on a Au surface*, Kassel University Press, 2004

[7] J.-P. Niklaus, R. Eichler, S. Soverna, H. W. Gaggeler, *PSI Annual Report*, 8 (2000)

Reactions on Pt and Pt-based surfaces

Timo Jacob

Fritz-Haber Institut der Max-Planck Gesellschaft, Faradayweg 4-6, 14195 Berlin, Germany;

California Institute of Technology, Pasadena, California 91125, USA;

e-mail: jacob@fhi-berlin.mpg.de

1 Introduction

Nowadays Platinum is used to catalyze a whole variety of different reactions. Especially for electrocatalytic processes (such as in fuel cells) expensive Pt is still one of the most sufficient materials providing a high rate for oxygen reduction at lower temperatures (80-100°C):

$$O_2 + 4H^+ + 4e^- \longrightarrow 2H_2O.$$

However, mostly this reaction occurs in a multi-component environment and under conditions of finite temperature, pressure, and electrode potential ($p = 1$ bar, $T = 80$–100°C, $\Phi \neq 0$V). Thus, the model of a pure and perfect Pt(111) surface, which is often used to study this reaction, is clearly incomplete. In order to replace Pt as catalyst material (or at least reduce its amount) and improve the reaction kinetics at the cathode several different materials such as Ni/Mo[1, 2] or Pt-based bimetallic alloys (e.g. Pt_3Ni, Pt_3Co [3, 4]) have been proposed, However, it is important to understand the reaction process

at the cathode in order to find a reaction sequence that would maintain a small barrier for each of the steps. In addition, this will show the rate-determining step of the whole reaction pathway and allow improvement of the reaction rate at the cathode by specifically lowering their energy barriers. Although under electrochemical conditions the electrodes are surrounded by several solvent molecules (e.g. water), knowing the reaction pathways and their energetics in gas-phase is indispensable to understand the overall process and the impact of each component. In this paper we provide a complete picture of the cathode reaction processes in gas-phase using Pt as catalyst material. Afterwards we apply a first order solvation model to investigate the influence of surrounding water molecules on each reaction step and the overall mechanism. In order to understand the experimentally observed enhancement of the oxygen reduction using Pt_3Ni- or Pt_3Co-alloys we studied the structure of their surfaces and nanoparticles, which afterwards were used to obtain the potential energy surfaces for adsorbing atomic hydrogen and oxygen.

2 Methods

2.1 Cluster-calculations

The calculations on finite systems were performed using spin-unrestricted density functional theory (DFT) with the B3LYP flavor of the exchangecorrelation functional. This GGA-hybrid-functional (generalized gradient approximation) [5, 6] combines exact HartreeFock exchange with the Slater local exchange functional [7]. In addition, it uses the Becke gradient correction [8], the local VoskoWilkNusair exchange functional [9], and the LeeYangParr local gradient-corrected functional [6]. All ab-initio cluster calculations were

carried out with the Jaguar program suite [10]. For platinum the 60 core electrons (1s4f) were treated by the Hay and Wadt corevalence relativistic effective-core potential (ECP), leaving 18 valence electrons [atomic ground state of Pt is $(5s)^2(5p)^6(5d)^9(6s)^1(6p)^0$] treated with the LACVP** basis set. Both other elements (H and O) are described with all electrons using the 6-31G** basis set.

2.2 Slab-calculations

For the infinitely extended surfaces we used the SeqQuest [11] periodic DFT program with Gaussian basis sets (rather than plane waves) and the PBE [12] exchangecorrelation functional. The 62 core electrons of each Pt were replaced by a norm-conserving pseudopotential, leaving the 16 5p, 5d, and 6s electrons to be treated explicitly on a "double-ζ+polarization" level. In case of Ni the treatment was accordingly, leaving the 3p, 3d, and 4s electrons in the valence space.

3 Oxygen Reduction on Pt(111)

3.1 Cluster-Model

In order to simulate the Pt-catalyst by a finite cluster, it is necessary to determine the minimum size of the model cluster that correctly describes surface reactions of organic molecules on the catalyst surface [e.g. Pt(111)]. Increasing systematically the number of cluster-atoms and examining both the electronic structure of the surface cluster and the reaction with an O atom, we were able to find a suitable cluster[13], shown in Fig. 1. We chose to examine the chemisorption of oxygen because it binds strongly to the surface, whereas the electronic structure of the Pt-clusters suffers distinct

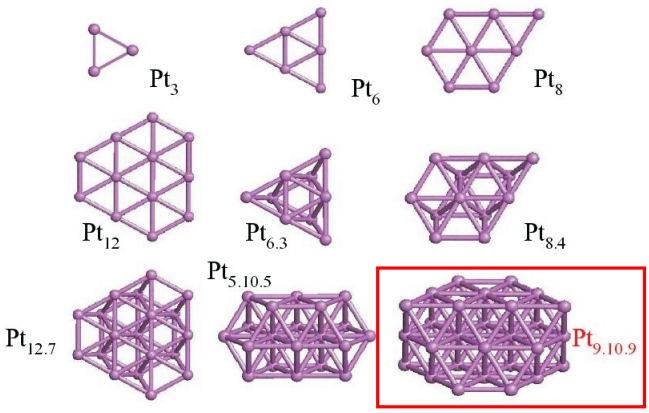

Fig. 1: Clusters studied for convergence

modifications. Therefore, a cluster that properly describes the chemisorption of oxygen is likely to be adequate for other surface processes involving less reactive species or organic fragments. For each system the oxygen atom was located at different adsorption sites (fcc $-\eta_3$, hcp $-\eta_3$, bridge $-\eta_2$, top $-\eta_1$) and after a fully self-consistent geometry optimization the values for the bond properties were compared. In fact, the three-layer system $Pt_{9.10.9}$ (28 atoms) is well enough for describing adsorption processes on the Pt(111) surface. The adsorption energies, bond distances, and vibrational frequencies predicted for the different sites are summarized in Table 1.

	Top	Bridge	Hcp	Fcc	exp.	slab
E [eV]	2.015	2.729	2.946	3.284	$3.21 - 3.43$	3.43
R_{Pt-O}	1.872	1.990	2.040	2.005	2.01 ± 0.05	2.02
$\omega[cm^{-1}]$			531	510	$466 - 480$	470

Tab. 1: Summary of the bond properties

The comparison of the experimental results with our calculated values shows good agreement for the bond distance and vibrational frequency. The calculated energies are within range of the available experimental values[15].

Additionally, we found that the orbital structure of the Pt surface and its reactivity with oxygen atom are consistent with the interstitial electron model (IEM) of McAdon and Goddard as extended by Jacob and Goddard[13]. The importance of this result is evident, because all reaction processes will be studied based on this model. For the reaction steps (see below) we will use a 35-atomic $Pt_{14.13.8}$-cluster. This cluster allows one to calculate more difficult reactions on the surface by decreasing possible border effects, and include the main surface relaxations induced by the adsorbates.

3.2 Reaction Mechanisms

We used the 35-atom $Pt_{14.13.8}$-cluster to calculate binding structures and energetics for each possible intermediate (O, H, O_2, H_2, O_H, OOH, HOOH, H_2O) involved in the oxygen reduction reaction on the Pt(111) surface[16]. Atomic oxygen is most strongly bound at the μ_3-fcc position, while molecular O_2 prefers the bridge site. OOH prefers the same geometry as O_2 with one O covalently bound on top of a Pt atom (23.85 kcal/mol). Including zero-point energy (ZPE) a single H atom prefers the μ_3-fcc site over an on top site by ≈ 3.2 kcal/mol, whereas molecular H_2 undergoes dissociation to two on top bound H atoms wile adsorbing on Pt. OH and water show comparable binding structures (on top bound), but a different type of binding. The hydroxyl radical is covalently bound to one Pt atom (47.45 kcal/mol), and water uses the remaining lone pair orbital of its oxygen to attach to the surface atom (13.90 kcal/mol). In order to study a complete reaction pathway we also calculated all possible dissociation processes of the various intermediates on the Pt-cluster. Using the binding energies together with the dissociation barriers heats of formation (ΔH_f) were deduced, which then allowed us to study possible reaction pathways starting with gas-phase H_2

and O_2. We distinguished two main reaction pathways: O_2-Dissociation and OOH-Formation. Along the O_2-Dissociation pathway oxygen adsorbs on the surface, then dissociates, and finally reacts with hydrogen to form water. The rate-determining step for this mechanism is the $O^{ad} + H^{ad} \longrightarrow OH^{ad}$ reaction with a barrier of 31.66 kcal/mol and not the dissociation of O_2. Since O_2 changes its adsorption structure during dissociation the dissociation barrier lowers to only 15.02 kcal/mol. Along the OOH-Formation pathway adsorbed O2 first forms OOH with a surface hydrogen, and then generates OH via OOH dissociation, which finally reacts with another hydrogen to from water. In this mechanism the $OOH^{ad} \longrightarrow OH^{ad} + O^{ad}_{fcc}$ dissociation has the highest barrier of 17.13 kcal/mol. Therefore, the OOH-formation mechanism seems to be the most likely pathway for the cathode reaction. This pathway may additionally be supported by recombination of two adsorbed surface oxygens:

$$H^{g}_2 + O^{g}_2 \xrightarrow{-14.38} 2H^{ad} + O^{g}_2 \xrightarrow{-11.28} 2H^{ad} + O^{ad}_2 \xrightarrow[1.09]{-13.76}$$
$$H^{ad} + OH^{ad} + O^{ad}_{fcc} \xrightarrow[5.59]{-24.14} H_2O^{ad} + O^{ad}_{fcc} \xrightarrow{+13.90} H_2O^{g} + O^{ad}_{fcc}$$

These results in gas-phase allowed us to examine possible reaction mechanisms under more realistic conditions. Since water is generated during this reaction and since in the electrochemical system the cathode is solvated, we used DFT in combination with the self-consistent reaction field (SCRF) method to incorporate a hydrated environment and to study the structurally and energetically changes due to the water molecules. For instance, the structure and bond strength of an adsorbed water molecule on a Pt surface changes drastically. Polarized species, such as OH, show changes in the structure, binding and dissociation energies due to solvation. The surrounding water molecules influence the charge distribution and thus lead to

stronger or weaker surface connections, which also change the corresponding dissociation barriers. We found that the presence of the solvent changes the preference of the main reaction pathway. For instance, the formation of OH out of adsorbed H and O lowers its barrier by a factor of two, which then results in a O_2-Dissociation pathway dominated by the process of breaking the O=O bonds (as observed experimentally). In addition, the comparison of both reactions mechanisms in solution shows similar barriers for each of the single reaction steps, leading to a stronger interplay between both mechanisms.

4 Pt-based Alloys

4.1 Slab-Calculations for Extended Surfaces of $Pt_3Ni(111)$

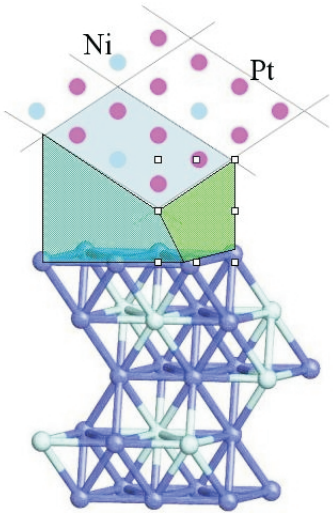

Fig. 2: Model of the unit-cell Pt-distribution: 100-50-83-50-100

Experiments on binary alloy catalysts, such as PtNi, PtCo and PtCr[3]

as well as ternary alloy catalysts[17], have shown an increased reaction rate (factor 25) for the oxygen reduction compared to pure Pt. However, it is also well known [18] that the lower coordinated surfaces of these alloys show strong segregation effects, in which Pt segregates to the surface. In order to understand the enhanced reactivity we first studied the surface structure of these alloys using periodic DFT-calculations (one unitcell is shown in Fig. 2). On the basis of different sized unitcells we build symmetric slabs consisting of 5-layers. By changing the composition and distribution of Pt and Ni atoms, and comparing their surface energies, we were able to establish the most stable surface structure (see Figure). Indeed, as a result of its higher cohesive energy Pt segregates to the surfaces and completely occupies all surface sites. In contrast, the second layers show an enrichment of Ni, leading to half the sites occupied by Pt atoms and the other half by Ni atoms. With 83% of the sites occupied by Pt, the alternating behavior can also be observed in the third layer. Comparing our findings to experimental measurements [18] (amount of Pt per layer: 100-48-89-75-75-) shows a very good agreement. Thus, on the basis of (semi-)infinitely extended $Pt_3Ni(111)$ or $Pt_3Co(111)$ surfaces, the surface reactivity is still dominated by Pt atoms. However, the distribution within the lower layers will also have an influence.

4.2 Pt_3Ni-Nanoparticles

Since in realistic electrochemical systems highly dispersed catalysts are used instead of mono-crystalline surfaces, after the periodic slab studies we performed cluster calculations on Pt/Ni clusters with different sizes, compositions, and distributions. The Pt/Ni-alloy system shows an element specific electron-configuration on the surface. Pt has the s1d9 character, whereby Ni is more s2d8. In extensive studies [19], we were able to define the most stable

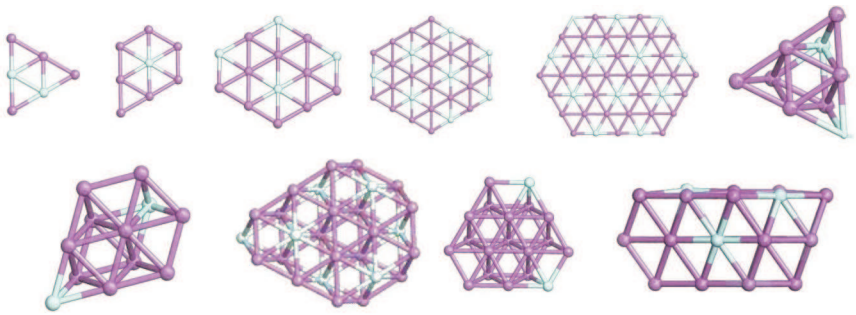

Fig. 3: Most stable structures for each cluster size

surface composition for the Pt/Ni-nanoparticles (Fig. 3). Equivalent to the bulk composition of Pt_3Ni, the alloy particle wants to keep the bulk ratio for the surface, too. According to this model, each Ni atom is surrounded by 6 Pt atoms. Thus, by not showing any surface segregation the nanoparticle will have a completely different behavior than the extended surface, resulting in different surface properties. Therefore, using surface science experiments to understand the processes of realistic electrochemical systems (with highly dispersed catalysts) is clearly incomplete in case of these alloys. On the basis of the found Pt/Ni structure we calculated the adsorption of atomic oxygen and hydrogen at all different adsorption sited on the surface. For on top binding there exist two different sites (on Pt and on Ni), for bridge and hollow binding in each case there are four distinguishable sites. The sum of all calculations finally led to the adsorption characteristics shown in Fig. 4.

Oxygen prefers three-fold sites, which consists of two Pt atoms and one Ni atom. Therefore, it is strongly bound around the Ni atoms with a hopping barrier of ≈ 2 eV. Compared to the pure Pt(111) surface, where the barrier was about 0.6 eV, oxygen is strongly localized on the alloy surface. In case of hydrogen, which is known to be very mobile on the Pt surface due to similar binding energies for all sites, the calculations on the Pt/Ni alloy indicate

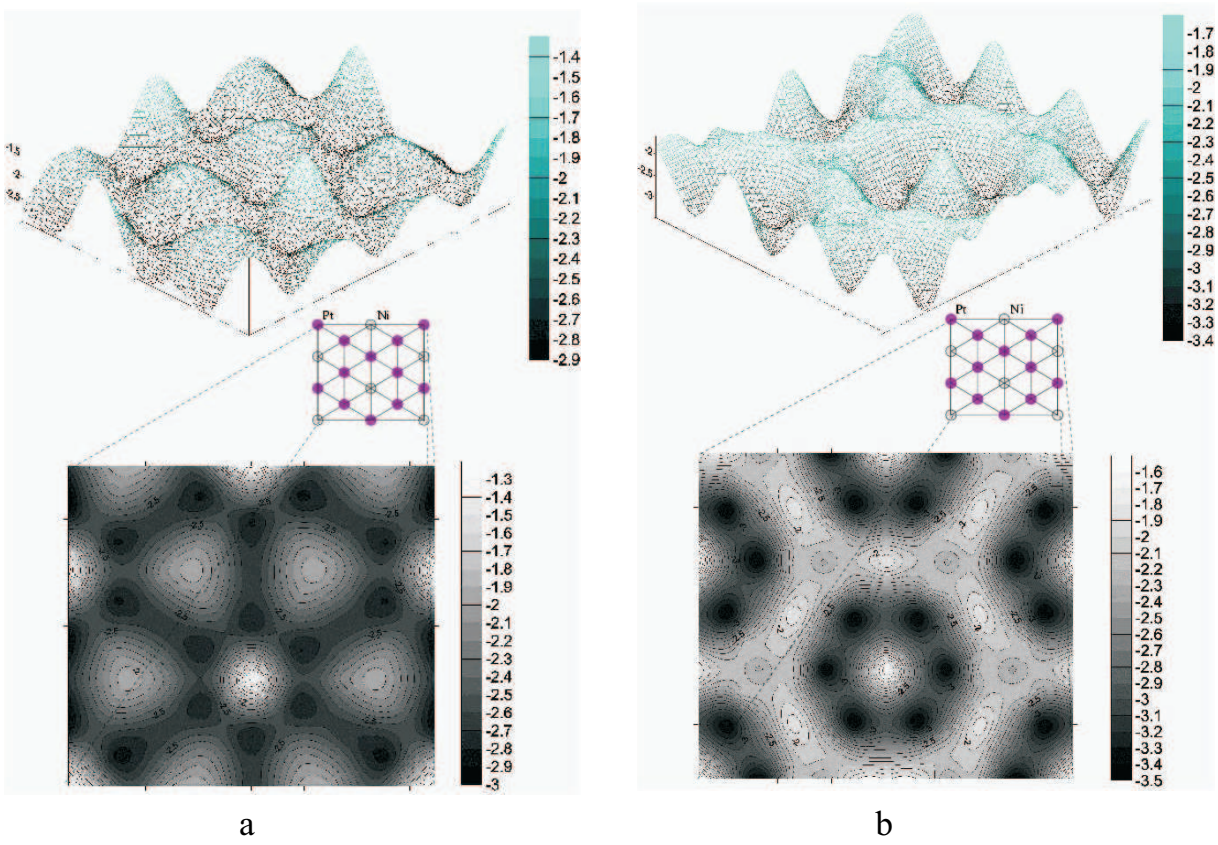

a b

Fig. 4: Hydrogen (a) and oxygen (b) binding characteristics (in eV) on the $Pt_3Ni(111)$ alloy surface

a different behavior. The hydrogen atoms are not such highly mobile on the complete surface as on channels between and on circles around the Ni atoms (see Fig. 4). The nearly fixed oxygen location and the constrained hydrogen mobility cause an increase in the probability that both atoms come close enough to react with each other. This example shows how alloying significantly changes the system character.

References

[1] Highfield, J. G.; Claude, E. Oguro, K. Electrochim. Acta 2001, 47, 465.

[2] Highfield, J. G.; Oguro, K.; Grushko, B. Electrochim. Acta 1999, 44, 2805.

[3] Beard, B. C.; Ross, P. N. Electrochem. Soc. 1990, 137, 3368.

[4] Glass, J. T.; Cahen , G. L.; Stoner, G. E.; Taylor, F. J. Electrochem. Soc. 1987, 134, 58.

[5] Becke, A. D. J. Chem. Phys., 1993, 98(7), 5648.

[6] Lee, C.; Yang, W.; Parr, R. G. Phys. Rev. B, 1988, 37, 785.

[7] Slater, J. C. Quantum Theory of Molecules and Solids, Vol. 4: The Self-Consistent Field for Molecules and Solids; McGraw-Hill: New York, 1974.

[8] Becke, A. D. Phys. Rev. A 1988, 38, 3098.

[9] Vosko, S. H.; Wilk, L.; Nusair, M. Can. J. Phys. 1980, 58, 1200.

[10] Jaguar 4.2/5.0; Schrödinger, InC.: Portland, Oregon, 2000/2002.

[11] Schultz, P. A. (unpublished); A description of the method is in: Feibelman, P. J. Phys. Rev. B 1987, 35, 2626; Verdozzi, C.; Schultz, P. A.; Wu, R.; Edwards, A. H.; Kioussis, N. Phys. Rev. B 2002, 66, 125408.

[12] Perdew, J. P.; Burke, K.; Ernzerhof, M. Phys. Rev. Lett. 1996, 88, 3865.

[13] Jacob, T.; Muller, R. P.; Goddard III., W. A. J. Phys. Chem. B 2003, 107, 9465.

[14] Eichler, A.; Mittendorfer, F.; Hafner, J. Phys. Rev. B 2000, 62, 4744.

[15] Parker, D. H.; Bartram, M. E.; Koel, B. E. Surf. Sci. 1989, 217, 489.

[16] Jacob, T.; Goddard III., W. A., to be submitted.

[17] Srinivasan, S.; Mukerjee, S. J. Electroanal. Chem. 1993, 357, 201; Gamburzev, S.; Velev, O. A.; Srinivasan, S.; Appleby, A. J.; Luczak, F. J.; Wheeler, D. "Carbon Supported Ternary Platinum Alloys Oxygen Reduction Catalysts for PEMFCs", Montreal, 1997.

[18] Lundberg, M. Phys. Rev. B 1987, 36(9), 4692

[19] Jacob, T., Merinov, B. V., Goddard III., W. A. Chem. Phys. Lett. 2004, 385(5-6), 374.

The frequency-dependent dipole polarisability of the mercury dimer from four-component relativistic density functional theory.

Nicola Gaston[1,*], *Peter Schwerdtfeger*[1] *and Trond Saue*[2]

[1] Institute of Fundamental Sciences, Massey University (Albany Campus), Private Bag 102904, North Shore MSC, Auckland, New Zealand;

[2] Laboratoire de Chimie Quantique et Modélisation Moléculaire, Université Louis Pasteur; 4, rue Blaise Pascal; F-67000 Strasbourg, France

While there has been great progress in the last twenty years in determining electric and optical properties of Van der Waals systems from first-principle quantum theoretical methods and statistical thermodynamics [1, 2], for mercury this is a rather difficult task [3, 4]. There is also evidence that the transition to the near metallic state occurs at large cluster size [5, 6, 7] unlike the other metals, and the many-body interaction expansion for mercury does not converge smoothly [8]. There are, however, still a number of fundamental questions open even for the simple dimer Hg_2.

Measurement of the collision-induced Raman scattering spectrum in mercury vapor as a function of the temperature and pressure provides one of the most direct means of probing the pair interaction potential and the form of

the induced pair polarisability anisotropy of the mercury dimer. It further gives important data for the determination of the virial coefficients in the Clausius-Mosotti equation. We have therefore calculated the dipole polarisability of the mercury dimer at both zero frequency and the frequency used in the experimental measurements (λ =488 nm) and determined the first two virial coefficients of the generalized Clausius-Mossotti function for the refractive index.

We include a complete treatment of relativistic effects by applying four-component density functional theory (DFT) choosing two different functionals, i.e. the local density approximation (LDA) and the most widely used hybrid functional B3LYP. Here the frequency-dependence of the Hg_2 dipole polarisability is directly obtained within four-component response theory.

In linear response theory the components of the frequency dependent polarisability tensor are

$$\alpha_{ij}(\omega) = -\left\langle\left\langle r_i; r_j \right\rangle\right\rangle_\omega \tag{20}$$

In the case of a linear molecule the components in the principal axis system are $\alpha_\parallel (= \alpha_{zz})$ and $\alpha_\perp (= \alpha_{xx} = \alpha_{yy})$, with the molecule oriented along the z-axis. From these components of the polarisability tensor we define the isotropic part of the polarisability, α, in the usual way as

$$\alpha = \frac{2\alpha_\perp + \alpha_\parallel}{3} = \frac{tr(\alpha)}{3} \tag{21}$$

and the polarisability anisotropy by

$$\beta = \alpha_\parallel - \alpha_\perp. \tag{22}$$

All calculations have been performed with a development version of the program package DIRAC [9], using the 4-component relativistic DFT implementation of response theory for molecular properties [10]. The formalism is

	DZ basis		TZ basis	
	DZ/LDA	DZ/B3LYP	TZ/LDA	TZ/B3LYP
Static	33.28	35.42	32.97	35.14
488 nm	37.19	39.24	36.93	38.99

Tab. 1: The atomic polarisability (in a.u.) as calculated with different basis sets (DZ and TZ) and density functionals. The experimentally derived value is 33.919(7) a.u. [12].

described in ref.[11]. An all-electron dual family triple zeta (TZ) Gaussian basis set was used for the polarisability calculations, i.e. $(28s25p19d12f2g)$ (uncontracted). The basis set superposition error was addressed using the counterpoise scheme, i.e. the dimer polarisability is defined as

$$\alpha(R) = \alpha_{Hg_2}(R) + 2\Delta^{BSSE}\alpha_{Hg}(R) \tag{23}$$

where $\Delta^{BSSE}\alpha_{Hg}$ is the BSSE correction to the atomic polarisability. With the basis set used this correction to the polarisability was consistently very small.

The results for the atomic polarisabilities are given in Table 1 for the two chosen functionals LDA and B3LYP.

Not surprisingly, the LDA and B3LYP functionals used in this study give greatly varying descriptions of binding in the dimer in comparison with the more accurate coupled cluster curve [6]. As expected LDA strongly overbinds, with a binding energy of 0.00874 a.u. at 2.98 Å (compared to experimental values of 0.0018 a.u. at 3.69 Å[13, 14]) whereas B3LYP produces a uniquely repulsive potential. Moreover, in the outer region where van der Waals forces are dominant, DFT underbinds as one expects. It has been noted that this leads to similar difficulties for the solid state structure even though mercury undergoes a transition to the metallic phase [6, 15, 8].

	$S_{\parallel}(-2)$	$S_{\parallel}(-4)$	$S_{\parallel}(-6)$	$S_{\perp}(-2)$	$S_{\perp}(-4)$	$S_{\perp}(-6)$
LDA	92.300	1647.699	38836.384	60.718	654.278	9881.548
B3LYP	95.422	1468.092	31134.425	64.182	635.005	9838.613

Tab. 2: The first three Cauchy moments for Hg_2 at $R = 3.69$ Å at the LDA and B3LYP level of theory for both the parallel and perpendicular components of the polarizability tensor (in a.u.).

For the first $X0_g^+ \rightarrow 1_u$ transition we obtain 0.20 (LDA) and 0.21 (B3LYP) a.u. compared to the experimental value of 0.171 a.u. [16]. For the second transition ($X0_g^+ \rightarrow 0_u^+$) we have 0.22 (LDA) and 0.24 (B3LYP) a.u. (exp. 0.179 a.u. [17]). Hence we expect the $\alpha(\omega)$ value at $\omega = 0.09337$ a.u. for Hg_2 to be reasonably accurate.

The Cauchy moments for the dimer may be calculated from a fit to the frequency dependent polarisability between zero and 0.12 a.u., i.e. before the first singularity. These are shown in Table 2.

Since the Cauchy sequence of the atomic polarizability of mercury is well known from experimental work of Goebel and Hohm [12], it is convenient to introduce the frequency dependent interaction polarizability,

$$\alpha_{Hg_2}(\omega) = 2\alpha_{Hg}(\omega) + \alpha_{int}(\omega) \tag{24}$$

In Figure 1 the isotropic average of the interaction polarisability, α_{int}, is given as well as the anisotropic β values, which may be compared to the experimental curve. The agreement between the anisotropic values and experiment is good, although the curves cross near the potential minimum.

The major disagreement in the anisotropy is at short distances, below 3.5 Å the curves diverge where the potential curve becomes repulsive. At short distances we expect rather accurate experimental results [18], since the potential data used from Koperski's work [14] is rather accurate. However,

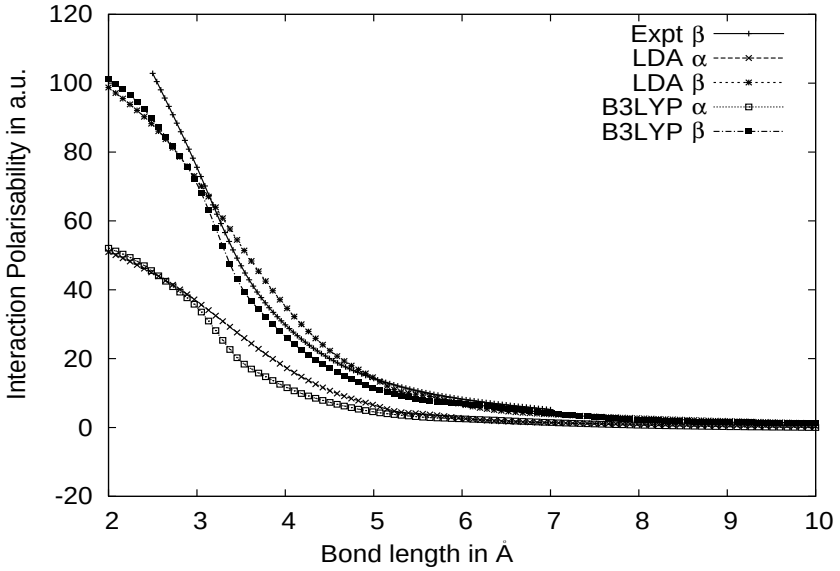

Fig. 1: The frequency dependent polarisability (at $\omega = 0.09337$ a.u.) in isotropic and anisotropic components for Hg_2 at different levels of theory.

we also find larger deviations in the long range region.

The extended Clausius-Mosotti equation for the refractive index is given by [19],

$$\frac{n(\omega,T)^2-1}{n(\omega,T)^2+2} = A_R(\omega,T)\rho + B_R(\omega,T)\rho^2 + C_R(\omega,T)\rho^3 + ... \qquad (25)$$

where n is the refractive index, A_R, B_R and C_R the first three refractivity virial coefficients (the subscript R stands for the refractive index), ω the frequency of light and T is the temperature of the system. The first virial coefficient is given directly by the frequency dependent atomic polarizability. The second virial coefficient can be determined from classical statistical thermodynamics,

$$B_R(\omega,T) = \frac{4\pi N_A^2}{6\epsilon_0}\int_{[0,\infty)} \alpha_{int}(\omega,R)exp(-V(R)/kT)R^2\,dR \qquad (26)$$

k is the Boltzmann constant and $V(R)$ the interaction potential.

	$B_R^{(0)}$	$B_R^{(2)}$	$B_R^{(4)}$
LDA			
c_1	9.7347×10^7	3.7358×10^9	7.4077×10^{10}
c_2	2.8746×10^4	2.3078×10^6	4.5643×10^7
c_3	1.0515×10^3	6.1876×10^4	1.2266×10^6
B3LYP			
c_1	8.3672×10^7	1.5520×10^9	2.8781×10^{10}
c_2	1.1024×10^4	8.2186×10^5	1.5232×10^7
c_3	7.9539×10^2	1.8259×10^4	3.3861×10^5

Tab. 3: The coefficients of eq.(29) which fit the temperature dependence of the refractivity virial coefficients $B_R^{(0)}$, $B_R^{(2)}$ and $B_R^{(4)}$ as defined in eq.(12) (in cm^6 mol^{-2}).

A Cauchy series for the virial coefficients is

$$B_R(\omega, T) = B_R(0, T) + B_R^{(2)}(T)\omega^2 + B_R^{(4)}(T)\omega^4 + \ldots \tag{27}$$

where the coefficients $B_R^{(2)}(T)$ and $B_R^{(4)}(T)$ are obtained from using the Cauchy coefficients for $\alpha_{int}(\omega, R)$ from Table 2, combined as in eq. 21 to give the isotropic interaction part. The distance dependence of the Cauchy coefficients was obtained by fitting to

$$S(-2k-2, R) = (\frac{a}{R} + \frac{b}{R^3})S(-2k-2, R_0) \tag{28}$$

where $S(-2k-2, R_0)$ are the equilibrium distance coefficients as in Table 2. a and b were fitted to give the correct distance dependence at $\omega = 0.09337$ a.u. The temperature dependence of these coefficients can then be summarised as

$$B_R(T) = c_1\frac{1}{T^2} + c_2\frac{1}{T} + c_3 \tag{29}$$

with the coefficients given in Table 3.

References

[1] B. Fernández, C. Hättig, H. Koch and A. Rizzo, J. Chem. Phys., **110** 2872 (1999).

[2] A. Rizzo, K. Ruud, D. M. Bishop, Mol. Phys., **100** 799 (2002).

[3] F. Hensel and W. Warren, *Fluid Metal* (Princeton, New Jersey, 1999).

[4] M. Ross and F. Hensel, J. Phys.: Condens. Matter **8**, 1909 (1996).

[5] R. Busani, M. Folkers, and O. Cheshnovsky, Phys. Rev. Lett. **81**, 3836 (1998).

[6] G.E. Moyano, R. Wesendrup, T. Söhnel and P. Schwerdtfeger, Phys. Rev. Lett. **89**, 103401 (2002).

[7] H. Uchtmann, K. Rademann, and F. Hensel, Ann. Phys. **48**, 207 (1991).

[8] B. Paulus, K. Rosciszewski, H. Stoll, N. Gaston, P. Schwerdtfeger, Phys. Rev. B **70** 165106 (2004).

[9] "Dirac, a relativistic ab initio electronic structure program, Release DIRAC04.0 (2004)", written by H. J. Aa. Jensen, T. Saue, L. Visscher *et al.* (http://dirac.chem.sdu.dk)

[10] P. Salek, T. Helgaker and T. Saue, Chem. Phys.,in press. (2004).

[11] Trond Saue and H. J. Aa. Jensen, J. Chem. Phys., **118**, 522 (2003).

[12] D. Goebel and U. Hohm, J. Phys. Chem., **100**, 7710 (1996).

[13] P. Schwerdtfeger, R. Wesendrup, G. E. Moyano, A. J. Sadlej, J. Greif and F. Hensel, J. Chem., Phys. **114** 16 (2001).

[14] J. Koperski, J. B. Atkinson and L. Krause, Chem. Phys. Lett. **219** 161 (1994).

[15] B. Paulus and K. Rosciszewski, Chem. Phys. Lett. **394** 96 (2004).

[16] A. Zehnacker, M. C. Duval, C. Jouvet, C. Lardeux-Dedonder, D. Solgadi, B. Soep, and O. B. D'Azy, J. Chem. Phys. Lett. **219** 161 (1994).

[17] J. Koperski, J. B. Atkinson and L. Krause, Chem. Phys. **86** 6565 (1987).

[18] Jörn N. Greif-Wüstenbecker, Thesis Philipps University, Marburg *The polarisability anisotropy of mercury dimer obtained from collision-induced Raman spectroscopy* (2000).

[19] R. K. Bullough, J. Phys. A **3**, 708, 726 (1970).

Second day: 26 June 2005

Time	Speaker	Title
	Chair: Valeria Pershina	
9.00 – 9.40	Matthias Schädel	Chemical separation and characterization of superheavy elements.
9.40 – 10.20	Heinz Gäggeler	From few atoms/min (Rf) to few atoms/week(Z=112).
10.20 – 10.40	Coffee	
	Chair: James Wright	
10.40 – 11.20	Warren Roper	Compounds of Ru or Os with bonds to B, Si and Sn.
11.20 – 11.45	Pennelope Brothers	Theoretical investigations into transition meta-Group 13 element bonding
11.45 – 12.10	Tilo Söhnel	Fe, Ru and Ir containing Tin Cluster Compounds.
12.10 – 14.00	Lunch	
	Chair: Heinz Gäggeler	
14.00 – 14.40	Robert Eichler	Thermodynamic data evaluation for gas phase chemical experiments with transactinides.
14.40 – 15.05	Hicham Idriss	Carbon monoxide reaction with UO_2 (111) single crystal and thin film surfaces.
15.05 – 15.30	Graham A. Bowmaker	Solid-state NMR of silver and mercury compounds.
15.30 – 16.00	Coffee	
	Chair: G. Bowmaker	
16.00 – 16.25	James Wright	Tethered Osmabenzenes Derived from an Osmabenzofuran
16.25 – 16.50	Alistair Nielson	A case for linear agostic interaction in tantalum chemistry
16.50 – 17.15	Peter Schwerdtfeger	How good is density functional theory for field gradients?
17.15 – 18.00	Final Discussions and Reflections	

Chemical separation and characterization of superheavy elements

Physical, chemical, technological and metrological challenges

Matthias Schädel

Gesellschaft für Schwerionenforschung (GSI), Planckstr. 1, D-64291 Darmstadt.

The number of chemical elements has considerably increased over the last decades. These new, man-made elements at the far end of the Periodic Table are transactinides and are located in the area of the long-awaited for superheavy elements (SHE). The discovery of elements up to atomic number 112 with the most recent experiment at RIKEN presumably up to 113 is based on solid grounds; see e.g. [1] for a recent compilation. However, all nuclides produced in the Pb and Bi target based nuclear reactions dubbed "cold-fusion" lead to very short-lived nuclides which are not usable in chemical investigations (with the exception of element 104 and 105). Most pleasantly, more elements and longer-lived nuclides are on the horizon and a challenge for chemical studies. Yu. Ts. Oganessian and coworkers [2] reported on the observation of elements up to 116 and an indication even for element 118. This opens up a thrilling region for heavy element chemists to probe the influence of increasingly strong relativistic effects and the structure of the Periodic Table at its end; see Figure 1.

Superheavy element chemistry experiments usually exploit an advantage

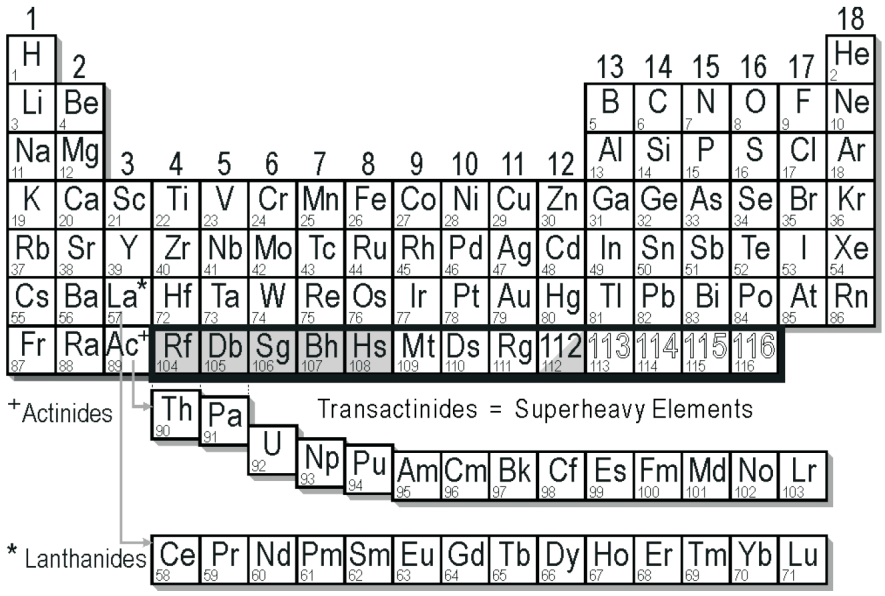

Fig. 1: Periodic Table of the Elements. The known transactinide elements 104 through 112 shall take the positions of the seventh period transition metals below Hf in group 4 and Hg in group 12. While chemical studies have - also from their observed chemical behavior - justified placing the elements Rf through Hs into group 4 to 8 of the Periodic Table, the "chemically unknown" heavier elements (full symbols for "known" elements and open symbols for yet unconfirmed reports) still need to be investigated. The arrangement of the actinides reflects that the first actinide elements still resemble, to a decreasing extent, the chemistry of d-elements: Th below group 4 elements Zr and Hf, Pa below Nb and Ta, and U below the group 6 elements Mo and W.

of so-called "hot-fusion" reactions which lead to the synthesis of the most neutron-rich, longest-lived isotopes of a given element. So the most neutron-rich isotope of an actinide element is applied as target material, e.g. ^{248}Cm is frequently used, and is irradiated with neutron-rich light ion beams like ^{18}O, ^{22}Ne and ^{26}Mg. All these reactions lead to a one-atom-at-a-time production of SHE - decreasing from about one atom per minute for Rf to about one atom per day for Hs.

Already the first chemical studies showed that Rf and Db (elements 104 and 105) belong into group 4 and 5 of the periodic table; they are trans-actinides and - from nuclear aspects - superheavy elements. It was only in recent years, that a large number of experiments did not only shed light on many fascinating and unexpected chemical properties of Rf and Db but allowed to stepwise climb up the exceedingly difficult path to the subsequent elements Sg, Bh and Hs; see Ref. [3] for a comprehensive coverage of this development. This success in superheavy element chemistry was only feasible because of an enormous progress in many fields to meet a large number of physical, chemical, technological and metrological challenges [3]. This contribution will focus on these developments and on their perspectives. Some aspects will be described in a more general way and some exemplary ones will be discussed in more detail including related experimental results.

The synthesis of SHE always starts with the availability of a stable, high intense heavy-ion beam. Electron cyclotron resonance (ECR) ion sources coupled to a powerful accelerator - are the state-of-the-art instruments to provide such beams. A low material consumption is an important feature for rare isotope like ^{18}O, ^{22}Ne, ^{26}Mg or ^{48}Ca. To make use of these beams, target technology developments, e.g. GSI's rotating target wheel ARTESIA, were necessary to withstand the heat load on windows, actinide target and backings; see ref. [4] for more information about the ARTESIA target production. In contrast to recoil separators typical chemistry experiments require a pressure of at least 1 bar in the recoil chamber were the nuclear reaction products are collected. To find metal window foils which are thick enough to sustain this pressure difference and are as thin as possible to minimize the energy loss from the heavy ion beam is a delicate optimization. Be foils with typical thicknesses of about 20 μm are frequently used. The future application of

recoil separators as pre-separators on the front-end of a SHE chemistry experiment will have the advantage that there is no - or almost no (1 mbar) - pressure drop across a window foil. Moreover, applying differential pumping, as it is under development for the new TransActinide Separator and Chemistry Apparatus (TASCA) [5] totally eliminates the need for window foils in the target area. However, here the necessary window foil at the end of the recoils separator constitutes a problem. This foil is needed to interface the separator with a so-called Recoil Transfer Chamber (RTC) a chamber with a similar purpose as the traditional recoil chamber. Here it is the low recoil velocity of especially products from reactions of light projectiles on heavy element targets which constitutes a challenge.

At high heavy-ion beam intensities of a few times 10^{12} s^{-1} or even 10^{13} s^{-1} He/cluster-jet transport systems have reached their limits. These traditionally used tools to transport non-volatile species from a recoil chamber to a chemistry apparatus become highly inefficient due to the strong interference of the heavy-ion beam with the transport gas and the cluster material. Again this is one of the strong arguments to apply separators like TASCA or the Berkeley Gas-filled Separator (BGS) the pioneering instrument in this field.

Not so much to circumvent problems with cluster-jet transport under high intense heavy-ion beam conditions but to exploit a number of advantages, the formation of volatile compounds directly in the recoil chamber [6] and its transport to the chemistry/detector device was applied in all Hs experiments [7, 8]. Transport of the volatile HsO_4 in a He/O_2 gas mixture was not only highly efficient but, at the same time, provided an excellent chemical separation from all non-volatile reaction products already in the recoil chamber. The developments of chambers combining features to chemically characterize

HsO4 and to detect atom-at-a-time the a-decay and/or spontaneous fission (SF) of single Hs isotopes (and their nuclear decay daughter products) established another challenge. One kind of instrument, the Cryo On-Line Detector (COLD) [6] and its forerunner the Cryo-Thermochromatographic Separator (CTS) [9] , allows to determine the adsorption temperature along a temperature gradient from e.g. room temperature to about 1700°C. Here, gas purification to reduce the partial pressure of water in the gas to 1 ppm or below - to avoid ice formation already at moderately low temperatures - is a critical issue. The CALLISTO experiment [8] used a chemically reactive surface opposite to PIN-diode detectors to investigate the HsO4 behavior.

Presently, element 112 is one of the hottest and most challenging topics in SHE chemistry. It also constitutes a transition from a more traditional approach in SHE chemistry - to form a chemical compound and chemically investigate this compound - to studies of an element in its atomic state. As in the Hs experiments, also in the element 112 experiment - and presumably later in an element 114 experiment more or less "volatile" single atoms are transported in a flowing gas to a detector set-up. Again, as in the Hs experiments, it will be the deposition temperature or the adsorption on a "chemically" reactive surface which will characterize the elements in the element 114 region.

Meeting the challenges of very cold temperatures in some of these experiments just mirrors the opposite task to cope with relatively high temperatures in gas-chromatographic studies of Sg compounds [10, 11] with OLGA [12] and HITGAS [13]. Corrosive gases, e.g. used in gas-chromatographic studies of Rf and Db, constitute extra problems; see e.g. [14].

Aqueous chemistry with the Automated Rapid Chemistry Apparatus (ARCA) [15] has reached Sg [10, 16] and has unraveled interesting and some-

times surprising chemical properties of Rf and Db; see ref. [17, 18] for more details. New developments based upon the ARCA technique - together with the implementation of an innovative automated sample preparation and detection technique has led to very successful detailed investigations of Rf with the "Automated Ion-exchange separation apparatus coupled with the Detection system for Alpha spectroscopy" (AIDA) [19, 20, 21, 22]. As in previous experiments it was shown that Rf belongs into group 4 of the Periodic Table. However, detailed studies of the fluoride complexation of Rf revealed stunning differences between Rf and its lighter homologues Zr and Hf [23]. For the first time the technically mature AIDA even allows to measure a complete elution curve for a transactinide element [24, 25]. This development will give access to more detailed chemical studies of the lighter SHE. However, the discontinuous batch-wise operation of ARCA and AIDA poses severe limits on the accessible nuclides. Half-lives of more than 10 s preferably more than 30 s are required not to be harmed by too severe nuclear decay losses during the product collection and the sample preparation.

New developments are under way aiming at extending the studies of SHE in aqueous solution beyond Sg. One approach is making use of electrochemical deposition techniques [26]. Bohrium and elements 112 and 114 are presumably good candidates for such investigations if sufficiently long-lived nuclides ($T_{1/2} > 10$ s) are accessible. A new quality of chemical studies is on the horizon when combining chemical techniques with recoil separators. This can already be seen from results of SISAK a fast and continuously operating liquid-liquid extraction technique coupled to the BGS [27]. The SISAK technique in itself still allows further improvements, e.g. by miniaturization [28]. TASCA at GSI [5], which will become available in about a year or two, will open up new perspectives for chemistry experiments at a

recoil separator.

References

[1] S. Hofmann, G. Münzenberg, M. Schädel, Nucl. Phys. News **14** (2004) 5.

[2] Yu. Ts. Oganessian et al., Phys. Rev. C **70** (2994) 064609.

[3] M. Schädel (Edt.), The Chemistry of Superheavy Elements, Kluwer Academic Publishers, Dordrecht, 2003.

[4] K. Eberhardt et al., Nucl. Instr. and Meth. A **521** (2004) 208.

[5] Information about the TASCA project, which is under construction at the GSI, and more interesting details, general information of this community and links to a large number of workshop contributions can be found at: http://www.gsi.de/tasca

[6] Ch. Düllmann et al. Nucl. Instr. and Meth. A **479** (2002) 631.

[7] Ch. Düllmann et al., NATURE **418** (2002) 859.

[8] A. von Zweidorf et al., Radiochim. Acta **92** (2004) 855.

[9] U.W. Kirbach et al., Nucl. Instr. and Meth. A **484** (2002) 587.

[10] M. Schädel et al., NATURE **388** (1997) 55.

[11] A. Türler et al., Angew. Chem. Int. Ed. **38** (1999) 2212.

[12] A. Türler, Radiochim. Acta **72** (1996) 7.

[13] S. Hübener et al., Radiochim. Acta **89** (2001) 737.

[14] A. Türler, K.E. Gregorich Experimental Techniques, pp. 117-157, and H.W. Gäggeler, A. Türler Gas-Phase Chemistry, pp. 237-289 in ref.[3].

[15] M. Schädel et al., ARCA

[16] M. Schädel et al., Radiochim. Acta **77** (1997) 149, and Radiochim. Acta 83 (1998) 163.

[17] J.V. Kratz Liquid-Phase Chemistry, pp. 159-203 in Ref.[3].

[18] J.V. Kratz, Pure Appl. Chem. **75** (2003) 103.

[19] Y. Nagame et al., J. Nucl. Radiochem. Sci. **3** (2002) 129.

[20] H. Haba et al., J. Nucl. Radiochem. Sci. **3** (2002) 143.

[21] Y. Nagame et al., Czech. J. Phys. Suppl. **53** (2003) A299.

[22] Y. Nagame et al., Nucl. Phys. A **734** (2004) 124.

[23] H. Haba et al., J. Am. Chem Soc. **126** (2004) 5219.

[24] Y. Nagame et al., Proceedings of the 6th International Conference on Nuclear and Radiochemistry (NRC-6), Aachen, 2004, in print.

[25] A. Toyoshima et al., J. Nucl. Radiochem. Sci. **5** (2002) 45.

[26] H. Hummrich, J.V. Kratz, Electrochemical deposition A tool for the investigation of superheavy elements? in: S.M. Qaim, H.H. Coenen (Edts.) Advances in Nuclear and Radiochemistry, NRC-6 Extended Abstracts, Forschungszentrum Jülich, 2004, p. 133-135, and GSI Scientific Report 2003, GSI 2004-1, May 2004, p. 199.

[27] J.P. Omtvedt et al., J. Nucl. Radiochem. Sci. **3** (2002) 121.

[28] K. Eberhardt et al., Institut für Kernchemie, Universität Mainz, Jahresbericht 2003, p. A7.

From few atoms/min (Rf) to few atoms/week(Z=112)

cutting-edge chemistry experiments with heaviest elements

Heinz W. Gäggeler

Paul Scherrer Institut, 5232 Villigen, Switzerland and Dept. of Chemistry & Biochemistry, Bern University, Freiestrasse 3, 3012 Bern, Switzerland

Heaviest elements with atomic numbers above 103 (lawrencium, Lr) the transactinides - can only be produced at a single-atom-at-a-time level. For nuclear physics reasons, isotopes of these elements have essentially no liquid drop (i.e. macroscopic) stability. They exist exclusively due to shell effects. Such nuclides are also called superheavy elements (SHE).

Production of SHE is possible in heavy ion fusion reactions at energies close to the Coulomb barrier, e.g. at the fusion barrier according to Bass. Depending on the Q-value of the reaction, given by the mass excess values of the interacting nuclei, fusion reactions are called "hot" or "cold". In hot fusion reactions the minimum excitation energy at the barrier amounts to typical values of 30 - 40 MeV and in cold fusion reactions to 10 - 20 MeV, respectively. As a consequence, usually 3 to 5 neutrons are evaporated from primary products formed in hot fusion reactions to reach the ground state of the evaporation residue whereas only 1 to 2 neutrons in cold fusion reactions. Due to high probabilities of excited primary products to decay by prompt

fission if compared to evaporating a neutron, survival probabilities are very small. Moreover, in more symmetric cold fusion reactions with Pb or Bi targets, formation of primary products is hindered due to strong Coulomb repulsion. As a consequence, production rates of surviving atoms of SHE are usually very small. Figure 1 depicts an overview on production rates that can be achieved with current technologies (maximum beam intensities, cooled targets etc.) in hot or cold fusion reactions. Some typical reactions that have been used in recent years for chemical investigation are listed in table 1. In the following a short overview is given on gas chemical studies of transactinides. Most of the data described below have been obtained with very few atoms, typically on the order of ten.

Except for the very first historic investigations of Rf with frontal gas chromatography [1], later experiments applied on-line chemical separation techniques coupled to on-line detection arrays. Of special importance were two devices, OLGA [2] and IVO [3]. OLGA (On-Line Gas chemistry Apparatus) was developed to perform isothermal gas adsorption chromatography experiments of short-lived species with lifetimes down to a few seconds in quartz columns. OLGA enabled chemical investigations of volatile halides or oxyhalides at maximum temperatures of 500 °C. In a special version, this technique was also used to study volatile oxy-hydroxides at temperatures up to 1000 °C [4]. IVO (In-situ Volatility and On-line detection), on the other hand is an on-line chemistry device coupled to an on-line thermochromatographic detection array. Hence, detectors are used as chemical sensors on which adsorption studies may be performed. An overview on techniques can be found in [5].

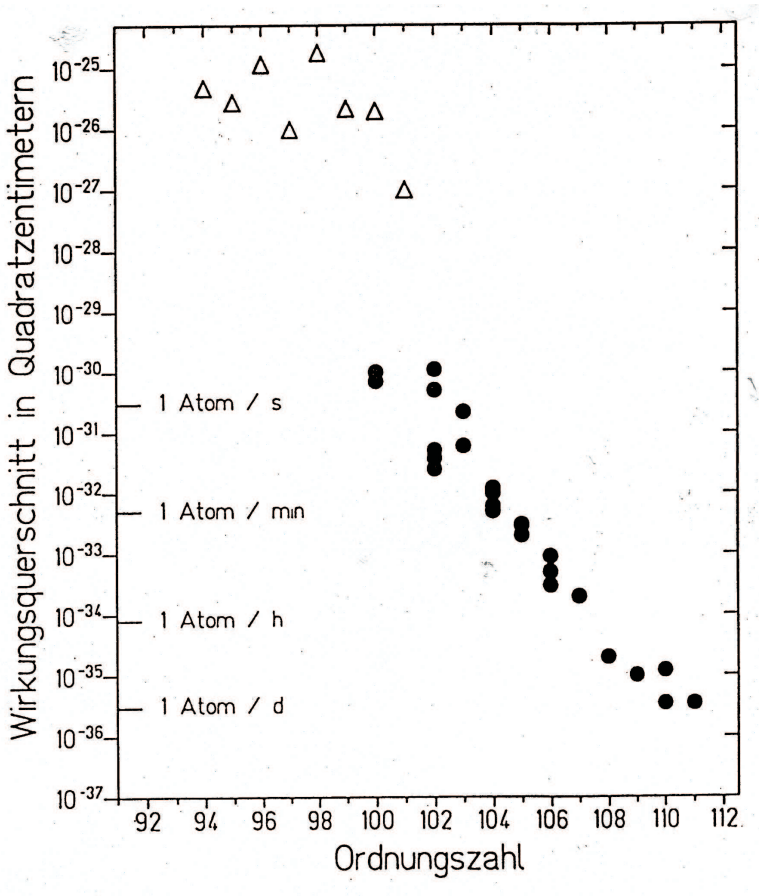

Fig. 1: Typical production rates for formation of heavy elements in nuclear fusion reactions (from [6])

1 Rutherfordium (Rf)

So far, most gas chemical investigations of this element have been conducted with Rf4+in form of its chloride, oxychloride or bromide. In one experiment an attempt was made to search for a p-element behaviour of Rf, based on a predicted ground-state configuration of $[Rn]5f^{14}7s^27p^2$ or $[Rn]5f^{14}6d7s^27p$, respectively. However, the experiment did not yield any evidence for such a configuration which should result in a similarity to Pb [7]. OLGA experiments yield retention temperatures that enable the determination of adsorp-

Element	Prod. rate (Atoms/h)	Half-life (s)	Reaction
Rf (104)	30	78 (^{261}Rf)	^{248}Cm(^{18}O;5n)
Db (105)	30	34 (^{262}Db)	^{249}Bk(^{18}O;5n)
Sg (106)	2	7 (^{265}Sg)	^{248}Cm(^{22}Ne;5n)
Bh (107)	0.5	17 (^{267}Bh)	^{248}Cm(^{22}Ne;5n)
Hs (108)	0.25	10 (^{269}Hs)	^{248}Cm(^{26}Mg;5n)
Z=112	0.05	4* or 300* (^{283}112)	^{238}U(^{748}Ca;3n)

Tab. 1: Production rates and half-lives of transactinide nuclides used for chemical studies. *controversial literature data [18, 19]

tion enthalpies. Figure 2 shows measured adsorption enthalpies of group 4 chlo-rides and bromides. It was argued that the obvious "reversal" of the trend of ΔH^0_a when going from Zr via Hf to Rf is evidence for relativistic effects in the chemistry of Rf [8].

2 Dubnium (Db)

Gas chemical studies of Db were performed with Db^{5+} and proved to be extremely challenging due to its high tendency to form oxyhalides. Therefore, some chromatographic data that were published as retention temperatures of pure halides could be erroneous, since they might probably represent the behaviour of the oxy-halide. Such an example is an investigation of $DbBr_5$ [10].

Figure 3 depicts experimental adsorption enthalpies of group 5 halides. It is evident that no reversal is observed as found in group 4 (see Fig. 2). However, if the value depicted for DbBr5 is actually from DbOBr3, then a higher ΔH^0_a value should result, since oxyhalides are less volatile compared to pure halides of the same oxidation state. Therefore, the trend shown in

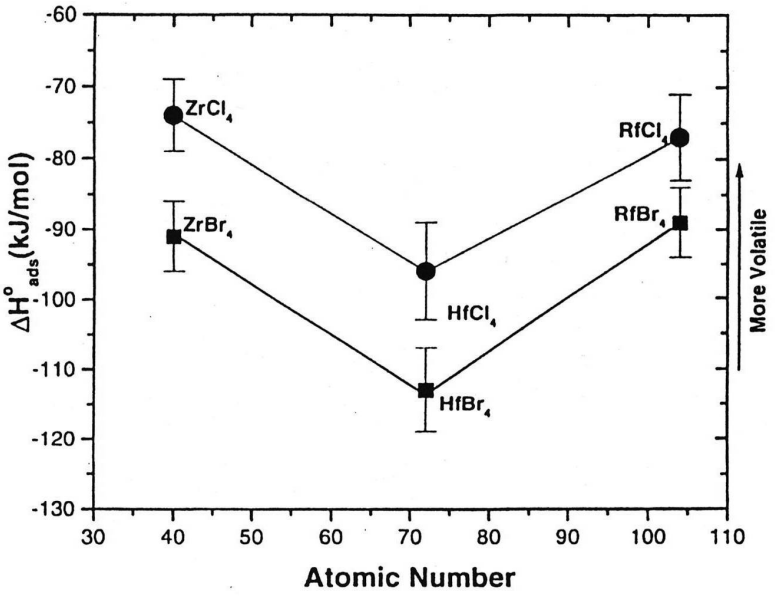

Fig. 2: Adsorption enthalpies of chlorides and bromides of Zr, Hf and Rf on quartz surfaces (from [9]

Fig. 3 may be questioned.

3 Seaborgium (Sg)

Chemical investigations of Sg have been conducted with Sg^{6+}. The pure halide of Sg^{6+} is not stable. From thermodynamic considerations the most stable compound in a halogenating atmosphere is the dioxydihalide. So far, only oxychlorides have been studied. The adsorption data of Mo, W and Sg indicate a normal trend within group 6 [12] (Fig. 4). In one study the adsorption behaviour of dioxydihydroxide of Mo, W and Sg on quartz was investigated. It turned out that these molecules do not interact on quartz surfaces via mobile adsorption but undergo surface reactions in form of dissociative adsorption [4].

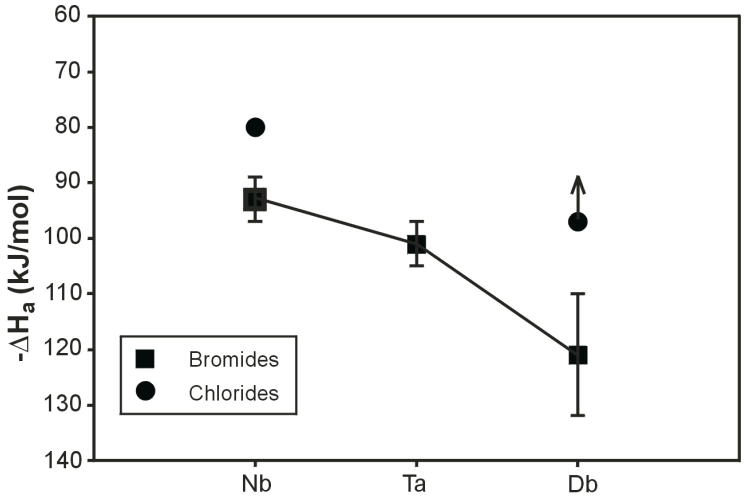

Fig. 3: Adsorption enthalpies of chlorides and bromides of Nb, Ta and Db on quartz surfaces (from [11])

4 Bohrium (Bh)

Bohrium studies were performed from the highest oxidation state Bh^{7+}. For thermo-dynamic reasons the most stable compound in a halogenating atmosphere is the trioxyhalide. As for Sg, the only system that has been investigated so far is the oxychloride. Measured adsorption enthalpies for the trioxychlorides of Tc, Re and Bh are also depicted in figure 4 [13]. It is evident, that group 7 oxychlorides have lower adsorption enthalpies compared to the corresponding group 6 compounds. Again, a linear trend is found for the adsorption enthalpies of oxychlorides when going along the members of group 7.

5 Hassium (Hs)

Elements of group 8 exhibit a rather special feature, they form with oxygen very volatile tetroxides that are gaseous under ambient conditions at a single

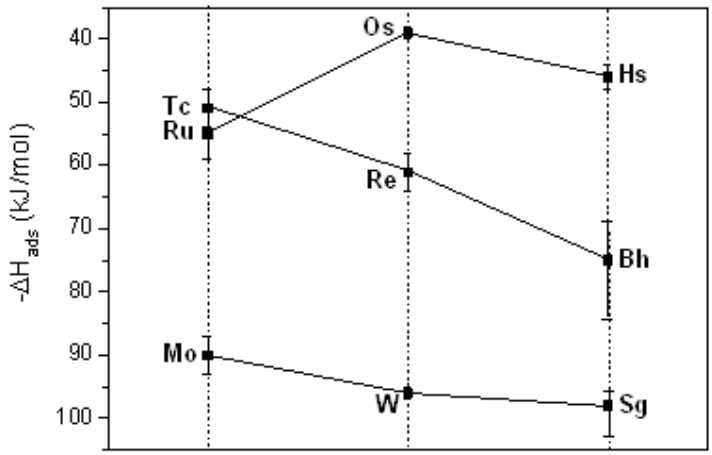

Fig. 4: Adsorption enthalpies of dioxydichlorides of Mo, W and Sg (from [12]) and of trioxychlorides of Tc, Re and Bh (from [13]), respectively, on quartz surfaces. Also shown are adsorption enthalpies of tetroxides of OsO4 and HsO4 on silicon nitride detector surfaces [14] as well as of RuO_4 on quartz [11].

molecule level in an inert environment (e.g. quartz). In the first chemical study of heavy members of group 8 deposition temperatures of OsO_4 and HsO_4 along a thermochromatographic PIN detector array were measured. PIN diodes are semiconductor detectors with a silicon nitride surface. Unfortunately, it was not possible to also investigate the behaviour of RuO_4 on the same detector surface. Therefore, an independent determination of the adsorption enthalpy on quartz surface is depicted in figure 4. For OsO_4 identical adsorption enthalpies on silicon nitride and on quartz were observed. As RuO_4 is very unstable it can not be ruled out that the species investigated was not the tetroxide but the trioxide! This would explain the unexpectedly high adsorption enthalpy. In this case the reversal of the trend depicted in figure 4 may be questioned.

6 Element 112

About a chemical indentification of element 112 was reported in [15]. Based on several predictions, this element as a member of group 12 is expected to be more volatile than mercury, possibly as volatile as radon. Indeed, a non-Hg like but much more radon like behaviour of element 112 was observed [15]. In additional experiments, first, an indi-cation for a similar behaviour was claimed [16] that, however, in a third study could not be confirmed [17]! Hence, currently the situation concerning the chemical property of Z=112 in its elemental state remains controversial and requires additional investigation.

References

[1] I. Zvara, et al., At. Energ. **21**, 83 (1966)

[2] H.W. Gäggeler et al., Nucl. Instr. Meth., **A309**, 201 (1991)

[3] C.E. Düllmann et al., Nucl. Instr. Meth., **A479**, 631 (2002)

[4] S. Hübener et al., Radiochim. Acta, **89**, 737 (2001)

[5] Chemistry of Superheavy Elements, M. Schädel (Ed.), Kluwer Acad. Publ. (2003)

[6] G. Münzenber, M. Schädel, Moderne Alchemie, VIEWEG, ISBN 3-528-06474-9

[7] B.L. Zhuikov et al., Radiochim. Acta **46**, 113 (1989)

[8] A. Türler et al., J. Alloys Comp., **271-273**, 287 (1998)

[9] K.E. Gregorich, in: Proc. "The Robert A. Welch Foundation", 41^{st} Conf. on Chem. Res. The Transactinide Elements, Houston, Texas, Oct. 27-28 (1998), p.95

[10] H.W. Gäggeler et al., Radiochim. Acta, **57**, 93 (1992)

[11] H.W. Gäggeler, A. Türler, Gas-Phase Chemistry, in [5]

[12] A. Türler et al., Angew. Chem. Int. Ed., **38**, 2212 (1999)

[13] R. Eichler et al., Nature, **407**, 63 (2000)

[14] C.E. Düllmann et al., Nature, **418**, 859 (2002)

[15] A. B. Yakushev et al., Radiochim. Acta, **91**, 433 (2003)

[16] H.W. Gäggeler et al., Nucl. Phys. **A734**, 208 (2004)

[17] R. Eichler et al., Radiochim. Acta, to be submitted (2005)

[18] Yu. T. Oganessian et al., Nature, **400**, 242 (1999)

[19] Yu. T. Oganessian et al., Phys. Rev. **C70**, 064609 (2004)

Compounds of Ru or Os with bonds to B, Si and Sn

Warren R. Roper

Department of Chemistry, The University of Auckland, New Zealand

Compounds of the type $L_nM\text{-}BR_2$ are involved in metal-catalyzed processes such as the hydroboration of alkenes, the diboration of alkynes, and even the direct borylation of alkanes. Likewise, compounds of the type $L_nM\text{-}SiR_3$ and $L_nM\text{-}SnR_3$ are involved in metal-catalyzed hydrosilation and hydrostannation, respectively. In this lecture the syntheses, structures and reaction patterns of boryl, $L_nM\text{-}BR_2$, silyl, $L_nM\text{-}SiR_3$, and stannyl, $L_nM\text{-}SnR_3$, complexes where M = Ru or Os, will be examined. Structural information on selected compounds is revealing of the nature of the M-Element bond and this, together with studies of compounds designed to model postulated intermediates, allows a better understanding of the above catalytic processes. Base-stabilized complexes of borylene (BR), and silylene (SiR_2) will also be considered as will the possible intermediacy of silylene and stannylene complexes in some reactions. The reactions of BCl_2, $SiCl_3$, and SnI_3 ligands will also be discussed.

Coordinatively unsaturated and saturated boryl, silyl, and stannyl complexes are readily prepared from oxidative addition reactions of B-H, B-B, Si-H, and Sn-H bonds, respectively, to appropriate osmium(0) and osmium(II)

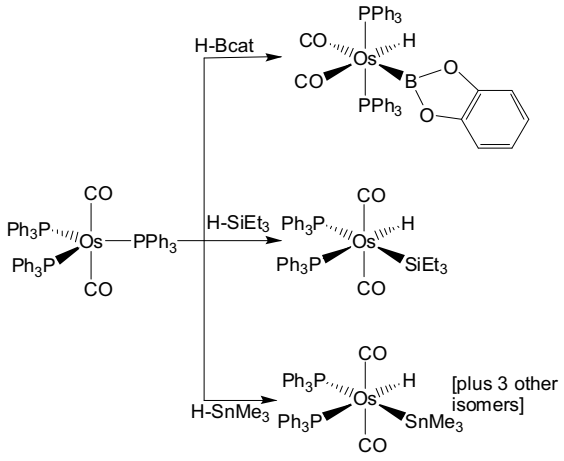

Fig. 1: Synthesis of coordinatively saturated boryl, silyl and stannyl complexes.

complexes. This is illustrated with selected examples in Figures 1 and 2. In the reactions shown in Figure 2 the initial oxidative addition is followed by a reductive elimination of PhH. Crystal structure determinations have shown that all the five-coordinate complexes of type $Os(ER_n)Cl(CO)(PPh_3)_2$ have a tetragonal pyramidal geometry with the ER_n ligand apical and the two triphenylphosphine ligands arranged mutually trans. By using H-BCl_2 it is possible to prepare the novel compound, $Os(BCl_2)Cl(CO)(PPh_3)_2$, where the two B-Cl bonds are usually reactive and some typical derivatives are shown in Figure 3. The spectroscopic and structural data for the set of 3 compounds shown in Figure 3 is good experimental evidence for the significance of the π-component to the Os-B bond. Ethyne inserts into the Ru-B bond in $Ru(Bcat)Cl(CO)(PPh_3)_2$ but not into the Os-B bond in the corresponding osmium compound. The chloride ligand in $Os(Bcat)Cl(CO)(PPh_3)_2$ can be replaced by o-tolyl and in the derived, saturated, compound Os(Bcat)(o-tolyl)$(CO)_2(PPh_3)_2$ there is a very facile reductive elimination of o-tolylBcat.

In some coordinatively saturated chloro, amino-boryl derivatives the B-Cl bond becomes remarkably unreactive. This feature is seen again in SiCl3

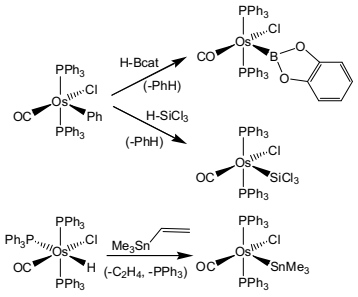

Fig. 2: Synthesis of coordinatively unsaturated boryl, silyl and stannyl complexes.

derivatives described below where the Si-Cl bond becomes unreactive, even to hydroxide under vigorous conditions! The five coordinate $SiCl_3^-$ derivative, $Os(SiCl_3)Cl(CO)(PPh_3)_2$, gives rise to the interesting set of 4 compounds shown in Figure 4 where a combination of spectroscopic, structural, and computational data points to an increasing importance of π-bonding with SiF_3>$SiCl_3$>$Si(OH)_3$>$SiMe_3$. $Os[Si(OH)_3](CO)(PPh_3)_2$ is an especially interesting molecule in that the $Si(OH)_3$ ligand shows little tendency to undergo condensation reactions and in the crystal is not involved in either intra- or inter-molecular hydrogen-bonding interactions. Whereas the 5 coordinate Os(SiCl3)(CO)(PPh3)2 is readily hydrolysed to $Os[Si(OH)_3](CO)(PPh_3)_2$ the 6 coordinate

$Os(SiCl_3)(\kappa^2\text{-}S_2CNMe_2)(CO)(PPh_3)_2$ is quite inert to hydrolysis even when subjected to KOH under vigorous conditions. This inertness of the Si-Cl bond is attributed to a loss of electrophilicity at Si through bonding of the silicon to the very electron-rich osmium centre. Another manifestation of this is that silatranyl derivatives of ruthenium and osmium lose the intramolecular N-Si bond and the N atom in these complexes can be protonated or methylated. The corresponding stannatranyl derivatives provide a striking contrast in that the cage structure is retained with short N-Sn distances.

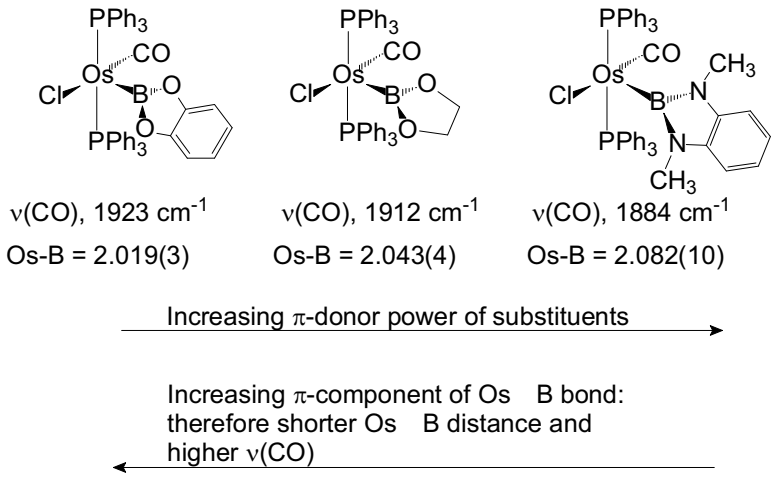

Fig. 3: Spectroscopic and structural evidence for a π-component to the Os–B bond.

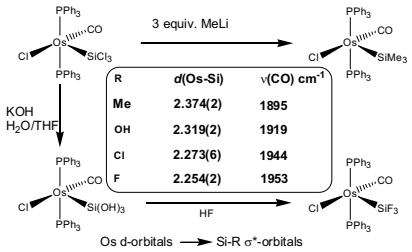

Fig. 4:

Saturated stannyl derivatives can also be made via oxidative addition of Sn-H bonds but the most flexible approach to these compounds is through initial introduction of the trimethylstannyl ligand (as depicted in Figure 2) and subsequent modification of the substituents on tin by making use of redistribution reactions at tin (as depicted in Figure 5). The Sn-X bonds in stannyl ligands do not exhibit the inertness of Si-X bonds in silyl ligands and

$Os(SnI_3)(\kappa^2\text{-}S_2CNMe_2)(CO)(PPh_3)_2$ is easily converted to $Os(SnH_3)(\kappa^2\text{-}S_2CNMe_2)(CO)(PPh_3)_2$. Likewise, $Os(SnMe_2Cl)(\kappa^2\text{-}S_2CNMe_2)(CO)(PPh_3)_2$ reacts readily with $LiSnMe_3$ to form $Os(SnMe_2SnMe_3)(\kappa^2\text{-}S_2CNMe_2)(CO)(PPh_3)_2$ in a novel formation of a distannyl ligand. Another feature of the osmium-

tin complexes is the reversible migration of a methyl group between tin and osmium as shown in Figure 6. The reactions suggest the intermediacy of a transient stannylene complex and further support for this idea is that thermal reactions of $Os(SnMe_3)Cl(CO)(PPh_3)_2$ generate complexes with ortho-stannylated triphenylphosphine complexes.

Acknowledgments I thank my collaborator, James Wright, my colleagues George Clark, Cliff Rickard for crystal structures, and Peter Schwerdtfeger for calculations. I also thank Post-doctoral Fellows and PhD students over several years, too numerous to name here. Financial support has come from the Marsden Fund, The Royal Society (London), The Croucher Foundation, The Humboldt Foundation, and The University of Auckland.

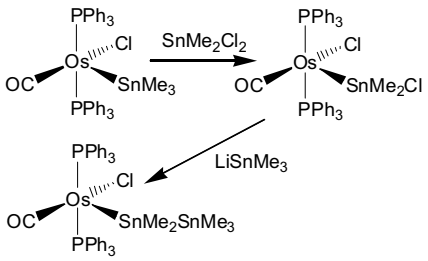

Fig. 5: Synthesis of distannyl complexes

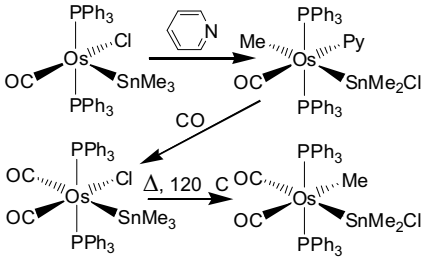

Fig. 6: Reversible methyl migration between Sn and Os.

Theoretical investigations into transition metal-Group 13 element bonding

Penelope J. Brothers

Department of Chemistry, The University of Auckland, New Zealand

Our fundamental understanding of the nature of element-element multiple bonding was initially derived from our knowledge of multiple bonding involving carbon and the other second period elements nitrogen and oxygen. Over the last two decades, as homonuclear element-element bonded compounds involving the heavier main group elements have become experimentally accessible, our understanding of multiple bonding has evolved to become more sophisticated in order to accommodate the different characteristics of these new classes of compounds. In a similar fashion, our knowledge of transition metal-main group element multiple bonding began with a focus on metal-carbon, -nitrogen and -oxygen bonds in carbene, carbyne, imido, nitrido and oxo compounds. It is only much more recently that the corresponding transition metal compounds containing bonds to heavier main group elements have become available, and as a result the nature of the metal-element bonding in these compounds has been subjected to increased scrutiny in recent years. At first this attention was focused on silicon, and to a lesser extent the heavier Group 14 elements, because of their obvious similarity to carbon. However, developments in both synthetic methods and in the use of bulky ligands to

provide steric protection have led to the preparation of a range of compounds with direct transition metal-Group 13 bonds. The specific class of these that are of interest in this study are the transition metal Group 13 diyl compounds L_nM-ER, where E = B, Al, Ga, In and Tl. These are of interest not just for the fundamental questions of bonding and structure, but also because of their potential utility as reagents in important synthetic processes. Borylene complexes, L_nM-BR, have been a target for some time and in the mid 1990s the first examples were reported. This was followed by the report of the iron gallium complex $(CO)_4$FeGaAr* (Ar* is a bulky terphenyl ligand) in which an iron-gallium triple bond was claimed, exciting considerable interest and controversy among both experimental and theoretical chemists.

The key questions concerning the bonding in the L_nM-ER class of compounds centre around the degree of ionic versus covalent character in the M-E bond and the relative contributions of σ bonding and π back-bonding to the M-E bonding. The Group 13 diyl fragments :ER are formally isolobal to a cationic carbyne moiety $:CR^+$ and as such the covalent bonding description comprises σ donation by the lone pair of electrons on E to the $d_z{}^2$ orbital on the metal, and a π back-bonding interaction between filled d_{xz} and d_{yz} orbitals on the transition metal and the p_x and p_y orbitals on E. The ionic and covalent (σ and π) contributions to the bonding will be strongly dependent on the nature of the L_nM fragment, including the characteristics of the auxiliary ligands L_n, and the nature of E. Most of the experimentally reported compounds contain strong π-acceptor ligands, in particular carbonyl (CO) ligands or cyclopentadienyl/carbonyl ligand combinations. This situation has arisen for pragmatic reasons, with the most accessible synthetic routes to L_nM-ER complexes being salt elimination reactions involving the Group 13 dihalides REX_2 with transition metal anions L_nM^{2-} which typically con-

tain strong π-acceptor ligands. The drawback to studying M-E bonding in complexes containing strong π-acceptor ligands is that they will be competing with the Group 13 diyl fragment for available electron density at the metal centre, and may perturb or inhibit the π back-bonding interaction in the M-E bond.

This work concerns a density functional theory study of ruthenium-Group 13 diyl bonding in complexes in which the ancillary ligand on the ruthenium(II) centre is a porphyrin dianion (Por), of the type (Por)Ru-ER. The complete set of Group 13 elements B, Al, Ga, In and Tl was investigated. The porphyrin ligand was chosen because it does not have strong π-acceptor characteristics and ruthenium was selected as the metal because of its higher propensity for π back-bonding relative to first row transition metals. In this system the possibility of Ru-E π back-bonding should be maximised as a result of the characteristics of both the metal and the auxiliary ligand set. Computation was carried out for R = H, and also for R = Trip (where Trip is the bulky aryl ligand $C_6H_2iPr_3$). From a practical point of view, the ruthenium porphyrin dianion $Ru(Por)^{2-}$ is known experimentally and offers the possibility of synthesis of the target complexes through the salt elimination route, and the bulky Trip ligand would be suitable for kinetic stabilisation of the target complexes through steric protection about the Group 13 element centre. The DFT study of the ruthenium porphyrin Group 13 diyl complexes complements other published computational studies which have tended to focus on iron and on complexes containing carbonyl ancillary ligands.

In addition to the computational study on the ruthenium(II) porphyrin complexes (Por)Ru ER, a parallel computational study was undertaken into the ruthenium(0) carbonyl complexes $(CO)_5$Ru-EH. The purpose of this was to investigate the effect of the formal oxidation state at ruthenium, and to

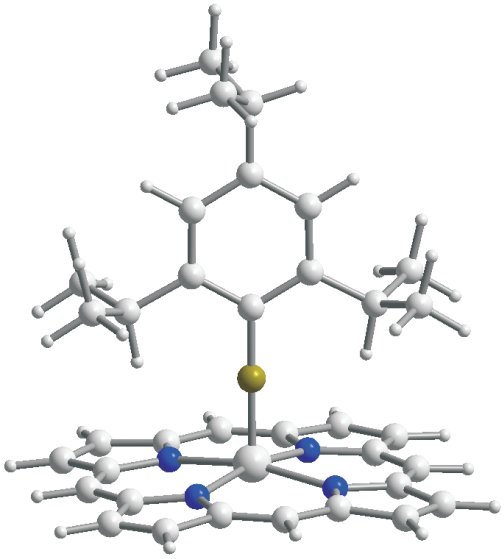

Fig. 1: Optimised B3LYP geometry of (Por)Ru-Btrip

contrast the influence of the porphyrin ligand with the presence of the strong π-acceptor carbonyl ligands.

The results of the study can be summarised as follows. The ruthenium porphyrin complexes have very short Ru-E bond lengths which are calculated to be more than 0.10 Åshorter than those in the corresponding carbonyl complexes. This observation is related to the increased bond strength and higher degree of ionic character in the porphyrin complexes. The bond dissociation energies decrease down the group (B > Al > Ga > In > Tl) within each set of compounds. With the exception of boron, similar bond dissociation energies are calculated for the porphyrin and carbonyl ruthenium complexes. A Natural Bond Order (NBO) analysis indicates that both the σ bonding and π back-bonding characteristics of the Ru-E bond decrease in magnitude on going down the Group 13 elements (B Tl). In the case of boron, the porphyrin compounds (Por)Ru-BR show much higher dissociation energies than

does the carbonyl compound $(CO)_4$Ru-BH, and both the porphyrin and carbonyl ruthenium compounds exhibit the greatest degree of π back-bonding contributions for the borylene complexes.

Acknowledgements

This work was carried out by Dr Tobias Bollwein and Dr Holger L Hermann with the support of Feodor Lynen Fellowships awarded by the Alexander von Humboldt Foundation (Bonn), and with the assistance of Professor Peter Schwerdtfeger. Full results and references to relevant literature can be found in the following paper: "Theoretical investigations into transition metal Group 13 element bonding: comparison between ruthenium porphyrin and ruthenium carbonyl diyl compounds." Bollwein, T.; Brothers, P. J.; Hermann, H. L.; Schwerdtfeger, P. Organometallics 2002, 21, 5236-5242.

Fe, Ru and Ir containing Tin Cluster Compounds

Tilo Söhnel

Department of Chemistry, University of Auckland, Private Bag 92019,
Auckland, New Zealand
Phone: (0064) 9-373 7599 ext. 89722, Fax: (0064) 9-373 7422,
E-mail: t.soehnel@auckland.ac.nz

Abstract

The solid state cluster chemistry of transition metals has been investigated extensively since the middle of last century, starting with the electron poor d-elements of the 4^{th} transition metal group, the group of oxomolybdates and oxoniobates and the electron rich clusters of rhenium sulifdes. Later on, the rare-earth halogenide cluster compounds were discovered, now known in a wide range of different compounds [1]. Only very recently a number of new and very promising intermetalloid clusters like $[Pt@Pb_{12}]^{2-}$ [2] or $[Pd@Bi_{10}]^{4+}$ [3] were found and characterized. Those can be described as endohedral Zintl ions with a binding situation partially comparable to the fullerenes [4]. In comparison to this, condensed oxidic cluster compounds of the main group metals (with the exception of the alkali metal suboxides), are not known. Our research group succeeded to synthesize the first

compound in this series, $Ru_3Sn_{15}O_{14}$, containing condensed Sn_6-octahedra in mixed transition metal-main group metal clusters [5]. Subsequently, a number of new Sn, In and Bi compounds were found, where the metal frameworks are build up of Sn_6-, In_6- and Bi_6-octahedra. In the case of the Sn clusters no other coordination spheres could be found so far. First results have been obtained in the systems M/Sn/O (M = Ru [5], Os [6], Ir [7, 8]), Ru/M/Sn/O (M=Si [9], Al [9], Mn, Fe, Co, Zn, Mg), Fe/Si/Sn/O [10] and Ir/M/Sn/O (M = Fe, Ru) [11]. The central and most striking structural feature of all these stannates are the Sn_6-octahedra, which are filled with the different transition metals. In contrast to the Bi- and In-compounds, where the Bi_6- and In_6-octahedra are isolated from each other, the tin cluster compounds are condensed via common corners and edges of the $[MSn_6]$-octahedra forming one-dimensional endless chains. With the decrease of the transition metal to tin ratio the coordination state of the condensation of the $[MSn_6]$-octahedra increases systematically from compound to compound. The compounds which are not showing the condensation of the $[MSn_6]$-octahedra are $[RuSn_6](Si_{1/4}O_4)_2$, $[RuSn_6](Al_{1/3}O_4)_2$ (Fig. 1), $RuSn_6[(Al_{1/3-x}Si_{3x/4})O_4]_2$, as the mixed crystal of the ternary Si and Al compounds and the recently discovered $[RuSn_6](MO_4)$ (M =Mn, Fe, Co, Zn, Mg) [12], respectively. Here, the isolated [MSn6]-octahedra are only linked together by oxygen atoms and (MO_4)-tetrahedra. An identical or very similar situation can be found in the quaternary and pentanary Pt-In oxides and fluorides $[PtIn_6](GaO_4)_2$, $[PtIn_6](MO_4)(GeO_4)$ (M = Mg, Zn, Fe), $PtIn_7F_{13}$, $Pt_3In_{22}F_{40}$ and $Pt_2In_{14}Ga_3O_8F_{15}$ which have been discovered recently by Köhler et al. [13].

The condensation of the $[MSn_6]$-octahedra has been observed for the first time in the compounds $M_3Sn_{15}O_{14}$ (M = Ru, Os) [5, 6]. Both com-

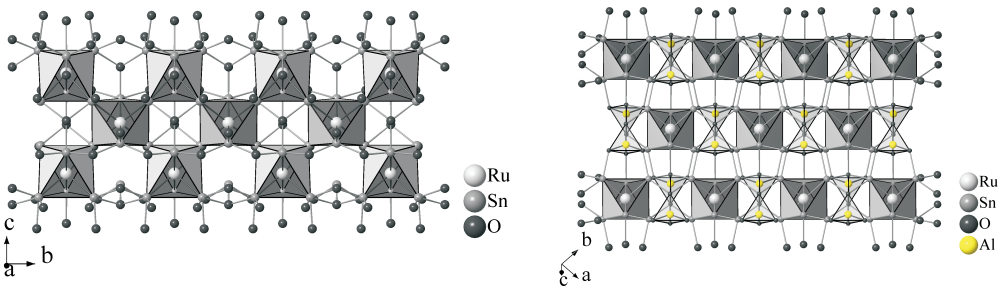

Fig. 1: left: Crystal structure of $Ru_3Sn_{15}O_{14}$; right: Crystal structure of $[RuSn_6](Al_{1/3}O_4)_2$

pounds are characterized by corner-linked $[MSn_6]$-octahedra forming endless one-dimensional triple chains (Fig. 1). With $Ir_{10}Sn_{45}O_{44}$ (Fig. 2) a third compound has been obtained showing the formation of, in this case, endless fivefold chains formed by corner-linked $[IrSn_6]$-octahedra. In all three cases the chains are formed by two outer octahedra and one ($M_3Sn_{15}O_{14}$) or three ($Ir_{10}Sn_{45}O_{44}$) inner octahedra. The outer octahedra are formed by four terminal and two linking tin atoms leading to a composition of $[MSn_4Sn_{2/2}]$ for these octahedra. According to bond length/bond strength considerations the terminal tin atoms can be considered as Sn^{2+}, whereas the linking tin atoms can be estimated as Sn^{1+}. The inner octahedra are formed by two terminal tin atoms and four linking tin atoms leading to the composition of $[MSn_2Sn_{4/2}]$. The amount of oxygen atoms can be obtained from the amount of oxygen atoms, which are connected to the different octahedra. The outer octahedra contain five O-atoms, while the inner octahedra have four O-atoms. In addition, these structures are filled up with one further Sn-atom, which does not belong to the assembly of the chains. From this, the deducible general formula for all compounds can be derived as $[MSn_4Sn_{2/2}]_x[MSn_2Sn_{4/2}]_ySn_zO_{5x+4y}$. While x can only adopt the values of 0 and 2, the number of the inner octahedra (y) is freely selectable. The

amount of the further tin atoms is a result of the difference of all charges:

$$z = \frac{2 \cdot (5x + 4y)x \cdot m + y \cdot n}{2}$$

The charge of the [MSn_6]-octahedra depends on the transition metal placed in the octahedra and will be obtained according to the 18-valence electron rule. In case of $Ru_3Sn_{15}O_{14}$ and $Ir_{10}Sn_{45}O_{44}$ the charges of the Ru and Ir atoms centering the peripheral octahedra are +1 and +2, respectively, whereas the charges for the metals centering the central octahedra are Ru^0 and Ir^{1+}, respectively. Therewith one gets one further Sn^{2+} atom per strand for $Ru_3Sn_{15}O_{14}$ but only 0.5 Sn^{2+} per strand for $Ir_{10}Sn_{45}O_{44}$: $[Ru^{1+}(Sn^{2+})_4(Sn^{1+})_{2/2}]_2[Ru^0(Sn^{2+})_2(Sn^{1+})_{4/2}]_1(Sn^{2+})_1O_{5\cdot2+4\cdot1}$ and $([Ir^{2+}(Sn^{2+})_4(Sn^{1+})_{2/2}]_2[Ir^{1+}(Sn^{2+})_2(Sn^{1+})_{4/2}]_3(Sn^{2+})_{0.5O5\cdot2+4\cdot3})\cdot2$.

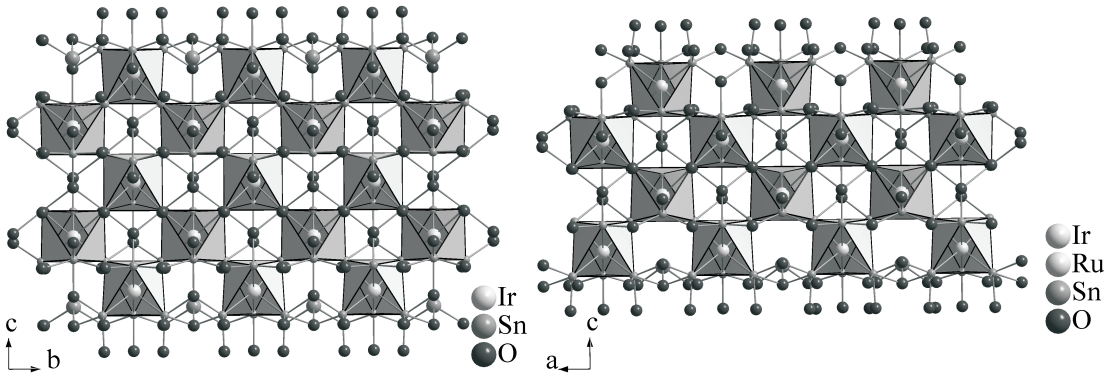

Fig. 2: left: Crystal structure of $Ir_{10}Sn_{45}O_{44}$; right: Crystal structure of $(Ru_2Ir_2)Sn_{19}O_{18}$

The proposed valence states Sn^{2+} and Sn^{1+} can be supported by ^{119}Sn-Mössbauer investigations, which show significantly different signals for the two types of tin atoms. Following this general principle we could postulate a compound containing two inner octahedra and two outer octahedra forming a four-fold chain of corner linked [MSn_6]-octahedra. And indeed, with $(Ru_2Ir_2)Sn_{19}O_{18}$ (Fig. 2) such a compound has been experimentally found

quite recently. An equivalent compound containing only the two outer octahedra (two-fold chain) has not yet been found. A compound, which contains only inner octahedra of type $[MSn_2Sn_{4/2}]$, should have a two-dimensional endless layer of corner-linked $[MSn_6]$-octahedra with the formular MSn_4O_4. The first example for this composition is $IrSn_4O_{4-x}$, but the arrangement of the $[IrSn_2Sn_{4/2}]$-octahedra is not two-dimensional like expected, it is three-dimensional. Higher coordination states are only possible, if an edge- or side-linkage is allowed. The first example of a partly side-linkage is $Ir_3Sn_8O_4$. This compound can be described as a variation of $IrSn_4O_{4-x}$ with additional Ir atoms present. At the same time, only half of the amount of the oxygen atoms of $IrSn_4O_{4-x}$ are existent: $Ir_2Sn_8O_8 + Ir \Longrightarrow Ir_3Sn_8O_4$ (Fig. 3). The original Sn matrix remains, but the structure is slightly distorted (tI $\Longrightarrow$ oI) and a superstructure seems to be formed. X-ray single crystal investigations as well as HRTEM investigations have shown, that a pseudo-orthorhombic superstructure cell with $2a_0 \times 4b_0 \times 2c_0$ is formed and in order to that a distortion of the octahedral chains results. This leads to alternating Ir-Ir-interactions inside the chains, which could be proven by ^{193}Ir-Mössbauer spectroscopy.

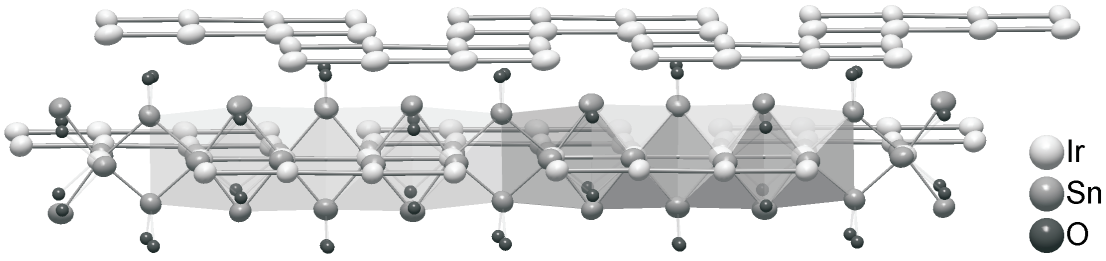

Fig. 3: Crystal structure of $Ir_3Sn_8O_4$

But latest low temperature X-ray investigations at 100 K and 150 K have shown the formation of a monoclinic substructure, which could be solved

and refined easily. The additional superstructure reflexes turned out to be satellite reflexes with a modulation vector H = ha* + kb* + lc* + m(βb* + 1/2c*) (β = 0.239, m = ± 1). The successful refinement of the crystal structure with comprehension of all satellite reflexes was carried out in the (3+1)-dimensional superspace group C2/m(0β1/2)00 as incommensurable modulated structure. The modulation affects all atoms in the unit cell. The strongest modulation could be observed for the Ir atoms, which center the edge-linked octahedra (Fig. 4). The reason therefore is obviously electron excess, which is compensated by the Ir-Ir-interactions inside the chain.

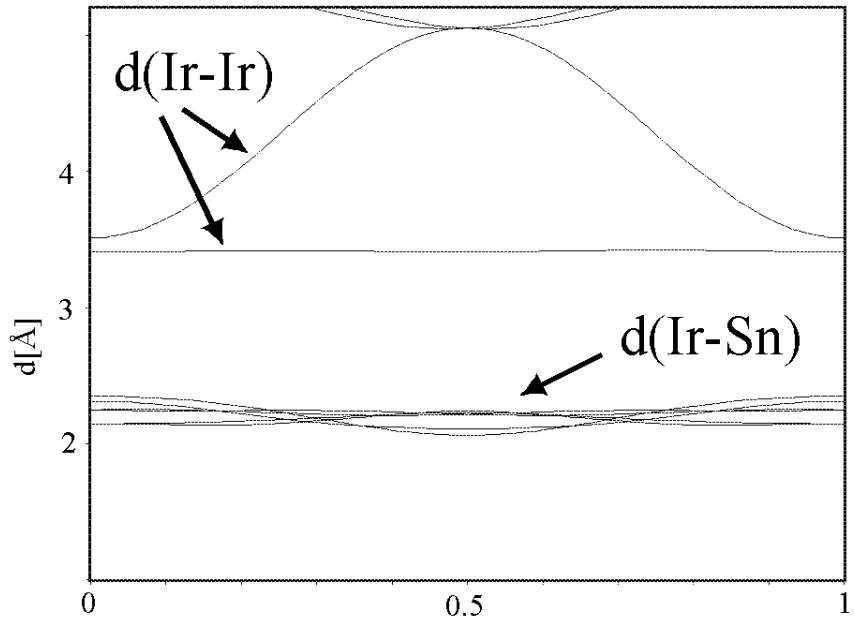

Fig. 4: Variation of the Ir-Ir and Ir-Sn distances in $Ir_3Sn_8O_4$

The ^{193}Ir-Mössbauer spectra have clearly shown the presence of three different coordinated Ir atoms. The Ir atom with the lowest quadrupole split is related to the perpendicular to the chains arranged $IrSn_6$-octahedra. Comparable investigations of other Ir-Sn-O compounds confirm this. Because of the identical Sn-environment of the other Ir atoms, the higher quadrupole

split has to be caused by the Ir-Ir-interactions. The study of the two different quadrupole splits correlates with the formation of four-fold blocs inside the octahedral chains. Thus leads to the formation of a four center-one electron bond, with modulated bond distances. The condensation of the $[MSn_6]$-octahedra results in third type of Sn-atoms in these cluster compounds, which possesses a trigonal-planar coordination of iridium atoms and therefore a very low coordination number for Sn. The formal valence state is assumed to be Sn0. The very unusual oxidation states of Sn^{1+} and Sn^0 could not be observed in oxides up to now. Only in case of SrSnP [14] an Sn1+ has been discussed according to the Zintl-Klemm-concept: $Sr^{2+}Sn^{1+}P^{3-}$. But band structure calculations and ELF-calculations show evidence to suggest, that it should be expected that it is in fact Sn^{2+} [15].

References

[1] Hughbanks T., Corbett J. D. Inorg. Chem. 1989, 28, 631; Payne M. W., Dorhout P. K., Kim S.-J., Hughbanks T. R., Corbett J. D. Inorg. Chem. 1992, 31, 1389; Lulei M., Martin J. D., Hoistad L. M., Corbett J. D. J. Am. Chem. Soc. 1997, 119, 513.

[2] Esenturk E. N., Fettinger J., Lam Y.-F., Eichhorn B. Angew. Chem. 2004, 116, 2184; Angew. Chem. Int. Ed. 2004, 43, 2132.

[3] Ruck M., Dubenskyy V., Söhnel T. Angew. Chem. 2003, 115, 3086; Angew. Chem. Int. Ed. 2003, 42, 2978.

[4] Fässler Th. F., Hoffmann St. D. Angew. Chem. 2004, 116, 6400; Angew. Chem. Int. Ed. 2004, 43, 6242.

[5] Reichelt W., Söhnel T., Rademacher O., Oppermann H., Simon A.,

Köhler J., Mattausch Hj. Angew. Chem. 1995, 107, 2307; Angew. Chem. Int. Ed. 1995, 34, 2113; Söhnel T., Reichelt W., Teske K., Wagner F. E. Z. Anorg. Allg. Chem. 1999, 625, 247.

[6] Söhnel, T., Reichelt W. Acta Crystallog. 1997, C53, 9.

[7] Söhnel T., Reichelt W. Proceedings of the VIIth European Conference on Solid State Chemistry, Madrid, Spain, September 15-18, 1999, p. 203.

[8] Söhnel T. Z. Anorg. Allg. Chem. 2004, 630, 1759.

[9] Söhnel, T., Reichelt, W., Wagner, F. E. Z. Anorg. Allg. Chem. 2000, 626, 223.

[10] Söhnel, T., Böttcher, P., Reichelt, W., Wagner, F. E. Z. Anorg. Allg. Chem. 1998, 624, 708.

[11] Söhnel T., Wagner F. E. Proceedings of the IXth European Conference on Solid State Chemistry, Stuttgart, Germany, September 2-6, 2003, p. 238.

[12] Söhnel T., Kramer M., unpublished results.

[13] Friedrich H., Köhler J. Z. Anorg. Allg. Chem. 2001, 627, 144.; Friedrich H., Köhler J. Proceedings of the VIIth European Conference on Solid State Chemistry, Madrid, Spain, September 15-18, 1999, p. 218; Köhler J., Chang J.-H. Angew. Chem. 2000, 112, 2007; Angew. Chem. Int. Ed. 2000, 39, 1998; Köhler J., Chang J.-H. 5. Jahrestag. DGK, Referateband 1997, 12; Köhler J., Chang J.-H. Whangbo M.-H. J. Am. Chem. Soc. 2005, 127, 2277.

[14] Eisenmann B., Jordan H., Schäfer H. J. Less-Common Met. 1986, 116, 251; Wagner F. R. Ph.D. Thesis, Saarbücken, 1993.

[15] Wagner F. R., Beck H. P. 9th Conference of the GDCh Division for Solid State Chemistry and Material Research, September 23-25, Saarbrücken, Germany, 1998, A55.

Thermodynamic data evaluation for gas phase chemical experiments with transactinides

the experimentalists approach

Robert Eichler[1,2,*]

[1]Laboratory for Radio- and Environmental Chemistry, Paul Scherrer Institute Villigen, CH-5232, Switzerland;

[2]Department for Chemistry and Biochemistry, University Bern, CH-3012, Switzerland;

[*]recently at Lawrence Berkeley National Laboratory, CA 94720, USA

So far, gas phase chemical investigation methods are most successful for the characterization of chemical properties of transactinides. All primary chemical investigations of new transactinide elements (elements 104-108) were performed using gas phase chemistry (see for review [1]). The recent discovery of long-lived isotopes of the heavier transactinides 112 and 114 (see for review [2]) opened up way to their chemical investigation. Recently, gas phase chemical methods are used again to investigate these new elements [3, 4, 5]. For these challenging experimental investigations thermodynamic data evaluation is of exceptional importance for two reasons: 1.) the formulation of expectations for the behavior of the transactinide

elements is essentially during the design phase of the experimental setups; 2.) the evaluation of thermodynamic data from the experimental results allows for assessment of the chemical character of the adsorbing species. A comparison with the predictions formulated in 1.) supports the interpretation of the experimental results. Direct results obtained in experiments with transactinides represent always properties of single atomic species. Those results are dependent on the experimental parameters used. In gas phase chemical studies these primary results are a) the deposition temperature of a species on a defined surface or b) the retention time of a species on a surface kept isothermally, represented by the amount of decay or by the experimental duration for short-lived and long-lived species, respectively. Two linear gas chromatography models are used for the transformation of these single atomic properties into standard adsorption enthalpies at zero surface coverage being comparable independently of the experimental parameters or the setup chosen for their determination. These models are the thermodynamic equilibrium model of mobile adsorption [6] and the microscopic kinetic Monte Carlo model [7]. Meanwhile, at least due to the rapid grow of computational power the Monte-Carlo method is used more or less exclusively for these calculations. It allows for the exact simulation of the real temperature distributions in the chromatographic setups and reproduces the entire shape of a deposition pattern by far better than the mobile adsorption model. Hence, also kinetic adsorption effects (sticking probabilities) leading to tailings of chromatographic depositions can be assessed. The standard adsorption enthalpies represent the energy changes, while a molar amount of the chemical species is transferred from its gaseous state into the adsorbed state at zero surface coverage without changing its chemical composition. The amount of the adsorption enthalpy may give hints regarding the nature of the adsorp-

tive bond. So far, for transactinide atomic and molecular species three types of adsorption bonds have been observed: 1.) a coordinative bond observed e.g. for the adsorption of halides/oxyhalides (group 4-7 of the periodic table) on chlorinated fused silica surfaces or oxides/oxyhydroxides (groups 6-8) on fused silica surfaces, 2.) a weak physisorption bond (groups 8, 12, 14, 18) on metals or fused silica, and 3.) a metal bond for the adsorption of metals on metal surfaces (groups 12-16). The resulting adsorption enthalpies are compared with data obtained using various prediction models. Here, we emphasis classical empirical correlation methods, since other powerful methods, such as density functional approaches are discussed in different other contributions at this workshop.

1 Coordinative adsorption bond.

If the gas phase species (molecule) has coordination vacancies during the adsorption process these vacancies are used to form coordinative adsorption bonds. It can be assumed that the silica surface is modified by the excess of reactive gas admixed to the carrier gas. The molecules approaching the surface form the coordinative bond to the reactive gas molecules on the surface. Hence, a coordination of the central metal atom of the molecule may be created similar to its coordination in the pure solid state phase of the species. The existence of an empirical correlation of the adsorption enthalpies with the sublimation enthalpies (see e.g. Fig. 1) suggests such a similarity of the adsorption and desublimation processes.

Similar empirical correlations were successfully applied for the assessment of collective properties of the heaviest elements and also for the prediction of their adsorption behavior in fused silica columns prior to the experiments:

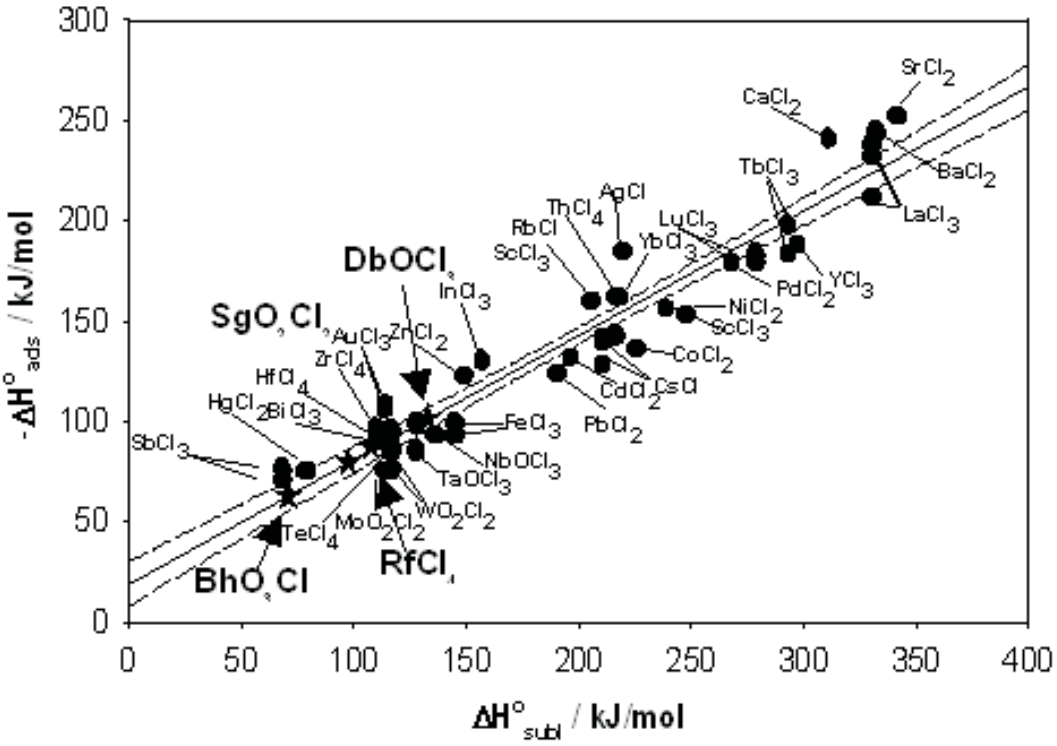

Fig. 1: Correlation of the molecular property adsorption enthalpy ΔH^0_{ads} with the property of the macroscopic solid phase sublimation enthalpy ΔH^0_{subl} for chlorides and oxychlorides in Cl_2, HCl, CCl_4 (O_2).

for elements (with H_2, (H_2O))

$$-\Delta H^0_{ads} = (-9.1 \pm 11.5) + (0.8 \pm 0.1) \cdot \Delta H^0_{subl} \qquad [5]$$

for chlorides and oxychlorides (with Cl_2, $SOCl_2$, HCl, (O_2))

$$-\Delta H^0_{ads} = (21.5 \pm 5.2) + (0.600 \pm 0.025) \cdot \Delta H^0_{subl} \qquad [8]$$

and for oxides and oxyhydroxides (with O2, (H2O))

$$-\Delta H^0_{ads} = (6.27 \pm 7.78) + (0.680 \pm 0.028) \cdot \Delta H^0_{subl} \qquad [9]$$

This type of correlations still represents the only link available between microscopic properties of "carrier free" amounts of d-element compounds

and properties of macroscopic amounts. These correlations offer direct access to the enthalpy of sublimation from the experimental result. ΔH^0_{subl} is considered as the measure for the volatility of a species. It represents the energy equivalent needed to transform a molar amount of the species from its solid state into its gaseous state. The use of vapor pressure, for example, suffers from uncertainties in its entropic part, strongly dependent on the molecular structure change during the transformation of the solid phase into the gaseous state. Hence, no correlation is observed between the vapor pressure and the adsorption enthalpy. However, speaking about volatilities as a result of adsorption chromatography experiments one has always to assure the validity of correlations shown above. The deduced volatility of a species allows further for estimation of more basic thermochemical data for the chemical species. One impressive example is the observed correlation between the standard formation enthalpies of gaseous and solid oxychlorides and oxyhydroxides (see Figure 2).

With just the volatility (sublimation enthalpy) it is possible to estimate basic thermodynamic data for the solid and the gaseous state. So far, this is the only example where the solid state property of a transactinide species can be derived.

$$-\Delta H^0_{298}(s) = a \cdot (-\Delta H^0_{298}(g)) + b \longrightarrow \quad \Delta H^0_{298}(g) = \frac{b - \Delta H^0_{subl}}{a-1}$$
$$\Delta H^0_{298}(s) = \frac{a \cdot \Delta H^0_{subl} - b}{1-a}$$
$$a = 1.449 \pm 0.034, b = -182.9 \pm 24.9$$

2 Physisorptive adsorption

In case of inert gases the interaction between an atom A and the surface B depends mainly on the polarizability and size of the atoms A. Here, the simplest approach is the well known formula for the calculation of the dispersion

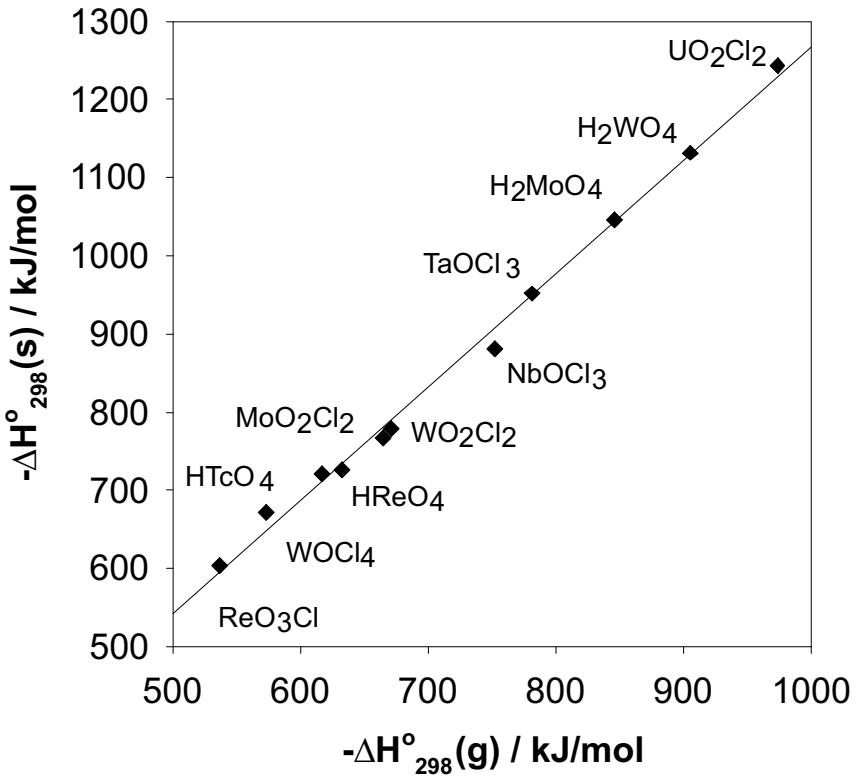

Fig. 2: Correlation of the standard formation enthalpies of oxychlorides and oxyhydroxides in their gaseous ($\Delta H^0_{298}(g)$) and solid state ($\Delta H^0_{298}(s)$)

binding energy (EDB) in the physisorptive case.

$$E_{DB} = -g \cdot \frac{E_a \cdot E_B}{E_A + E_B} \cdot \frac{\alpha}{8 \cdot r_e^3}$$

$E_{A/B}$ ... effective excitation energy $\longrightarrow E_{A/B} = 1.57 \cdot IP_{A/B}$; g = 1 for metals;

α ... polarizability of the adsorbate; $IP_{A/B}$ ... ionisation potentials;

r_e ... distance between the adsorbate to the substrate;

However, a comparison with experimental data yielded insufficient results not even describing the trend in the interaction e.g. of radon with various metals [10]. The main uncertainties rise from the unknown distances between the adsorbate atoms and the surface re (third power, see above).

Another approach was suggested by Miedema and Nieuwenhuys [11]. They describe the adsorption interaction of noble gases with metals in the form of energy of adhesion. Several data are required for the metal: the electron density at the Wigner-Seitz cell boundaries, the surface energies at 0K, and the atomic volume of the pure metals. So far, the electron density at the Wigner-Seitz cell boundaries is calculated by summation of electron densities of each electron orbital of the single atoms at a distance of a Wigner-Seitz radius from the nucleus. This is a very rough approach. A more exact method would be a calculation of the quantities such as the electron density at the Wigner-Seitz cell boundaries or the atomic volumina using ab-initio calculation methods assuming metal lattices with high coordination numbers (12) for all transactinide elements.

Moreover, in addition to the good agreement of the results of this approach with experimental results, correlations between the adsorption enthalpies of the inert gases Ne, Ar, and Kr on metals and the adsorption enthalpies of xenon on these metals were observed.

$$\Delta H_{ads}(Z, M) = C(Z, Xe) \cdot \Delta H_{ads}(Xe, M)$$

Using empirical correlations for example between the C(Z,Xe) and the polarizabilities or the ionization potentials corresponding proportionality constants C(Z,Xe) for Rn and the hypothetical noble gas like elements 112 and 114 were derived [10]. Hence, simply from the adsorption enthalpy of Xe on the metal surface of interest one can predict the amount of adsorption interaction for other inert gases or inert gas like elements. Fig. 3 depicts the comparison between experimental and calculated data for radon adsorption.

3 Metal-Metal interaction

Already in the 1970s it was suggested that the investigation of the adsorption properties of transactinide s- and p-elements of the groups 12-16 in the periodic table on metal surfaces may reveal their metallic character [12]. Nowadays, with the observation of long-lived isotopes of the elements 112 and 114 this suggestion is turned into experimental practice.

An exceptionally useful quantification of metal-metal interactions is provided by a model suggested by Miedema [13, 14]. This macroscopic semiempirical description of the thermodynamics of intermetallic alloys reproduces very well experimental results obtained for hundreds of metallic binary liquid and solid systems. Later on an extension of the Miedema model for the description of adsorption interactions was made [15]. Here the

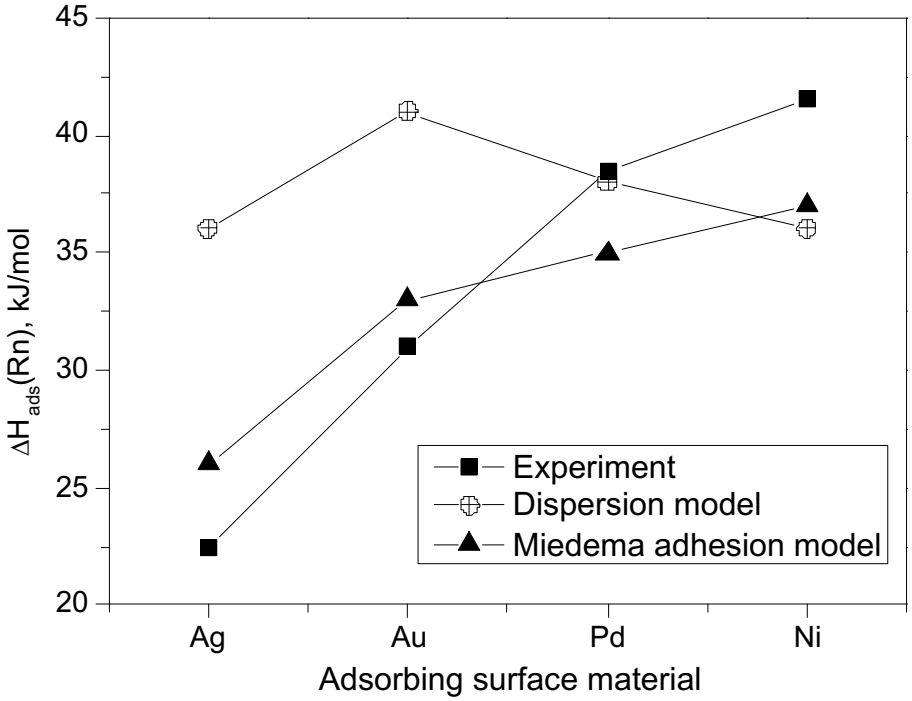

Fig. 3: Comparison beween the experimental results for the adsorption of Rn on various metals and calculated data.

adsorption enthalpy of a metal A on a metal B is described by two terms: 1) the transformation of the gas phase species A into a solid solution with B at infinite dilution and 2) the subsequent segregation of A to the surface of B. Hence the adsorption enthalpy can be derived by a Born-Haber cycle as a linear combination of the differential partial enthalpy of solid solution (ΔH_{sol}), the enthalpy of segregation (ΔH_{segr}), and the enthalpy of desublimation ($-\Delta H^0_{subl}$).:

$$\Delta H_{ads} = -\Delta H_{subl} + \Delta H_{sol} + \Delta H_{segr}$$

Again parameters of the pure metals are needed for the calculation of ?Hsol: the atomic volume, the electron density at the Wigner-Seitz cell boundaries in their pure metallic state, the atomic volumes, the enthalpies of surface and volume vacancy formation of the surface metal, and the sublimation enthalpy. So far, most of these data were predicted by empirical correlation methods [12, 16, 17].

Recently, a new empirical correlation of the adsorption enthalpies of a variety of elements beginning from metals like lead and bismuth up to noble gases on gold surfaces

with their sublimation enthalpies was established to serve both, for the evaluation of thermodynamic data from experimental results as well as for the formulation of expectations from predicted thermodynamic data for the heaviest elements [18].

The results of these calculations for the new transactinide p-elements enforce the experimentalists to think about the design of new gas phase chemical setups in order to study less volatile atomic species as well as extremely volatile elements. So far, the limitations of the on-line thermochromatographic investigation setups are given by the operational temperature range specified for the solid state silicon based detectors (50°C - –200°C). Moreover, contaminations covering the metal surface at the lowest temperatures (e.g. ice) as well as oxidation processes of the stationary chromatographic metal surface at higher temperatures severely interfere the adsorption information or render strong limitations regarding the selection of the proper chromatographic stationary material [5, 10, 19]. Most of these contaminations originate from the chromatographic carrier gas. Therefore, preparations are made to investigate the adsorption of single atomic species under vacuum conditions. It is expected that adsorption processes under vacuum conditions can be studied in a wide temperature range from 600°C down to –200°C without surface contaminations. The first design plans of such experimental setups will be presented as well as appearing requirements for new thermodynamic data, such as release enthalpies and diffusion coefficients.

References

[1] Chemistry of Superheavy Elements, ed. M. Schädel, Kluwer Academic Publishers (2003).

[2] Oganessian, Yu. Ts. et al.: Phys. Rev. C 70, 064609 (2004).

[3] Yakushev, A.B. et al.: Radiochim. Acta 89(11-12), 743 (2001).

[4] Yakushev, A.B. et al.: Radiochim. Acta 91, 433 (2003).

[5] Soverna, S., PhD-Doctoral thesis, University Bern, Bern, Switzerland (2004).

[6] Eichler, B., Zvara, I.: Radiochim. Acta 30, 233 (1982).

[7] Zvara, I., Radiochim. Acta 38, 95 (1985).

[8] Eichler, B. et al.: J. Phys. Chem. A 103(46), 9296 (1999).

[9] Eichler, R. et al.: Radiochim. Acta 87, 151 (1999).

[10] Eichler, R., Schädel, M.: J. Phys.Chem. B106, 5413 (2002).

[11] Miedema, A.R., Nieuwenhuys, B.E.: Surf. Sci. 104, 491 (1981).

[12] Eichler, B.: Kernenergie 19, 307 (1976).

[13] Miedema, A.R.: J. Less-Common Met. 32, 117 (1973).

[14] Miedema, A.R.: J. Less-Common Met. 46, 67 (1976).

[15] Eichler, B., Rossbach, H.: Radiochim. Acta 33, 121 (1983).

[16] Eichler B.: PSI Report 00-09; Villigen (2000), ISSN 1019-0643.

[17] Eichler B.: PSI Report 03-01; Villigen (2002), ISSN 1019-0643.

[18] Eichler, R.: Radiochim. Acta 93, 245 (2005).

[19] Soverna, S. et al.: Radiochim. Acta 93, 1 (2005).

Carbon monoxide reaction with UO_2 (111) single crystal and thin film surfaces.

*S.D. Senanayake, G.I.N. Waterhouse and H. Idriss**

The Department of Chemistry, The University of Auckland, Private Bag 92019, Auckland, New Zealand

Corresponding author: Fax: 74 9 373 7422, email: h.idriss@auckland.ac.nz

Abstract

The reaction of carbon monoxide has been investigated on the surfaces of UO2(111) single crystal and thin film. Over the stoichiometric surfaces CO is very weakly adsorbed with no further reaction noticed. Over UO_{2-x}, CO molecules adsorb and in presence of traces of H2 they couple to make acetylene molecules that desorb in two temperature domains during TPD. In the presence of excess H_2 the coupling product is seen to be ethylene. High Resolution X-ray Photoelectron Spectroscopy (HRXPS) of the core level of the oxygen-defected surface shows the presence of U4f lines attributed to multiple oxidation states. The lines attributed to U^{x+} ($x < 4$) decrease upon CO adsorption; indicating oxidation by O atoms from dissociatively adsorbed CO molecules. XPS C1s lines shows the presence of adsorbed species tentatively assigned to enolate species that are most likely the reaction intermediate in the coupling of two CO molecules to acetylene.

1 Introduction

The surface chemistry of the uranium oxide system is very rich. The fact that uranium ions can accommodate several coordination numbers and several oxidation states makes them active for oxidation/reduction reactions. CO reactions, over oxide surfaces, have been studied in details for long years. The most common chemical reaction studied for CO is its oxidation to CO_2, in that regard U_3O_8 is a very active catalytic material, far superior to most early transition metal oxides[1, 2]. Far less work has been done for the reduction (including coupling) of CO on oxides. Although no surface science work has addressed the coupling of CO molecules to higher hydrocarbons yet, examples of coupling of CO in coordination chemistry are common. On U complexes coupling of two molecules of CO to enolates has been reported a while ago[3]. Other metals, such as V, Mo and W[4], are also active for this reaction. In this work we show that one can selectively make C_2H_2 from CO and H_2 over the surface of UO_{2-x} (111) single crystal. The oxidation/reduction of UO_{2-x} was followed by the U and O core levels while the reaction products were monitored by TPD.

2 Experimental

TPD experiments was conducted in an Ultra High Vacuum (pressure $\approx$ 1x10^{-10} torr) stainless steel chamber equipped with several surface science techniques, as described elsewhere, at the University of Auckland [5]. HRXPS is conducted at U12a beamline at the National synchrotron Light Source of Brookhaven National Laboratory. The UO_2(111) single crystal surface was prepared prior to all experimentation with several cycles of annealing to 800K and Ar^+ sputtering, and further confirmed for stoichiometry (or near stoichiometry) using XPS and Low Energy Electron Diffraction (LEED) with a sharp hexagonal structure (figure 1). The UO_2 thin film was cleaned using a similar method but with annealing temperatures not exceeding 600 K to maintain the integrity of the thin film. The defected surfaces (UO_{2-x}) is obtained with extended periods of Ar^+ sputtering and analysed by XPS.

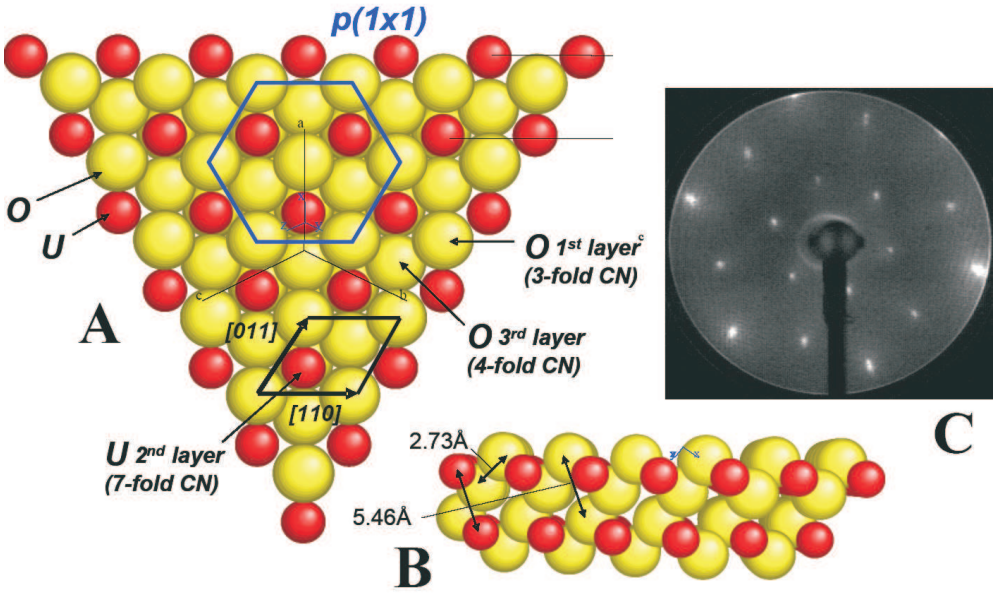

Fig. 1: Ball model of the UO_2(111) surface showing the hexagonal arrangement of U and O atoms and lattice parameters; red balls U atoms, yellow balls O atoms (**A**: top view, **B**: side view) **C**: LEED of the UO_2(111) surface showing the extended order (131 ev)

3 Results

3.1 Temperature Programmed Desorption of CO

Figure 2 shows TPD following CO adsorption (9 L exposure; 1 L = 10^{-6} torr s) at 300 K over a UO_{2-x} surface (x is estimated from XPS O1s/U4f lines to be equal to 0.3). The striking result is the formation of acetylene that is due to coupling of two molecules of CO and their association with the inevitable traces of H_2 in the background of the chamber (as well as during sputtering). In addition, considerable amounts of CO_2 are formed. Repeating the CO-TPD experiments after different sputtering time shows that the amount of CO_2 increases with increasing reduction, while the yield for C_2H_2 remains constant (within few %), figure 3. This result may indicate an additional route for CO reaction (beside the coupling to acetylene) on defected surfaces; Boudouard reaction (2 CO (a) $\longrightarrow$ CO_2 (g) + C(a); (a) for adsorbed, (g) for gas) is a likely pathway.

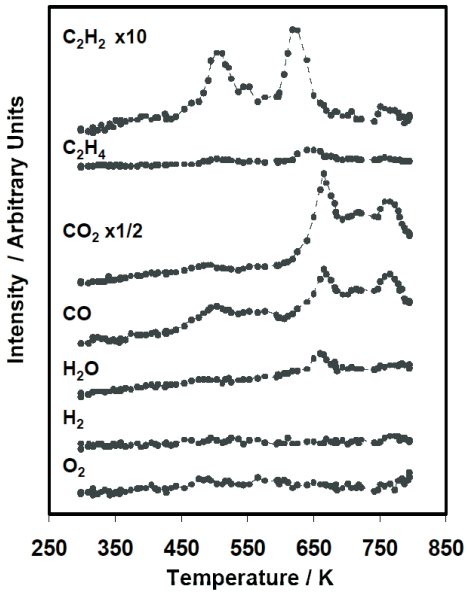

Fig. 2: TPD following CO adsorptions on UO_{2-x} ($x \approx 0.3$). Note the small desorption of H_2O and the absence of CO_2 desorption.

3.2 XPS after CO adsorption at 300 K

Figure 4 shows HRXP spectra of the U4f region before and after exposure to CO at 300 K. Spectrum **a** is that of the freshly sputtered surface before adsorption. In addition to the $U4f_{7/2}$ and $U4_{5/2}$ lines at 380 and 391 eV, respectively and attributed to U^{4+}, a clear line at 377 eV is seen. This latter line is a complex region containing several oxidation states of U atoms including U metal. Upon adsorption of CO the intensity of these lines decrease and almost disappear at surface saturation. Figure 5 shows the corresponding HRXPS C1s lines A main feature at a binding energy of 286.5 eV is seen. Parallel study of ethylene glycol (EG), $HOCH_2CH_2OH$, adsorption on the surface of stoichiometric UO_2 thin film reveals lines very similar to those in figure 5. Since EG is most likely dissociatively adsorbed on the surface its C1s line position should be very close the endiolate species presented at the top of figure 5.

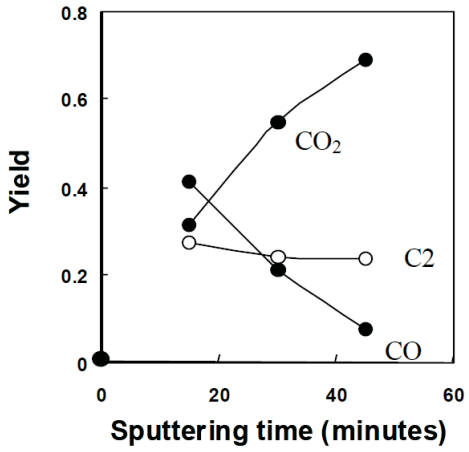

Fig. 3: CO-TPD yield from UO_2/UO_{2-x} surface as a function of extent of reduction. At zero sputtering time no reaction is taking place.

4 Discussion

The formation of C_2H_2 from CO can be represented by several chemical equation the most realistic of them are the following two:

$$4CO + H_2 \longrightarrow C_2H_2 + 2CO_2 \qquad \Delta G = -29\text{kJ} \cdot \text{mol}^{-1} \tag{30}$$

$$2CO + 3H_2 \longrightarrow C_2H_2 + 2H_2O \qquad \Delta G = +28\text{kJ} \cdot \text{mol}^{-1} \tag{31}$$

Clearly ΔG favours equation 30. In addition, considerable amount of CO_2 is seen during TPD while only traces of H_2O desorbed. It is however not clear if all CO_2 is formed from CO coupling, some might be due to CO oxidation with loosely bonded lattice O atoms formed upon sputtering. CO_2 can also be formed from CO following Boudouard reaction and this may explain the increase of CO_2 yield with increasing sputtering time (increasing the amount of U metals on the surface) as seen in figure 3. Acetylene synthesis is most likely via a pinacol route (coupling reaction as seen in organometallic U and Th compounds[3].

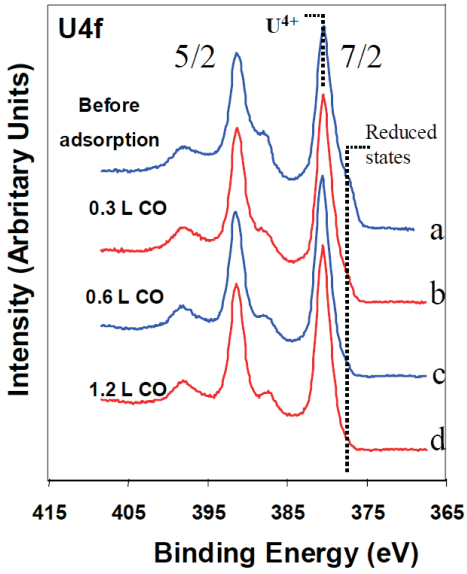

Fig. 4: HRXPS U4f lines of Ar-ion sputtered UO_2 thin film before (a) and after (b,c and d) reaction with CO at the indicated exposures in Langmuir (L).

5 CONCLUSIONS

The rich chemistry of uranium oxide system can serve as a model for studying chemical reactions in general and coupling reactions in particular. The work shows that while stoichiometric UO_2(111) single crystal is inactive for CO coupling, the oxygen defected one is active for the coupling of CO molecules to acetylene and ethylene.

References

[1] F. Nozaki and K. Ohki, Bull. Chem. Soc. Japan **45**, 3473 (1972)

[2] G. Hutchings, C.S. Heneghan, I.D. Hudson and S.H. Taylor, Nature **384**, 341 (1996)

[3] B. E. Kahn and R. D. Rieke, Chem. Rev. **88**, 733 (1988) and references therein.

[4] E. M. Carnahan, J.D. Protasiewicz and S. J. Lippard, Acc. Chem. Res. **26**, 90 (1993)

[5] S. D. Senanayake, H. Idriss, Surf. Sci. **563**, 135 (2004)

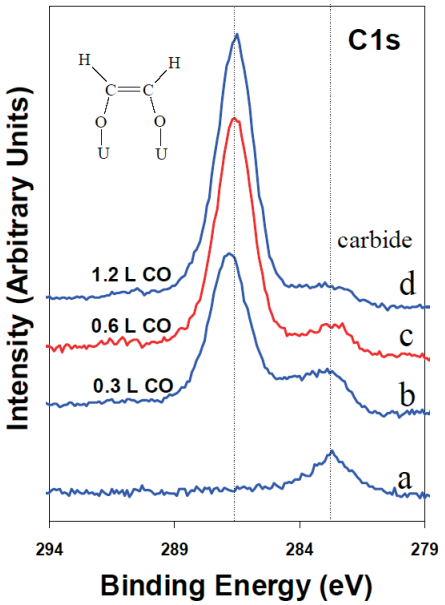

Fig. 5: HRXPS C1s lines of Ar-ion sputtered UO_2 thin film before (a) and after (b,c and d) reaction with CO at the indicated exposures in Langmuir (L).

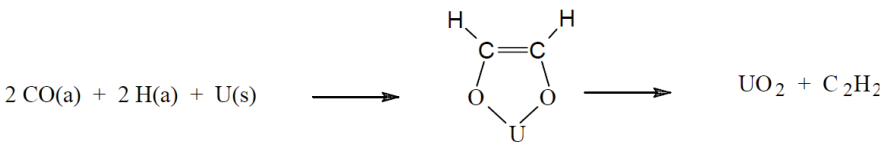

Solid-State NMR of Silver and Mercury Compounds

Graham A. Bowmaker[1], Robin K. Harris[2], Behnam Assadollahzadeh[3], David C. Apperley[2], Paul Hodgkinson[2], Pornsawan Amornsakchai[2], Andrew M. Brodie[3], Eric W. Ainscough[3], Graham H. Freeman[3] and Geoffrey B. Jameson[3]*

[1]Department of Chemistry, University of Auckland, Private Bag 92019, Auckland, New Zealand;

[2]Department of Chemistry, University of Durham, South Road, Durham DH1 3LE, United Kingdom;

[3]Chemistry - Institute of Fundamental Sciences, Massey University, Palmerston North, Private Bag 11 222, Palmerston North, New Zealand.

Solid-state cross-polarisation magic-angle spinning (CP-MAS) NMR spectra have been recorded for the compounds $[Ag(NH_3)_2]_2SO_4$, $[Ag(NH_3)_2]_2SeO_4$ and $[Ag(NH_3)_2]NO_3$, all of which contain the linear or nearly linear two-coordinate $[Ag(NH_3)_2]^+$ ion[1]. The ^{109}Ag CP-MAS NMR spectra show centrebands and associated spinning sideband manifolds typical for systems with moderately large shielding anisotropy, and splitting due to indirect ^{1}J(^{109}Ag-^{14}N) spin-spin coupling (Fig. 1).

Spinning sideband analysis has been used to determine the ^{109}Ag shielding anisotropy and asymmetry parameters .s and . from these spectra, yielding anisotropies in the range 1500-1600 ppm, and asymmetry parameters in the range 0 - 0.3. One-bond (Ag, ^{15}N) coupling constants are found to have magnitudes in the range 60 65 Hz. Density functional calculations of the Ag shielding tensor for model systems yield results that are in good

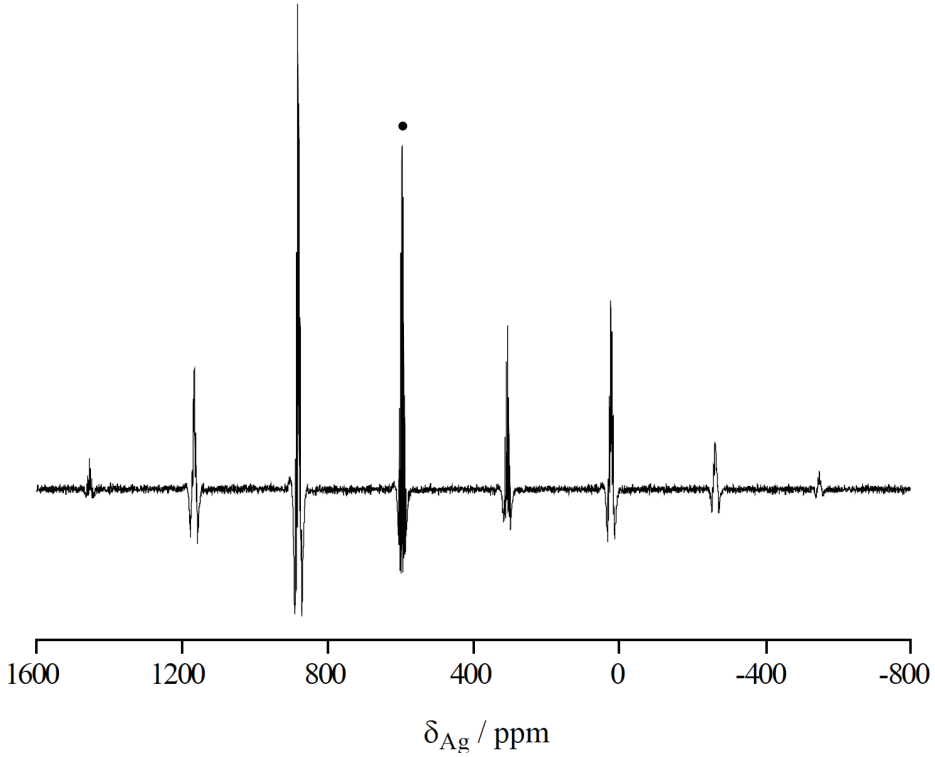

Fig. 1: ^{109}Ag CP-MASN NMR spectrum of $[Ag(NH_3)_2]_2SeO_4$, obtained at 13.97 MHz and with spinning at 4 kHz. The centreband is indicated by ·

agreement with the experimentally determined shielding parameters, and suggest that in the solid compounds $\delta\sigma$ and η are reduced and increased respectively from the values calculated for the free $[Ag(NH_3)_2]^+$ ion (1920 ppm and 0 respectively), primarily as a result of cation-cation interactions for which there is evidence from the presence of metal-over-metal stacks of $[Ag(NH_3)_2]^+$ ions in the solid-state structures of these compounds. The tribenzylphosphine (PBz_3) complexes of mercury(II), $[Hg(PBz_3)_2](BF_4)_2$, $[Hg(PBz_3)_2(NO_3)_2]$ and $[HgX(NO_3)(PBz_3)]$ (X=Cl, Br, I and SCN), have been synthesised and their structures characterized by single-crystal X-ray crystallography and CP-MAS NMR spectroscopy.[2] $[Hg(PBz_3)_2](BF_4)_2$ contains $[Hg(PBz_3)_2]^{2+}$ cations with linear P-Hg-P coordination, the first example of a truly two-coordinate $[Hg(PR_3)_2]^{2+}$ complex (Fig. 2).

The mercury coordination in $[Hg(PBz_3)_2(NO_3)_2]$ can be described as distorted tetrahedral, with a significant deviation of the P-Hg-P angle from linearity as a result of coordination of the nitrate groups. Nitrate coordination is also observed in $[HgX(NO_3)(PBz_3)]$

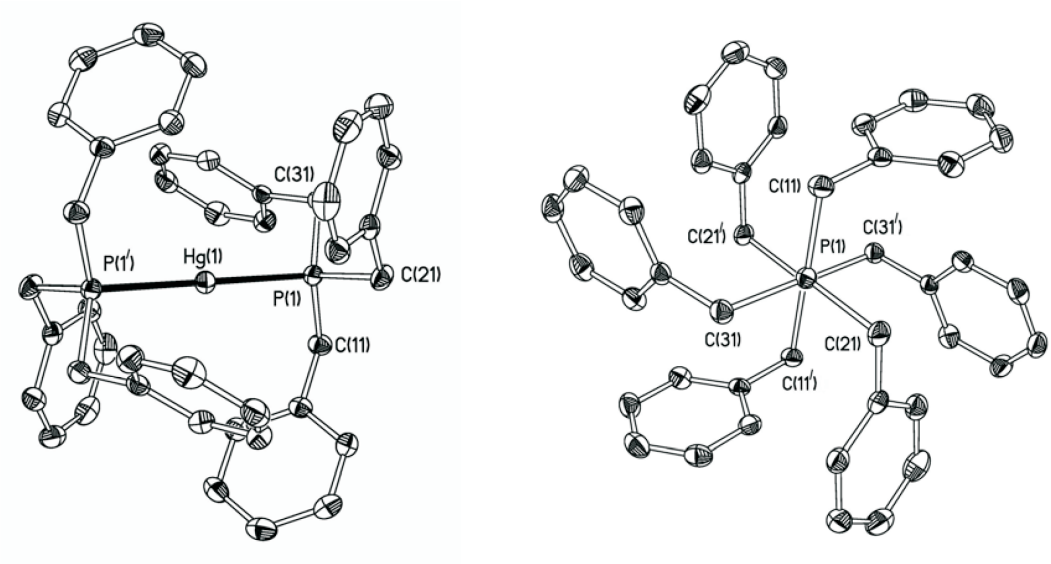

Fig. 2: The $[Hg(PBz_3)_2]^{2+}$ cation in $[Hg(PBz_3)_2](BF_4)_2$ (ellipsoids are drawn at the 50% probability level).

(X = Cl, Br, I), resulting in significantly non-linear P-Hg-X coordination. The thiocyanate complex is a centrosymmetric thiocyanate-bridged dimer with distorted trigonalpyramidal mercury coordination to the P atom of PBz3, to the S and N atoms of two bridging thiocyanate groups, and to the O atom of one nitrate group. For all the nitrato complexes, secondary mercury-nitrate interactions (Hg-O 2.7 3.1 Å) effectively raise the coordination number of the Hg(II) centres to six. High-resolution ^{31}P solid-state CPMAS NMR spectra of the six tribenzylphosphine mercury(II)-complexes have been recorded. The spectra of $[Hg(PBz_3)_2](BF_4)_2$ and $[HgX(NO_3)(PBz_3)]$ (X = Cl, Br, I and SCN) exhibit a single line, due to species that contain non-magnetic isotopes of mercury, and satellite lines, due to $^1J(^{31}P\text{-}^{199}Hg)$ coupling (Fig. 3).

The asymmetric unit of $[Hg(PBz_3)_2(NO_3)_2]$ contains two molecules with four phosphorus environments, resulting in two AB spectra with $^2J(^{31}P\text{-}^{31}P)$ coupling, due to species that contain non-magnetic isotopes of mercury, and satellite lines consisting of two ABX spectra, due to $^1J(^{31}P\text{-}^{199}Hg)$ coupling (Fig. 4).

These spectra have been analysed to yield all of the chemical shifts and coupling contants involved. A remarkable increase in $^1J(^{31}P\text{-}^{199}Hg)$ is observed from $[Hg(PBz_3)_2](BF_4)_2$ to $[Hg(PBz_3)_2(NO_3)_2]$ as a consequence of the incorporation of the nitrate group into the

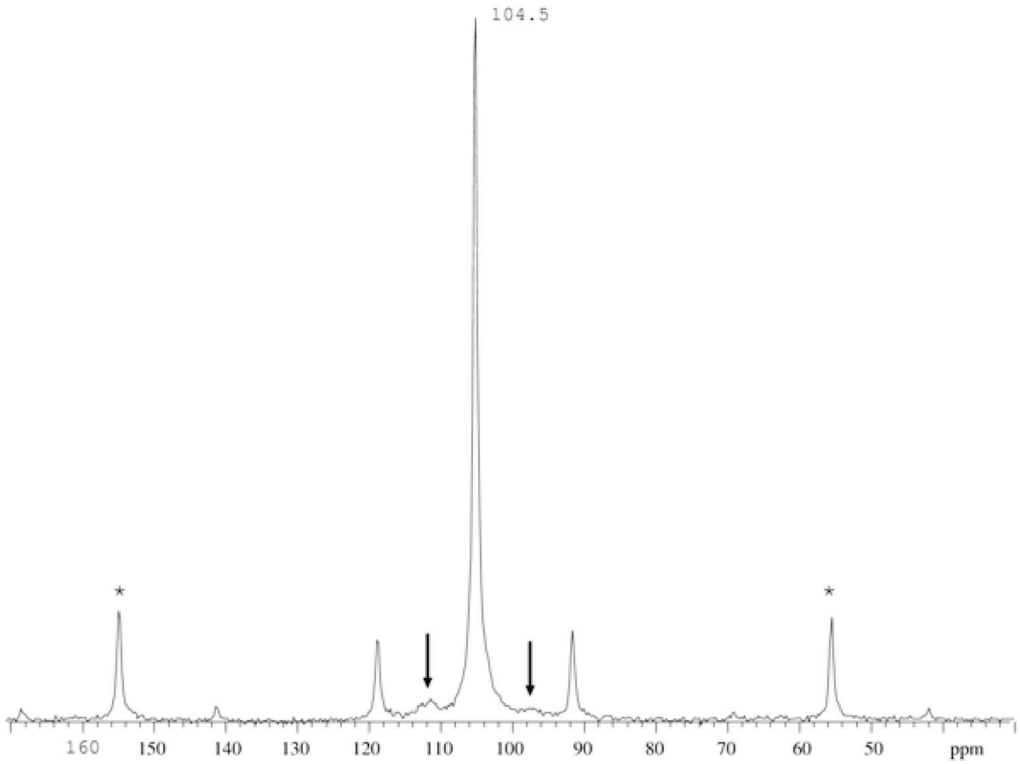

Fig. 3: ^{31}P CP-MAS NMR of $[Hg(PBz_3)_2](BF_4)_2$, at a rotor spinning rate of 6 kHz. Spinning sidebands are marked with asterisks. $\downarrow$ = peaks assigned as ^{201}Hg satellites.

Hg coordination sphere in the latter case. Several of the spectra also exhibit broader satellites due to the presence of scalar spin-spin coupling between ^{31}P and the quadrupolar ^{201}Hg nucleus (Fig. 3). Slow-spinning methods have been used to analyze the spinning-sideband intensities of the NMR spectra, in order to obtain the ^{31}P shielding anisotropy and asymmetry parameters $\delta\sigma$ and η The ^{199}Hg and ^{31}P NMR shielding tensors of PMe_3 models of the above six compounds have been calculated using relativistic density functional theory. The ^{31}P results are in good agreement with experiment and assist in the assignment of some of the signals.

Comparison of the results of the silver and mercury studies shows a significant difference in the effects of intermolecular interactions on the NMR parameters. In the case of the silver(I) compounds, the major effects result from an interaction between the cationic silver complexes. In the case of the mercury(II) compounds, the major effects result from

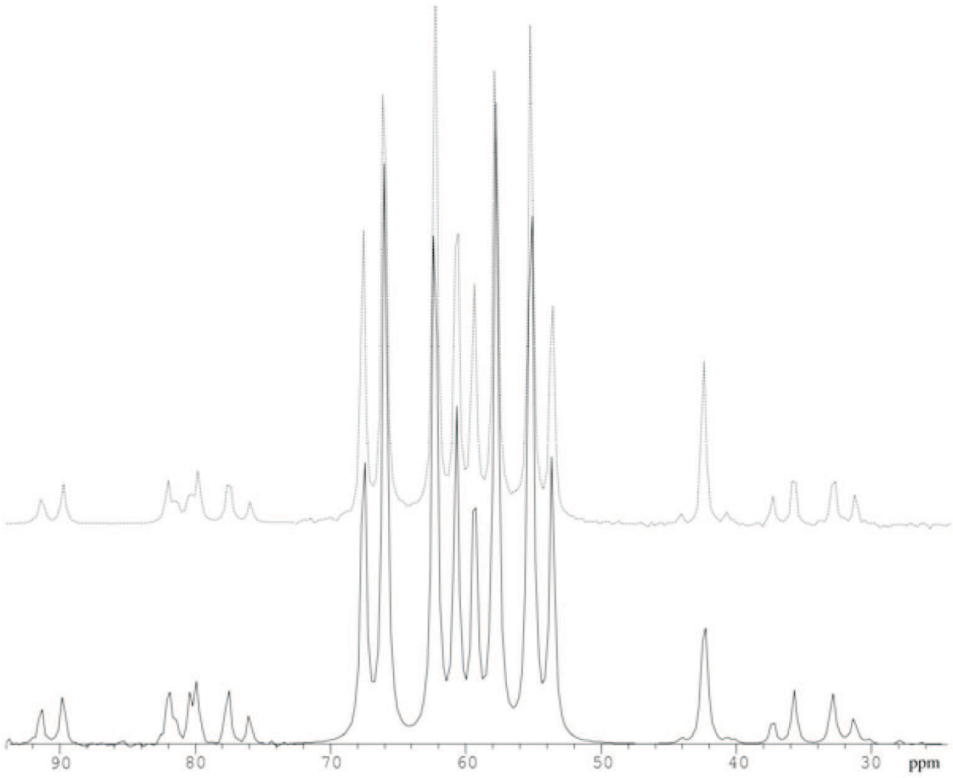

Fig. 4: Simulated (upper) and experimental (lower) ^{31}P CP-MAS NMR of $[Hg(PBz_3)_2(NO_3)_2]$, at a rotor spinning rate of 6 kHz.

cation-anion interactions.

References

[1] Bowmaker, G.A., Harris, R.K., Assadollahzadeh, B., Apperley, D.C., Hodgkinson, P., Amornsakchai, P., "Solid-State ^{109}Ag CP-MAS NMR Spectroscopy of some Diammine Silver(I) Complexes", Magnetic Resonance in Chemistry, 2004, 42, 819-826.

[2] Bowmaker, G.A., Assadollahzadeh, B., Brodie, A.M., Ainscough, E.W., Freeman, G.H. Jameson, G.B., "Structural and Spectroscopic Studies on Mercury(II) Tribenzylphosphine Complexes", Dalton Transactions, 2005, 1602-1612.

Tethered osmabenzenes derived from an osmabenzofuran

L. J. Wright

Department of Chemistry, The University of Auckland, New Zealand

Benzene is the archetypical aromatic compound. It is a cyclic, planar molecule with a delocalised π-bonding system that obeys Hückel's $(4n+2)$ rule. The characteristic physical properties that have come to be associated with aromaticity are displayed by benzene. These include high thermodynamic stability, bond length equalization around the ring, and the effects of ring current effects on 1H NMR chemical shifts.

Stable, aromatic, heterocyclic analogues of benzene in which one of the CH groups is formally replaced by a main group element such as N (to give pyridine), P (to give phosphabenzene), RSi (to give silabenzenes) are also well known. Recently it has been shown that the formal replacement of a CH group in benzene by a transition metal and its ancillary ligands is also possible and the resulting metallabenzenes form a fascinating new class of metallacyclic compounds.

The first metallabenzene was synthesised by W. R. Roper et al. in 1982 in a reaction that involved metal mediated cyclo-addition reactions of acetylene to the metalC bond of the CS ligand in $Os(CO)(CS)(PPh_3)_3$. Subsequently a small number of other stable metallabenzenes have been synthesised and studied by other researchers. Key steps in the synthetic routes to these metallabenzenes are ring closure of a pentadienyl ligand by CH bond activation, rearrangement of a 3-vinyl-1-cyclopropene ligand, oxidation of a bicyclic iridacyclohexadiene, and [2+2+1] cyclo-trimerization of alkynes (see Figure 1).

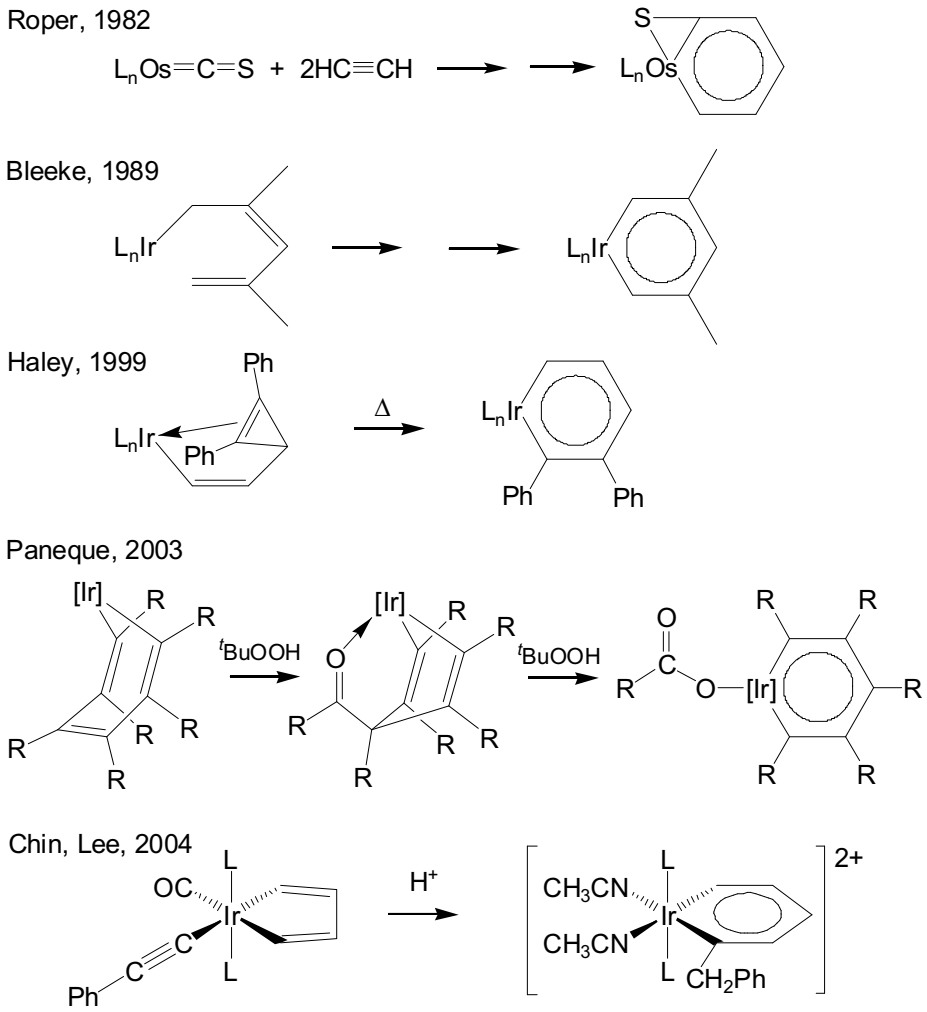

Fig. 1:

1 Synthesis and study of an osmabenzofuran

In the synthesis of the first osmabenzene described above, it is possible that the reaction proceeds via the formation of an osmacyclobutene complex through addition of the first acetylene to the OsC bond of the CS ligand in $Os(CO)(CS)(PPh_3)_3$. Indeed, some support for this possibility comes from the reaction of diphenyl acetylene with $Os(CO)(CS)(PPh_3)_3$. This reaction produces a mixture of two products in equal amounts, one containing an osmacyclobutene ring system that is formed through combination of acetylene with coordinated CS (complex 1), and the other containing a coordinated dipheny-

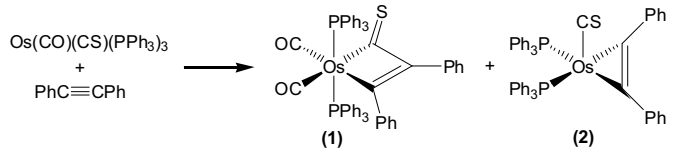

Fig. 2:

lacetylene and an unchanged CS ligand (complex 2, (see Figure 2). A redistribution of CO ligands occurs during this reaction and the coordinatively saturated osmacyclobutene-containing product contains two coordinated CO ligands whereas the other product contains none.

The diphenylacetylene-containing complex, Os(CPh=CPh)(CS)$(PPh_3)_2$ (2), which is potentially coordinatively unsaturated, appeared to be a good candidate for conversion to a new osmabenzene through addition of a suitable acetylene, since cyclo-addition/insertion reactions involving two coordinated acetylenes and CS could lead directly to the required six-membered, metallacyclic ring system.

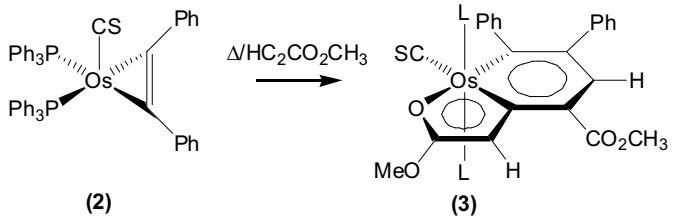

Fig. 3:

It was found that treatment of Os(CPh=CPh)(CS)$(PPh_3)_2$ with methyl propiolate (HC=CC(O)OCH_3) does indeed produce a new osmabenzene. Surprisingly, though, the CS ligand is not incorporated into the six-membered metallacyclic ring. Instead, two methyl popriolate molecules combine with the coordinated diphenyl acetylene in a [2+2+1] cyclo-trimerisation reaction to form the complex, Os[C_7H_2O(OMe-2)(CO_2Me-4)(Ph-6)(Ph-7)](CS)$(PPh_3)_2$ (3). The methyl propiolate molecule that contributes only one acetylenic carbon atom to the six-membered metallacyclic ring forms an additional bond to osmium through the carbonyl oxygen atom of the ester function. In this way a fused five- and six-membered metallacyclic ring system is formed (see Figure 3). The spectroscopic and structural data lend strong support to a metallabenzofuran formulation for this compound.

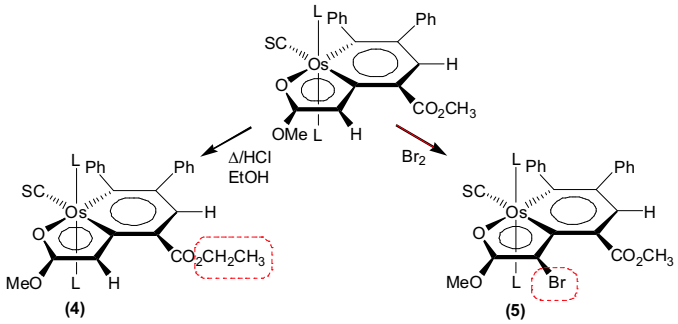

Fig. 4:

The osmabicyclic ring system in 3 is remarkably robust and heating this compound under reflux in ethanol with aqueous HCl effects only a transesterification of the ester function at the ring 4-position forming, $Os[C_7H_2O(OMe\text{-}2)(CO_2Et\text{-}4)(Ph\text{-}6)(Ph\text{-}7)](CS)(PPh_3)_2$ (4). Powerful electrophiles, however, attack the ring 3-position and treatment of 3 with pyridinium tribromide effects bromination at this position in an electrophilic substitution reaction to form $Os[C_7HO(OMe\text{-}2)(Br\text{-}3)(CO_2Me\text{-}4)(Ph\text{-}6)(Ph\text{-}7)](CS)(PPh_3)_2$ (5) (see Figure 4).

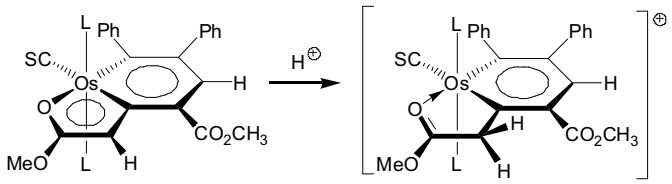

Fig. 5:

Treatment of 3 with nonaqueous trifluoroacetic acid results in protonation at carbon atom 3 and disruption of the delocalised bonding in the five-membered ring. The product formed is the cationic, tethered osmabenzene, $[OsC_5H(CH_2CO_2Me\text{-}1)(CO_2Me\text{-}2)(Ph\text{-}4)(Ph\text{-}5)(CS)(PPh_3)_2]CF_3CO_2$ (6) (see Figure 5). This osmabenzene cation has been isolated and fully characterised as the tri-iodide salt, $[Os[C_5H(CH_2CO_2Me\text{-}1)(CO_2Me\text{-}2)(Ph\text{-}4)(Ph\text{-}5)](CS)(PPh_3)_2]I_3$ (7). Spectroscopic parameters of 6 and 7 and structural studies of 7 are fully consistent with an osmabenzene formulation for this compound.

2 Acknowledgements

I thank my co-worker Professor W. R. Roper, my colleagues Professor G. R. Clark and Assoc. Prof. C. E. F. Rickard, FORST Postdoctoral Fellow Deborah Tonei, and PhD student Paul Johns. Financial support was provided by the Marsden Fund, FORST and the University of Auckland.

A case for linear agostic interaction in tantalum chemistry

*Adrian B. Chaplin, John A. Harrison, Alastair J. Nielson**

Chaohong Shen and Joyce M. Waters

Institute of Fundamental Sciences, Massey University (Albany Campus), Private Bag 102904, North Shore MSC, Auckland, New Zealand

1 Introduction

Agostic interactions play an important part in C-H bond organometallic chemistry and catalysis.[1, 2, 3] Such interactions are usually found to consist of side-donation of C-H bonding electron density to an electron deficient metal and are generally described as a three-centre-two electron bonding system.[1, 2] However agostic bonding is defined as "the interaction of C-H electron density with an electron-deficient metal"[1] which does not limit the interaction to the usual side-on mode. Tris(2-hydroxybenzyl)amine ligands[4] **I** on protonation at nitrogen and tris(2-hydroxyphenyl)methane ligands[5] **II** have the potential to place a hydrogen atom in close proximity to a metal with the N-H or C-H bond orientated in an "end-on" or "linear" fashion if the tripod coordinates with the particular hydrogen facing inwards. Where an electron deficient metal is present such as in a high-valent early transition metal, the hydrogen atom may interact significantly with an appropriate unfilled metal d orbital.

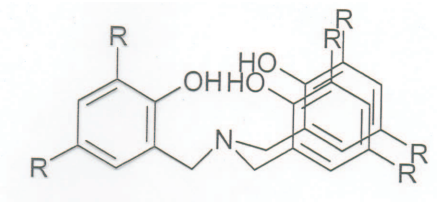

I

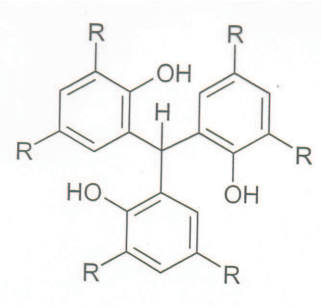

II

Fig. 1:

2 Results and Discussion

When two equivalents of tris(2-hydroxy-3,5-dimethylbenzyl)amine (ligand type I, R=Me) were added to $[Zr(OnBu)_4]$ in CH_2Cl_2 a colourless air-stable precipitate was formed. An X-ray crystal structure of the recrystallised product showed that the Zr atom lies on a centre of symmetry surrounded by a distorted octahedral arrangement of six similar phenoxy O atoms (Fig 2). The Zr-O bond lengths [2.066(2), 2.064(2) and 2.049(2) Å] are similar to those found in phenoxide complexes where the O-to-Zr p-donation is spread over several O-atom donors[6] and the Zr-O-C bond angles [158.0(2), 162.6(2) and 160.3(2)o] are similar to other complexes of this ligand.[7] The ^{1}H NMR spectrum indicates the nitrogen atoms in the complex are protonated and the crystal structure shows these on the inside with the N-bound H atom trapped in a cage-like arrangement at distances of 2.27, 2.12 and 2.29 Å from atoms O(1), O(2) and O(3) respectively. Such approaches are indicative of weak H...O hydrogen bonding.[8] The H atom points directly at the Zr atom [Zr...H-N, 174(2)o] at a distance of 2.76(3) Å which is not expected to involve significant interaction of the hydrogen with the metal centre. The Zr...N separation is 3.603(2) Å. The six oxygen atoms carry an overall formal charge of 2 for this part of the molecule and the nitrogen atoms each contain a charge of +1 so that the complex is di-zwitterionic.

One equivalent of tris(3,5-di-tert-butyl-2-hydroxy)methane (ligand type II, R = CMe_3) added to $TaCl_5$ suspended in CH_2Cl_2, followed by triethylamine, gave a mixture of products. Recrystallisation of the solid over an extended period of time (ca. several weeks) gave a small quantity of crystals. A single crystal X-ray analysis of one of these showed an anion (Fig. 3) consisting of a distorted octahedral coordination geometry, with the metal

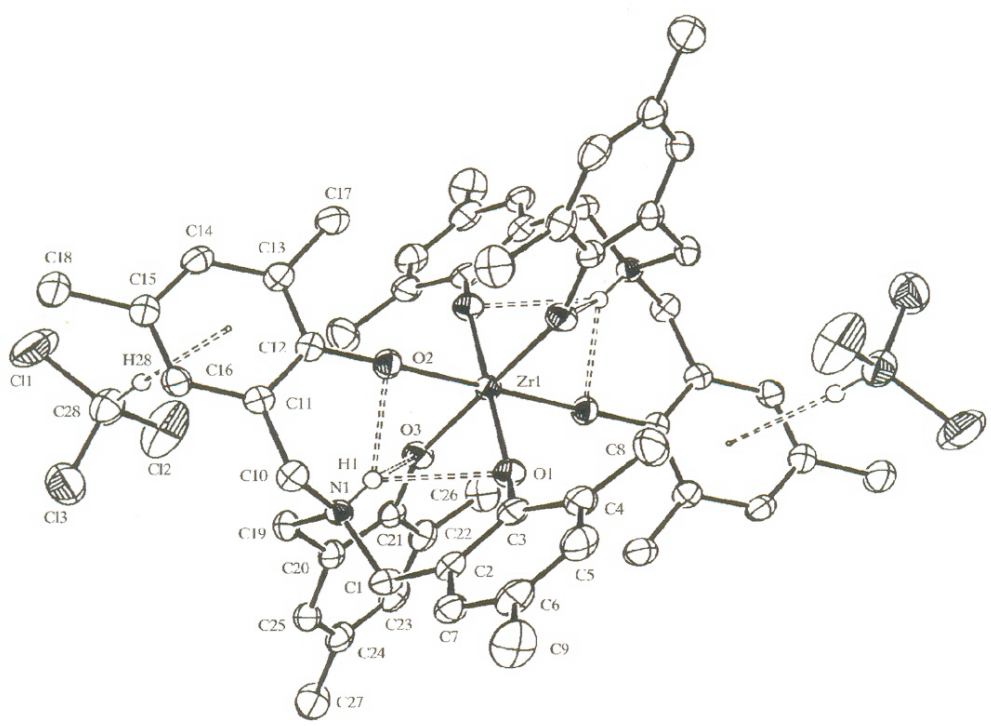

Fig. 2:

surrounded by three chloro ligands and three oxygen atoms of the tripodal ligand.

The Ta and one phenoxy ring of the ligand lie in a mirror plane with the other two "arms" forming a mirrored pair. The three Ta-Cl bond lengths [Ta1-Cl(1), Ta1-Cl(1) 2.415(1), Ta1-Cl(2) 2.431(2) Å] are all similar as are the Ta-O bond lengths [Ta1-O(1) , Ta1-O(1) 1.949(2), Ta1-O(2) 1.923(4)]. These are consistent with six anionic ligands around the tantalum centre resulting in a formal negative charge for the coordination sphere in a similar manner to a $[TaCl_3(OAr)_3]$ anion. An amine cation was located as the counter ion and this lies between the two mirror-related phenoxy rings. Two of the solvent benzene molecules also lie in the space between the other phenoxy rings.

The bond angles about the linking carbon atom [C(20)] are very distorted [C(2)-C(20)-C(22) and C(2)-C(20)-C(22) 116.2(3)o, C(2)-C(20)-C(2) 121.0(5)o] and C(20) lies 0.23 Å above the plane defined by C(2), C(2) and C(22). In the free ligand the respective angles about the central sp^3 carbon are 114.1, 114.0 and 114.0° with the carbon atom lying 0.40(2) Å above the plane[5]. In the more constrained alkali metal salts of the

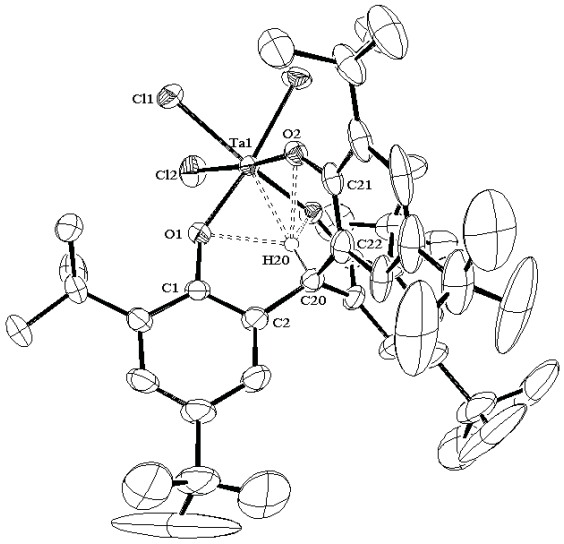

Fig. 3:

ligand these angles range from 111.6 to 114.0°.[5] The phenyl rings in the anion are twisted approximately 66° with respect to one another. On the difference map there was evidence for an H atom attached to C(20) in a position close to its calculated site. It was included in the refinement at this calculated position [C(20)-H(20) 1.0 Å] riding on C(20) and at a distance of 1.0 Å from it. In this position the hydrogen atom is enclosed in a cage and makes contacts of 2.02, 2.02 and 2.05 Å with O(1), O(1) and O(2) distances which are consistent with weak C-H bond hydrogen bonding[8]. As well, the hydrogen atom points directly at the tantalum atom [Ta1...H(20)-C(20) angle 178.2o] at a distance of 2.16 Å from it.

Density functional (DFT) calculations were carried out on models of the anion to examine the electronic features of the uniquely caged C-H hydrogen which is held in a position where there can be no side-on interaction of the C-H bonding electron density with the metal, which is typical of an agostic interaction.1 Models of the anion either without phenyl group substituents (model 1) or with ortho-t-butyl substituents (model 2) resulted in structures that were in good agreement with the crystal structure. The counter ion, which is located between two of the ligand phenyl rings in the X-ray structure, has a particular influence on the distortion away from a symmetric structure. In the models the

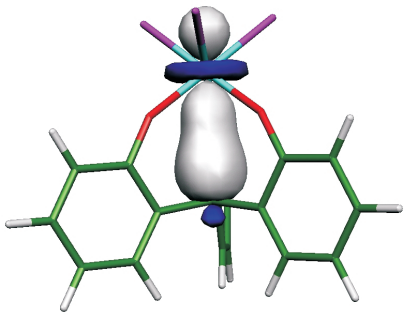

Fig. 4:

deviation is slight, for example in 2 the three O-Ta-O angles are 93.1, 93.7, 93.7 degrees, whereas the comparable angles in the crystal structure are 98.1, 95.0, and 95.0 illustrating that one of the O-Ta-O angles opens up as a result of accommodating the counter-ion. Other models at the same level of theory involving either a de-protonated [C(20)] neutral singlet state, neutral triplet state, protonated neutral radical, or analogues of 1 containing the proton on the outer side of C(20) gave poor agreement, with the phenyl rings twisted significantly to allow p-delocalisation to occur.

An NBO analysis[9] showed that the C-H bonding orbital for 1 is comprised of 12.1% C 2s, 50.6% C 2p and 37.3% H 1s (complex 2: 12.3% C 2s, 51.4% C 2p, 0.1% C 3d, 36.2% H 1s) character, whereas the C-H antibonding orbital is 7.2% C 2s, 30.0% C 2p and 62.8% H 1s (7.0% C 2s, 29.2% C 2p, 63.8% H 1s).The NBO analysis gave the stabilisation energy, E_2, for the interaction between the C-H bonding orbital and the Ta 5dz2 orbital of 10.95 and 15.2 kcal/mol respectively for 1 and 2. An average E_2 of 6.16 and 5.52 kcal/mol

respectively was found for the interaction involving the C-H bonding orbital and one of the antibonding C-C orbitals from each of the benzene rings.

The spatial overlap (43%) between the C-H bonding orbital and the Ta $5dz^2$ orbital for model 1 is depicted in fig. 4. There is a relatively slight (1.99 and 2.20 kcal/mol for 1 and 2 respectively) interaction between the C-H bonding orbital and the partially filled Ta 6s valence orbital and no other significant (i.e. >2.0 kcal/mol) donor interactions from this orbital. In comparison the average stabilization energy for each chlorine lone pair donor orbital summed over all of the acceptor Ta valence orbitals is 33.5 and 31.9 kcal/mol for 1 and 2 respectively. The corresponding interaction with the oxygen lone pairs is 57.7 and 56.3 kcal/mol per lone pair. Donation from one lone pair on each oxygen atom to the C-H s* orbital gives an E_2 of 4.21 kcal/mol for model 1 and 4.45 kcal/mol for model 2.

3 Conclusion

Tris(2-hydroxybenzyl)amine ligands I and tris(2-hydroxyphenyl)methane ligands II are able to form unique cages about N-H or C-H hydrogen atoms which involve weak hydrogen bonding to three oxygen atoms and a close approach to a high-valent early transition metal.[10, 11] The close approach is forced on the hydrogen as coordination of the three phenoxide oxygen atoms to the metal allows it nowhere to go but into the metal orbital system. For the Ta complex, theoretical calculations indicate that there is significant overlap of the C-H bond electron density in a linear sense with an unfilled metal d orbital. A stabilisation energy of 15.2 kcal/mol is found where the phenoxide ligands contain ortho-tert-butyl substituents. The present interaction has the characteristics of an agostic interaction[1] except that it does not involve a bent agostic bond and thus appears to be an example of a previously unidentified linear agostic interaction involving a three-centre-two-electron bonding system.

References

[1] M. Brookhart, M. L. H. Green, L.-L Wong, Prog. Inorg. Chem., 1988, 36, 1.

[2] W. Baratta, C.Mealli, E. Herdtweck, A.Ienco, S. A. Mason and P. Rigo, J. Am. Chem. Soc.,2004, 126, 5549; L. Brammer, Dalton Trans., 2003, 3145; R. H. Grubbs, G. W. Coates, Acc.Chem. Res., 1996, 29, 85.

[3] W. Scherer and G. S. McGrady, Angew. Chem. In. Ed., 2004, 43, 1782.

[4] a) K. Hultzsch, Chem. Ber.,1949, 82, 16 b) T. R. Dargaville, P. J. De Bruyn, A.S. C. Lim, M. G. Looney, A. C. Potter, D. H. Solomon and X. Zhang, J. Polymer Sci., Part A, 1997, 35, 1389.

[5] M. B. Dinger, M. J. Scott, Eur. J. Org. Chem., 2000, 2467

[6] M. B. Dinger and M. J. Scott, Inor. Chem., 2001, 40, 856.

[7] M. Kol, M. Shamis, I. Goldberg, Z. Goldschmidt, S. Alfi and E. Guizado- Rodriguez, Inorg. Che. Commun., 2001, 4, 177.

[8] a) M. J. Calhorda, J. Chem. Soc. Chem. Commun. 2000, 801 b) G. R. Desiraju, Acc. Chem. Res. 1996, 29, 441.

[9] NBO version 3.1, E. D. Glendening, A. E. Reed, J. E. Carpenter, F. Weinhold.

[10] A. J. Nielson, C. Shen and J. M. Waters, Acta Cryst., 2003, C59, m494.

[11] A. B. Chaplin, J. A. Harrison, A. J. Nielson, C. Shen and J. M. Waters, Dalton Trans., 2004, 2643.

The performance of density functional theory for field gradients

Peter Schwerdtfeger

Institute of Fundamental Sciences, Massey University (Albany Campus), Private Bag 102904, North Shore MSC, Auckland, New Zealand

For the accurate determination of nuclear quadrupole coupling constants, e2qQ , both the nuclear quadrupole moment Q and the electric field gradient q at a specific atomic center in the molecule or the solid have to be known. Nuclear quadrupole moments for the most important isotopes are available to certain accuracy and discussed in a recent paper by Pyykkö [1]. The most accurate way to determine the nuclear quadrupole moment Q for a specific isotope is indirectly by high-resolution spectroscopy, i.e. by the measurement of the nuclear quadrupole coupling constant and precise determination of the electric field gradient tensor q?? from theory. Accurate nuclear quadrupole coupling constants are obtained from atomic experiments (electronic or muonic transitions in atoms); from rotational spectroscopy of small linear molecules or from magnetic resonance or Mössbauer spectroscopy. Nuclear quadrupole moments can be obtained experimentally by electron scattering, inelastic hadron scattering, Coulomb excitation, hyperfine effects in muonic atoms, hyperfine techniques or from nuclear structure calculations [2], but usually they are less accurate. Accurate electric field gradients are obtained from relativistic quantum chemical calculations including electron correlation effects from coupled-cluster or multi-reference configuration interaction methods. For a recent review see [3].

The most rigorous way of including relativity from the beginning is by use of the many-electron Dirac-Coulomb-Breit-Hartree-Fock (DCB-HF) approximation. However, such calculations require rather large computational resources when electron correlation has to be considered and basis sets are needed describing accurately the wavefunction close

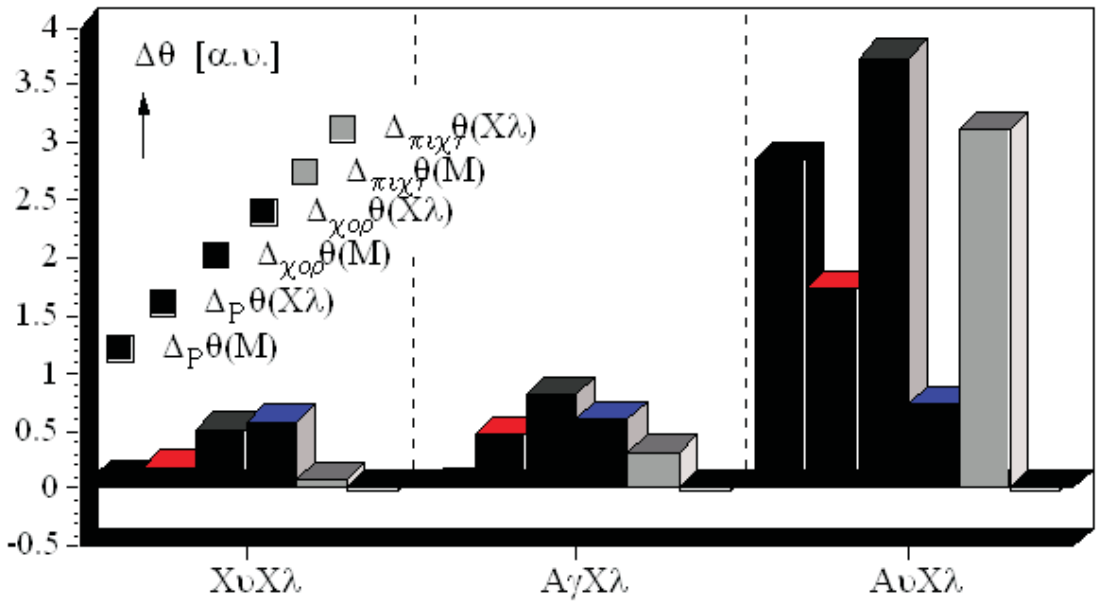

Fig. 1: Relativistic (Δ_R), correlation (Δ_{cor}), and picture change (Δ_{pict}) contributions to the electric field gradient of CuCl, AgCl, and AuCl.

to the nucleus. Scalar relativistic schemes, on the other hand, suffer from the well-known picture-change error [4, 5]. Such picture change errors can be very large for the heavier elements as figure 1 shows [5, 6]. An alternative model which avoids this error is by simulating the nuclear quadrupole moment perturbation via point charges (the PCNQM model) [7, 8]. This model is quite successful for the precise determination of electric field gradients in diatomic systems, however, it is too cumbersome to be used routinely for larger molecules including heavy elements. Here, ideally, four-component relativistic density functional calculations DFT are specially suited for larger molecules because of the low computational cost involved compared to the more expensive wave-function based procedures.

Density functional theory (DFT) is routinely used for nonrelativistic field gradient calculations in molecules or the solid state. Since the electric field gradient is a typical core property, it is widely assumed that density functionals perform well. For example, a comparison between B3LYP and fourth-order Møller-Plesset perturbation theory for the 2H NQCC of a number of molecules shows only minor differences between both methods [9]. In general DFT performs extremely well [10, 11] for main group elements. However,

the situation completely changes for transition-element containing compounds. Commonly used density functionals are not able to correctly describe the electron density distribution in CuCl [12]. Here the polarization of the Cu(3d) core by the chlorine atom has to be described correctly to obtain accurate electric properties such as the dipole moment or the electric field gradient at copper. For example, the CuCl dipole moment varies considerably between the different DFT approximations: 4.14 D for HFS, 4.38 D for LDA, 4.30 D for BLYP, and 4.87 D for B3LYP. For comparison, the Douglas-Kroll (DK) CCSD(T) value is 5.32 D. Slight variations in the molecular charge distribution obviously effect the electric field gradient at the copper atom, i.e. q(Cu) is +0.67 a.u. for HFS, +0.50 a.u for LDA, +0.54 a.u. for BLYP, and +0.15 a.u. for B3LYP [12]. The DK-CCSD(T) value is 0.34 a.u. and the experimental value is 0.31(2) a.u. [13]. There is a clear correlation between the error in the electric field gradient and the dipole moment as figure 2 shows. These results have been confirmed by Baerends and co-workers, who also obtained large errors in DFT electric field gradient calculations for copper and silver halides using the zeroth-order regular approximation (ZORA) to the Dirac equation [14].

Similar results are obtained for a number of other transition element compounds. For example, for q(Fe) in ferrocene, DFT calculations give 1.36 a.u. for both HFS and LDA, 1.43 a.u. for BLYP, and 1.85 a.u. for B3LYP (1.50 a.u. at the CCSD(T) level) [16]. Problems therefore arise for the accurate determination of the 57Fe NQM [17]. We therefore investigated in more detail the density functional approximation for representative molecules starting from a series of early transition metal compounds, ScX, to late transition metal compounds, CuX, and finally to main group compounds, GaX, where X= F, Cl, Br, I, H and Li. We find that common density functionals work well for main group compounds (GaX), but contain large systematic errors for transition metal compounds [18]. This leads to unreasonable copper nuclear quadrupole moments obtained from the complete CuX set, see figure 3. For copper compounds this can be remedied in an ad-hoc way by adjusting the Hartree-Fock exchange contribution in the exchange part of the hybrid functional (modified B3LYP). Using this modified B3LYP functional we obtain reasonable results for the copper electric field gradient in CuF3, a case where the Cu(3d) core is strongly polarized by the fluorine ligands. Similar problems have recently been reported for gold compounds [19] and for the uranium electric field gradient in UO22+ compounds by Baerends and co-workers [20].

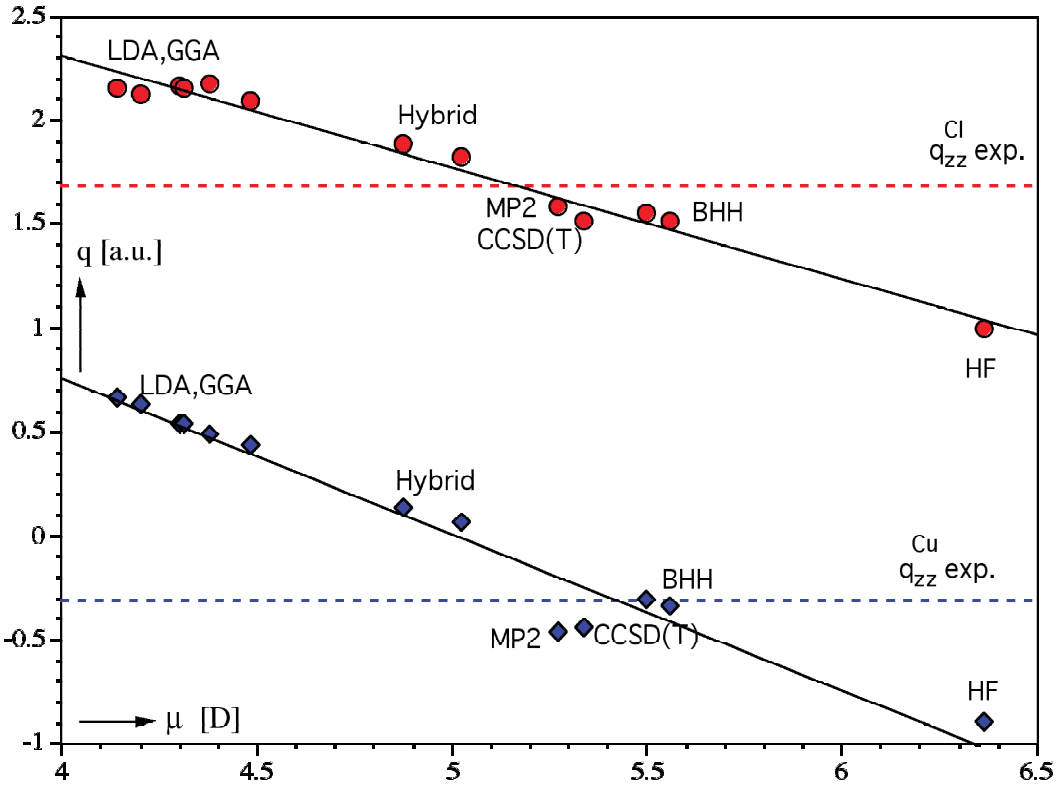

Fig. 2: The copper and chlorine electric field gradient plotted against the CuCl dipole moment at various levels of theory. The horizontal line shows the expected experimental field gradients calculated from the nuclear quadrupole coupling constants by Hoeft et al. [15].

Density functional theory has been widely used for electric field gradient calculations in solid-state transition element compounds using the Vienna code [21, 22], but the results are questionable. An interim solution is to change the parameter of the Hartree-Fock admixture in hybrid functionals such as B3LYP, but this has to be done for each individual transition element and it is not clear that this scheme works for different compounds of the same transition metal. A better solution is to introduce long-range corrections as recently done in Hiraos group [23], but this has to be tested. To conclude, the accurate determination of electric field gradients from DFT for the d- and f-element containing compounds remains an open question, which has to be addressed in the near future.

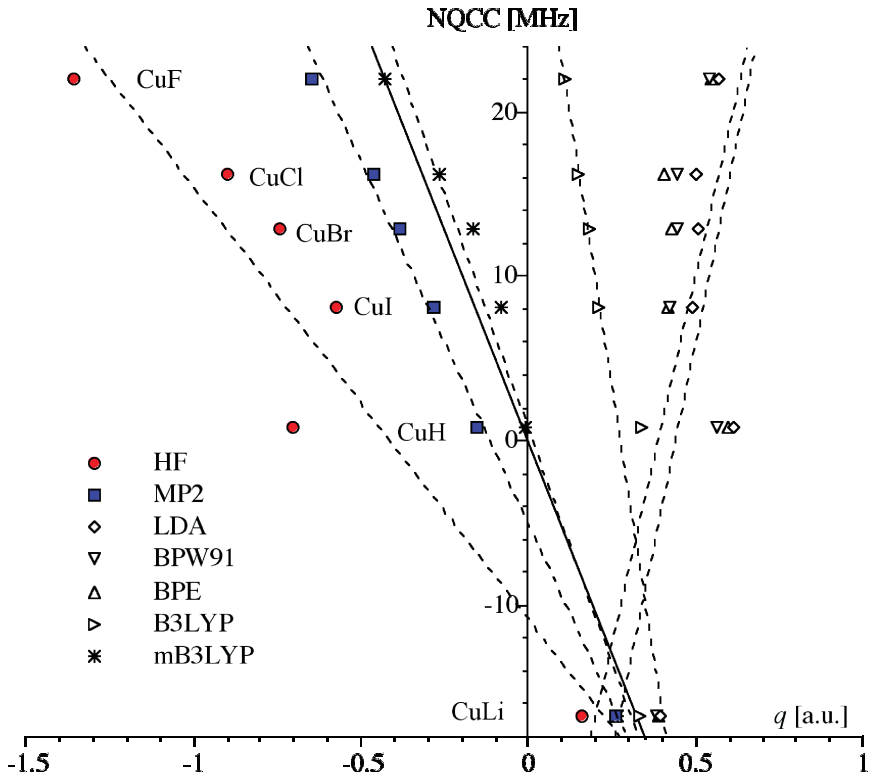

Fig. 3: Electric field gradient vs. the nuclear quadrupole coupling constant for diatomic copper compounds.

Acknowledgment

This work was supported by the Marsden Fund administered by the Royal Society of New Zealand. We are grateful to the Allan Wilson Centre for large amounts of computer time on their high-performance parallel computer HELIX

References

[1] P. Pyykkö, Mol. Phys. 2001, 99, 1617.

[2] W. Nazarewicz and I. Ragnarsson, in Handbook of Nuclear Properties, ed. by D. N. Poenaru and W. Greiner, (Clarendon Press, Oxford), 1996; p. 80.

[3] P. Schwerdtfeger, M. Pernpointner, W. Nazarewicz, Calculation of Nuclear Quadrupole Coupling Constants, In "Calculation of NMR and EPR Parameters: The-

ory and Applications" (Editors: M. Kaupp, M. Bühl, V. G. Malkin), Wiley-VCH, Weinheim, 2004; pgs. 279-291.

[4] E. J. Baerends, W. H. E. Schwarz, P. Schwerdtfeger, J. G. Snijders, J. Phys. B: At. Mol. Phys. 1990, 23, 3225.

[5] M. Barysz, A. J. Sadlej, Theor. Chim. Acta 1997, 97, 260.

[6] M. Pernpointner and P. Schwerdtfeger, B. A. Hess, Int. J. Quant. Chem. 2000, 76, 371.

[7] M. Pernpointner, M. Seth, P. Schwerdtfeger, J. Chem. Phys. 1998, 108, 6722.

[8] V. Kellö, A. J. Sadlej, J. Chem. Phys. 2000, 112, 522.

[9] W. C. Bailey, J. Mol. Spectrosc. 1998, 190, 318.

[10] W. C. Bailey, F. M. Gonzalez, J. Castiglione, Chem. Phys. 2000, 260, 327.

[11] J. N. Latosinska, Int. J. Quantum Chem. 2003, 91, 284.

[12] P. Schwerdtfeger, M. Pernpointner, J. K. Laerdahl, J. Chem. Phys. 1999, 111, 3357.

[13] J. Hoeft, J. J. Lovas, E. Tiemann, T. Törring, Z. Naturforsch. 1970, 25a, 34.

[14] E. van Lenthe, E. J. Baerends, J. Chem. Phys. 2000, 112, 8279.

[15] J. Hoeft, F. J. Lovas, E. Tiemann and T. Törring, Z. Naturforsch. 1970, 26a, 240.

[16] P. Schwerdtfeger, T. Söhnel, M. Pernpointner, J. K. Laerdahl, F. E. Wagner, J. Chem. Phys. 2001, 115, 5913.

[17] F. Hagelberg, T. P. Das, K. C. Mishra, Phys. Rev. B 2002, 65, 014425.

[18] R. Bast, P. Schwerdtfeger, J. Chem. Phys. 2003, 119, 5988.

[19] P. Schwerdtfeger, R. Bast, M. C. L. Gerry, C. R. Jacob, M. Jansen, V. Kellö, A. V. Mudring, A. J. Sadlej, T. Saue, T. Söhnel, F. E. Wagner, J. Chem. Phys. 2005, 122, 124317.

[20] P. Belanzoni, E. J. Baerends and E. van Lenthe, Mol. Phys. 2005, 103, 775.

[21] P. Blaha, K. Schwarz, P. H. Dederichs, Phys. Rev. B 1988, 37, 2792.

[22] T. J. Bastow, M. I. Burgar, C. Maunders, Solid State Commun. 2002, 122, 629

[23] T. Sato, T. Tsuneda, and K. Hirao, Mol. Phys. 2005, 103, 1151.